

**Quantum Effects from Classical Trajectories: New Methodologies and  
Applications for Semiclassical Dynamics**

by

David William Howey Swenson

A dissertation submitted in partial satisfaction of the  
requirements for the degree of  
Doctor of Philosophy

in

Chemistry

in the

GRADUATE DIVISION  
of the  
UNIVERSITY OF CALIFORNIA, BERKELEY

Committee in charge:  
Professor William H. Miller, Chair  
Professor Martin Head-Gordon  
Professor Maciej Zworski

Fall 2011

The dissertation of David William Howey Swenson is approved:

---

Chair

Date

---

Date

---

Date

University of California, Berkeley

Fall 2011

**Quantum Effects from Classical Trajectories: New Methodologies and  
Applications for Semiclassical Dynamics**

Copyright 2011  
by  
David William Howey Swenson

## Abstract

### Quantum Effects from Classical Trajectories: New Methodologies and Applications for Semiclassical Dynamics

by

David William Howey Swenson  
Doctor of Philosophy in Chemistry  
University of California, Berkeley  
Professor William H. Miller, Chair

Semiclassical approaches to chemical dynamics show great promise as methods to obtain practical results for a wide range of problems. In this dissertation we make these approaches more practical, by improving the efficiency of the calculations, and apply them to a wider range of problems, by developing techniques to explore new kinds of problems.

The approaches to improve the efficiency of semiclassical calculations essentially fall into two categories: we can reduce the number of trajectories we need in order to converge the calculation, or we can make each trajectory easier to calculate. (Of course, these two are not mutually exclusive.)

In this work, we have made attempts on both sides. Our efforts to reduce the number of trajectories required have been focused on finding ways to make the Monte Carlo sampling more efficient. The first method uses time-dependent information in order to reduce the sampling space. The second explores the idea of histogramming the phase of the contribution to the integrand. Although only the first of these shows real promise as a way to speed up semiclassical calculations, both methods can provide insights on the nature of the quantum effects we observe.

In an effort to make each trajectory easier to calculate, we developed a new method for calculating the monodromy matrix, which serves as the input to calculating the semiclassical prefactor. Calculating the semiclassical prefactor is the most computationally expensive part of generating a trajectory for a semiclassical calculation. Our new method doesn't break open the bottleneck, but it does make a meaningful improvement.

Finally, we step beyond simple improvements in efficiency. The dynamics of fermions provide a challenge for semiclassical methods. We present a method for generating a semiclassical Hamiltonian from a second-quantized fermionic Hamiltonian. This technique is applied to a simple model of a molecular transistor, and the results are in excellent agreement with the exact quantum calculations.

---

Professor William H. Miller  
Dissertation Committee Chair

To my four grandparents —

who taught me to love the future embodied by science, to love the past embodied by tradition, to be reverent in my faith, and to be irreverent in my humor

# Contents

<b>List of Figures</b>	<b>v</b>
<b>List of Tables</b>	<b>ix</b>
<b>Preface</b>	<b>1</b>
The Semiclassical Approach . . . . .	1
Thesis Outline . . . . .	2
<b>1 Introduction to Semiclassical Methods</b>	<b>3</b>
1.1 Semiclassical Propagators . . . . .	3
1.1.1 The Van Vleck IVR . . . . .	4
1.1.2 The Herman-Kluk IVR . . . . .	9
1.1.3 Implementation of a Semiclassical Propagator . . . . .	15
1.2 Semiclassical Correlation Functions . . . . .	18
1.2.1 Double Herman-Kluk . . . . .	18
1.2.2 Linearized SC-IVR . . . . .	19
1.2.3 Forward-Backward IVR . . . . .	23
1.2.4 Other SC-IVR Methods for Correlation Functions . . . . .	26
1.3 The Meyer-Miller-Stock-Thoss Hamiltonian . . . . .	26
1.3.1 Derivation . . . . .	26
1.3.2 Using the MMST in the SC-IVR . . . . .	28
1.3.3 Numerical Challenges in MMST Dynamics . . . . .	29
<b>2 Time-Dependent Monte Carlo</b>	<b>32</b>
2.1 Time-Dependent Monte Carlo . . . . .	32
2.1.1 Initial Value Monte Carlo . . . . .	33
2.1.2 Endpoint Time-Dependent Monte Carlo . . . . .	34
2.1.3 Path Sampling Time-Dependent Monte Carlo . . . . .	35
2.1.4 Sampling Multiple Domains: The Dual-Delta Method . . . . .	35
2.1.5 Specializing to the DHK-IVR . . . . .	37
2.2 Results . . . . .	38
2.2.1 Position Probability Distribution for $I_2$ . . . . .	38
2.2.2 Survival Amplitude of an Anharmonic Morse Oscillator . . . . .	41

2.3	Discussion . . . . .	45
2.4	Future Directions . . . . .	47
2.4.1	Another System: Tully Model 1 . . . . .	47
2.4.2	Proposed Method to Approximate IVR Results . . . . .	47
<b>3</b>	<b>Phase Histogram IVR</b>	<b>49</b>
3.1	HK-IVR as a Phase Histogram Problem . . . . .	49
3.2	Gaussian Fitting of the Phase Histogram . . . . .	50
3.3	Test System: The Quartic Oscillator . . . . .	51
3.4	Test System: The Anharmonic Morse Oscillator . . . . .	57
3.5	Discussion and Future Directions . . . . .	61
<b>4</b>	<b>The Precision Finite Difference Monodromy Matrix</b>	<b>62</b>
4.1	Older Methods . . . . .	62
4.1.1	Naïve Finite Difference . . . . .	63
4.1.2	Garashchuk and Light's Finite Difference Method . . . . .	64
4.2	The Precision Finite Difference Method . . . . .	65
4.3	Comparison of Methods for Simple Potentials . . . . .	66
4.3.1	One-Dimensional Potentials . . . . .	68
4.3.2	A Chaotic Two-Dimensional Test: The Hénon-Heiles Potential . . . . .	70
4.4	Discussion and Future Directions . . . . .	74
<b>5</b>	<b>Semiclassical Treatment of Fermionic Systems</b>	<b>76</b>
5.1	Classical Mapping of the Quantum Hamiltonian . . . . .	76
5.1.1	Mapping Matrix Elements to Classical Expressions . . . . .	77
5.1.2	Book-Keeping Functions . . . . .	79
5.1.3	Choosing the Length $\sigma$ . . . . .	82
5.1.4	Aside: Cartesian Expressions for this Mapping . . . . .	85
5.2	Measuring the Time-Dependent Current: Treatment of Operators . . . . .	87
5.2.1	Discretization of the Spectral Density . . . . .	87
5.2.2	Describing the Initial Conditions . . . . .	88
5.2.3	The Current Operator . . . . .	90
5.2.4	Aside: Time Derivative of the Current Operator at $t = 0$ . . . . .	91
5.3	The Landauer Problem: A Test System . . . . .	98
5.4	Future Directions . . . . .	104
<b>Concluding Thoughts</b>		<b>106</b>
<b>A</b>	<b>Model Systems</b>	<b>108</b>
A.1	Harmonic Oscillator . . . . .	108
A.2	Anharmonic Morse Oscillator . . . . .	109

<b>B Adaptive Gear 6th-Order Predictor-Corrector</b>	<b>115</b>
B.1 The 6th-Order Gear Predictor-Corrector . . . . .	116
B.2 The Adaptive Timestep Algorithm . . . . .	116
B.3 Fixing the Time Discretization . . . . .	117
<b>Bibliography</b>	<b>118</b>

# List of Figures

1.1	The IVR “Trick”: The black curve takes a given initial position $q_0$ for some hypothetical system and shows possible final positions $q_t$ reached from different initial momenta. The red line highlights the fact that a given $q_t$ can be reached from more than one $p_0$ . The initial value representation switches the axis of integration from $q_t$ to $p_0$ .	9
1.2	Cartoon of the linearized semiclassical initial value representation (LSC-IVR) method for calculating correlation functions. The original forward and backward trajectories (black) are written in sum (average, $(\bar{q}, \bar{p})$ ) and difference ( $\Delta q, \Delta p$ ) variables (red). The linearization approximation is that the difference variables $\Delta q$ and $\Delta p$ remain very small.	21
1.3	Cartoon of the forward-backward IVR (FB-IVR) method for calculating correlation functions. For each forward trajectory $(q_0, p_0) \rightarrow (q_t, p_t)$ , a number of jumps $\Delta$ are made, and a backward trajectory is run from for each jump from $(q_{t'}, p_{t'})$ to $(q_{0'}, p_{0'})$ . One such backward trajectory is shown in full; the starts of others are shown as the green arrows.	24
2.1	Comparison of two ways of sampling a positive definite $A(x_0)B(x_t)$ . (a) Using $A(x_0)$ as the sampling function, we see that we sample many regions where the total integrand is nearly zero. (b) Using the whole function for sampling, we have several distinct regions of sampling, but we don’t sample where the integrand is nearly zero.	33
2.2	Cartoon illustrating (a) Initial Value Monte Carlo, (b) Endpoint Time-Dependent Monte Carlo, and (c) Path Sampling Time-Dependent Monte Carlo.	34
2.3	Cartoon illustrating two methods for sampling distributions with multiple domains within an envelope: (a) represents the “big-delta” method, which only uses the Monte Carlo step appropriate to the envelope function; (b) represents the “dual-delta” function, where two step sizes are possible; one from the envelope function and one from the smaller domain.	36
2.4	Radial probability distribution for $I_2$ , calculated by FB-IVR (black line), and DHK-IVR with IVMC (red), EP-TDMC (green), and PS-TDMC (blue) sampling.	39
2.5	Convergence of various methods for the radial probability distribution of $I_2$ (as a root-mean-square deviation over several initial random seeds).	40

2.6	Phase space plots (in atomic units) of the distribution sampled by the TDMC methods for calculating the radial distribution of I <sub>2</sub> nuclei at $t = 192$ fs for (a) 2.43 Å and (b) 2.49 Å. . . . .	41
2.7	Survival amplitude for the anharmonic Morse oscillator calculated with optimized delta. Note the failure to reproduce the correct result from around times 7-9 and times 12-14. . . . .	42
2.8	Survival amplitude for the anharmonic Morse oscillator calculated by the DHK-IVR, with EP-TDMC sampling. Sampling trials for the pink points were selected by the big-delta method; trials for the light blue points were selected by the dual-delta method. . . . .	43
2.9	Phase space for calculating the anharmonic Morse oscillator survival amplitude at $t = 12.3$ for various sampling methods: (a) IVMC, (b) EP-TDMC with big-delta trial selection, (c) EP-TDMC with optimized delta ( $\sim 50\%$ acceptance ratio) trial selection, and (d) EP-TDMC with dual-delta ( $p_{\text{big}} = 0.1$ ) trial selection. . . . .	44
2.10	Convergence of the survival amplitude for the anharmonic Morse oscillator at $t = 12.3$ for EP-TDMC with the dual-delta trial selection (with several values of $p_{\text{big}}$ ) compared to big-delta trial selection. . . . .	45
3.1	Survival amplitude of the quartic oscillator system. (a) Phase histogram of the survival amplitude as a function of time. (b) Modulus of the survival amplitude as calculated by the HK-IVR and LSC-IVR. . . . .	52
3.2	Convergence of the Gaussian fit for the quartic oscillator at $t = 55.0$ as a function of the number of rehistogrammed bins, for different numbers of Gaussians. The exact HK-IVR result is shown, as is the rehistogrammed result for each number of bins. . . . .	53
3.3	Phase histogram and sum-of-Gaussians fit for the quartic oscillator at $t = 55.0$ , with 100 bins and 10 Gaussians. . . . .	54
3.4	Convergence of the phase histogram for the quartic oscillator at $t = 55.0$ as a function of trajectories for various methods of choosing the “best” number of bins and number of Gaussians for the Gaussian fitting method. . . . .	55
3.5	Survival amplitude of the anharmonic Morse oscillator system. (a) Phase histogram of the survival amplitude as a function of time. (b) Modulus of the survival amplitude as calculated by the HK-IVR, by the LSC-IVR, and by rebuilding the phase histogram with cutoff 0.005 (normalized to 250 bins). . . . .	56
3.6	Convergence of the Gaussian fit for the anharmonic Morse oscillator at $t = 5.0$ as a function of the number of rehistogrammed bins, for different numbers of Gaussians. The exact HK-IVR result is shown, as is the rehistogrammed result for each number of bins. . . . .	57
3.7	Phase histogram and sum-of-Gaussians fit for the anharmonic Morse oscillator at $t = 5.0$ , with 70 bins and 6 Gaussians. . . . .	58
3.8	Convergence of the Gaussian fit for the anharmonic Morse oscillator at $t = 12.3$ as a function of the number of rehistogrammed bins, for different numbers of Gaussians. The exact HK-IVR result is shown, as is the rehistogrammed result for each number of bins. . . . .	59

3.9	Phase histogram and sum-of-Gaussians fit for the anharmonic Morse oscillator at $t = 12.3$ , with 80 bins and 10 Gaussians.	60
4.1	Cartoon of the naïve finite difference method for calculating the monodromy matrix.	63
4.2	Cartoon of Garashchuk and Light's method for calculating the monodromy matrix.	64
4.3	Cartoon of the precision finite difference method for calculating the monodromy matrix.	65
4.4	Flowchart for the precision finite difference algorithm.	67
4.5	Tests for the one-dimensional anharmonic Morse oscillator.	69
4.6	The Hénon-Heiles Potential. The arrows show the initial directions of the A-type and NP-type trajectories.	70
4.7	Percent error in the magnitude of the Herman-Kluk prefactor for the NP-type trajectories from the Hénon-Heiles potential, comparing the precision finite difference method to the naïve method.	71
4.8	Percent error in the magnitude of the Herman-Kluk prefactor for the A-type trajectories from the Hénon-Heiles potential, comparing the precision finite difference method to the naïve method.	72
4.9	The Quadric (or $x^2y^2$ ) Potential.	75
5.1	Discretization of the spectral density into 50 discrete modes with $A = 5$ and $B = 20$ .	88
5.2	Illustration of the idea behind our sampling method. A random number is selected between 0 and 1. If it is less than $Z^{-1}(\omega)$ , then the action $n$ is zero. Otherwise, the action is one.	89
5.3	Results for different values of the source-drain voltage (where $eV = 2\mu_L = \mu_L - \mu_R$ ). Inverse temperature is $\beta = 3.0$ . All numbers are in units of $\Gamma$ .	96
5.4	Results for different values of the temperature (presented as the inverse temperature $\beta$ in units of $\Gamma$ ). The bias is $\mu_L = -\mu_R = 1.0$ .	97
5.5	Cartoon of the Landauer (resonant-level) problem. A single quantum dot (center) is coupled to two baths, left and right. While the baths are formally continuous, we add the lines to represent the fact that in our semiclassical simulations we discretize the electrodes.	98
5.6	Effect of different gate voltages on the time-dependent current. The bias is $\mu_L = -\mu_R = \Gamma$ and the temperature is $T = \Gamma/3$ .	100
5.7	Effect of different choices of the book-keeping function $f_b(n)$ on the time-dependent total current at temperature $T = \Gamma/3$ , gate voltage $\epsilon_0 = 0$ , and bias $\mu_L = -\mu_R = \Gamma$ .	101
5.8	Effect of different values of $\lambda$ (or equivalently, different choices for the length of the spin vector) on the time-dependent total current at temperature $T = \Gamma/3$ , gate voltage $\epsilon_0 = 0$ , and bias $\mu_L = -\mu_R = \Gamma$ .	102
5.9	Result of different numbers of modes per electrode on the time-dependent total current at temperature $T = \Gamma/3$ , gate voltage $\epsilon_0 = 0$ , and bias $\mu_L = -\mu_R = \Gamma$ .	103
5.10	Convergence of the time-dependent total current with respect to the number of trajectories, for the system parameters of temperature $T = \Gamma/3$ , gate voltage $\epsilon_0 = 0$ , and bias $\mu_L = -\mu_R = \Gamma$ .	104

A.1	Potential, initial wavepacket, and harmonic-width wavepacket for the anharmonic Morse oscillator. . . . .	110
A.2	The “semiclassical gauge” problem: the real part of the survival amplitude for the anharmonic Morse oscillator with the zero of energy at the bottom of the well versus at the dissociation limit. . . . .	111
A.3	Effect of various terms of the HK-IVR expression on the survival amplitude of the anharmonic Morse oscillator. . . . .	113

# List of Tables

4.1	Computational complexity of various methods for calculating the monodromy matrix, assuming the force calculation is a “black box.” The number of degrees of freedom in the system is denoted by $F$ . . . . .	68
4.2	Initial conditions for trajectories on the Hénon-Heiles potential. . . . .	70
A.1	Analytical results for the classical harmonic oscillator. . . . .	109

## Acknowledgments

No single person has had as much influence on my experience as a graduate student as Prof. William H. Miller. It was an honor to have Bill as my research advisor. Under his guidance, I've learned how to explore my own research ideas, as well as learning much from his experience. I've also had the opportunity to learn a lot from Bill in the classroom, both as a student (for 295, 221B, and 223B) and as a graduate student instructor for him in 120A. Bill is a model for how a respected scientist can be humble, yet confident about his work.

It has been a pleasure to get to know the other graduate students in the Miller group during my time here: Sandy Yang, Charu Venkataraman, Nandini Ananth, Mike Small, and Shervin Fatehi. I'm especially happy to have worked with Nandini and Shervin, who became good friends outside the office as well as in it. Nandini's patience with me as I prepared for my qualifying exam, badgering her with my impatient questions, is something for which I will always be grateful. Shervin was always willing to be a sounding board for my ideas. Few of those ideas went anywhere, but without Shervin there as a sanity check, I most certainly would have spent more time on ideas that failed and less time on ideas that succeeded.

I've also had the opportunity to get to know a number of excellent post-docs: Yimin Li, Tommy Miller, Cristian Predescu, Atsushi Horikoshi, Richard Stein, Guohua Tao, Shaohui Zheng, Jian Liu, and Bin Li. Of those, I was particularly fortunate to work with Cristian (although our project together is not included in this dissertation) and to have many informative conversations with Jian.

Any thanks to the Miller group would be remiss if it didn't also acknowledge Cheryn Gliebe, whose guidance through the tangles of the UC and LBL administrative mazes saved me many hours and much anguish.

Of course, no one has had a greater influence on my development, both as a person and as a scientist, than my parents. Although neither of them come from a particularly strong scientific background, they have always gone far out of their way to encourage my interest in science: from celebrating my birthday with a trip to the science museums of Chicago, to sending me off to Alabama for a week of Space Camp, to supporting me financially when I decided I needed a second undergraduate degree in math. What they couldn't teach me directly, they encouraged me to discover on my own, and that attitude is at the heart of research.

As I reach the end of my quarter-century as a student, I find myself reflecting on the path that brought me here and feeling thankful for the people who, knowingly or not, guided me along the way. My grandfather showing me Halley's comet when I was four is one of my first memories of being amazed by science. My father's colleague L. T. Brown, book editor at the Indianapolis News, sent science books to me. My fascination with molecular dynamics was born when I saw the cartoon of carbon burning from Feynman's "Atoms in Motion" in a book that L. T. Brown sent me. My first high school chemistry teacher, Dr. Karen Stetyick, suggested that I join our after-school chemistry "team," and there, under the direction of my second chemistry teacher, Dr. Claire Baker, my understanding of chemistry blossomed. In college, my advisor-in-practice-though-not-in-fact, Prof. Ted Lindeman, made the chemistry department, and my physical chemistry classes in particular, into something I associated as much with fun as with work. My first (and somewhat accidental) foray into theoretical chemistry during a summer working for Prof. Jeff Cina opened the world of theory to me. The next summer, working for Prof. Jean-Claude Rayez and

Dr. Laurent Bonnet, I began to really learn about chemical dynamics. My summers working with Prof. Cliff Dykstra taught me a lot about the practical process of theoretical research, and his practical advice about graduate school and about becoming a scientist has helped me immensely.

All of these people played roles in directing me along the specific and fortunate path I've followed. Many other excellent teachers helped prepare me in general, and three in particular helped me through difficult times in my youth: Mrs. Maria Nichols, Mr. Patrick Leonard, and Mrs. Mary Jo Wright.

While those people prepared me to attend Berkeley, many others have made my time in Berkeley more enjoyable. I've already mentioned Nandini and Shervin, whose friendship outside the office meant as much to me as our interactions in the office. My fond memories of graduate school will include drinking Scotch and losing chess games with Paul Crider, and chatting (sometimes ranting) over coffee with Lauren Comfort and Janel Uejio. Sarah Godsey has been another good friend and source of support. For the last year, I've been fortunate to have Natania Antler in my life.

I've also benefitted from the way my high school friends helped me anchor the person I've become to the person I wanted to become. For this, I'm particularly grateful to Steve Okey, Kara Glennon, and Sabrina Bingham Summers.

In the fall of 2008, I had the opportunity to take a semester at D. E. Shaw Research, and that time had a profound influence on me. Here I must again thank Cristian Predescu, who suggested that internship. All of the work contained in this thesis was started after my internship at DESRES. I don't think that is a coincidence: I think that my scientific abilities and my confidence in approaching problems matured substantially while at DESRES. I also had a wonderful time there, and I'd particularly like to thank my manager, John Klepeis, and my office-mates Greg Minton, Dan Arlow, John Jumper, and Daniel Shenfeld.

A couple of chapters need acknowledgment sections of their own. I learned about the "precision shooting" method, which inspired chapter 4, from my DESRES phone interview with Paul Maragakis. Michael Grünwald was also extremely helpful as I was trying to translate his work into an approach to calculate the monodromy matrix.

Chapter 5 came about because Eran Rabani suggested that we might be able to find a way to treat molecular conduction semiclassically, and he was very active in the development of the ideas contained in that chapter. His students, Tal Levy and Guy Cohen, were also instrumental in helping me understand the quantum side of that problem. The quantum results presented in that chapter were calculated by Tal Levy.

# Preface

If the goal of science is to understand the world around us, then simulation is the ultimate test of that understanding. A theory is just a hunch until it has numbers to back it up, and frequently those numbers come from simulations. By reproducing experimental observations in simulations, we show that the theories upon which we base our understanding are consistent with reality. By simulating phenomena that we have yet to see, we can direct experiments in interesting new directions. Perhaps most importantly, simulations allow us to gain a deeper understanding of experimental results, because simulations don't suffer from the physical limitations of experiments.

The work in this thesis is focused on a small area in the global picture of simulation: the simulation of the motion of atoms and molecules. I take a small sideline into the motion of electrons as well, but all of this work is united by the goal of simulating molecular behavior through semiclassical methods.

## The Semiclassical Approach

As far as the field of chemistry is concerned, nonrelativistic quantum mechanics is exact.\* Unfortunately, the quantum mechanical motion of systems of many atoms is too difficult of a problem to simulate exactly. In fact, the problem is so difficult that despite the rapid development of faster and faster computers, quantum simulations of more than a few atoms remain beyond our reach.

On the other hand, modern computers are quite adept at simulating classical mechanics. The classical simulation of millions of particles is feasible. However, not all important chemical effects can be captured by classical mechanics.

Chemistry exists on the border between quantum and classical mechanics. We generally don't need the full power of quantum mechanics to describe the motion of atoms and molecules. However, many important effects exist which aren't captured by classical mechanics — we need at least some treatment of the quantum effects.

This is where semiclassical theory comes in. It provides a middle ground between quantum treatments and classical treatments. Semiclassical theories are approximations to quantum mechanics that are based on classical dynamics. We take some of the best from both worlds: semiclassical methods get some of the accuracy of quantum mechanics while requiring far fewer computational resources to run a simulation. The fact that methods based on the less accurate theory (classical mechanics) can be used to capture effects from the more accurate theory

---

\* With a few exceptions when it comes to explaining the behavior of electrons in very large atoms.

(quantum mechanics) is one of the fascinating features of semiclassical dynamics.

Of course, we'd still like to make semiclassical methods even more efficient. Much of this dissertation is motivated by efforts to develop more efficient ways of calculating the semiclassical expressions described in chapter 1. However, semiclassical theory also provides excellent interpretational tools. Even when the methods I developed were not more efficient than existing methods, they provided insights into the nature of quantum effects. Semiclassical methods are particularly useful for interpretation because they are based on classical dynamics, which tends to be closer to human intuition. I have also worked to expand the range of problems which can be treated semiclassically.

## Thesis Outline

This thesis is structured in three main parts: literature review, techniques to improve the efficiency of existing methodologies, and new methodologies (with applications). The literature review is entirely contained in chapter 1.

Chapters 2, 3, and 4 show attempts to make SC-IVR calculations more efficient. Chapters 2 and 3 focus on the goal of reducing the number of trajectories that are required to converge a semiclassical calculation. Chapter 2 provides a method for the Monte Carlo sampling of a time-dependent integrand, which allows us to ignore many of the trajectories which are unimportant to the overall integral. Chapter 3 takes a somewhat related idea, but considers the histogram of the phase which result from these trajectories, and considers what we can learn from that picture. Although these two methods are very similar, they aren't mutually exclusive. It would be relatively easy to combine them, although we do not explore that here.

In chapter 4, we switch from Monte Carlo to the semiclassical prefactor. In particular, we develop a new way to calculate the monodromy matrix that does not require calculation of the Hessian, and which aims for a sweet spot between being more accurate than a fast (but error-prone) treatment of the monodromy matrix and the slower (but accurate) methods for calculating the monodromy matrix.

Chapter 5 marks the turning point toward new applications. The previous chapters found ways to improve the implementation of the ideas in chapter 1; this chapter aims to go beyond those ideas and to develop semiclassical techniques that will apply to new fields. Motivated by an interest in molecular electronics, we returned to a neglected idea on how to treat second-quantized fermions semiclassically. After making a few essential improvements on the idea, we tested it against a simple model of a molecular transistor, and we obtained excellent results when compared to the exact quantum treatment of the same system.

We close with a few concluding thoughts on the progress made by the work contained in these chapters, and on the directions that this work suggests for future exploration.

# Chapter 1

## Introduction to Semiclassical Methods

Efforts to study the connections between quantum mechanics and classical mechanics are as old as quantum theory. In fact, the first semiclassical approximation to Schrödinger's wavefunction (the WKB approximation) was published within six months of Schrödinger's paper presenting the wavefunction formalism<sup>1</sup> — what's more, the idea was submitted independently by three authors over the course of a few months: by Wentzel (June 1926),<sup>2</sup> Brillouin (July 1926),<sup>3</sup> and Kramers (September 1926).<sup>4</sup>

The semiclassical methods discussed herein share some spirit with that original semiclassical method (in that they extract quantum information from fundamentally classical mechanics, and that the classical action frequently acts to tie the quantum to the classical). But these methods go far beyond the WKB method. The WKB approximation applies to the time-independent treatment of one-dimensional systems. The methodologies we discuss in this dissertation are applicable to multi-dimensional time-dependent phenomena.

This chapter will review the background material on semiclassical initial value representations (SC-IVRs) and some related methodologies in order to lay the framework on which later chapters are built.

### 1.1 Semiclassical Propagators

The WKB theory is an approximation for time-independent problems; if we are interested in time-dependent problems, it is necessary to develop an approximation for the quantum time-evolution operator. The SC-IVR provides two main approximations. Both IVRs have the same basic mathematical form:

$$e^{-i\hat{H}t/\hbar} \approx \int dq_0 \int dp_0 e^{iS(q_0, p_0; t)/\hbar} \mathcal{C}(q_0, p_0; t) |\chi(q_0, p_0; t)\rangle \langle \chi(q_0, p_0)| \quad (1.1)$$

where  $S(q_0, p_0; t)$  is the classical action for a trajectory evolved to time  $t$  from initial conditions  $(q_0, p_0)$ , and  $\mathcal{C}(q_0, p_0; t)$  is a prefactor which is determined by the choice of state  $|\chi\rangle$ . When  $|\chi\rangle$  is a position (or momentum) state, the IVR is called the Van Vleck IVR. When  $|\chi\rangle$  is a coherent

state, the IVR is known as the Herman-Kluk IVR. Both of these are described in more detail below.

Henceforth, the dependence of quantities such as  $S$  and  $\mathcal{C}$  on the initial conditions will be implicit, and they will be subscripted by the time parameter. That is to say, we will write  $S_t$  in place of  $S(q_0, p_0; t)$ ,  $\mathcal{C}_t$  in place of  $\mathcal{C}(q_0, p_0; t)$ , and similarly  $|\chi_t\rangle$ , etc.

### 1.1.1 The Van Vleck IVR

The position state IVR is called the Van Vleck IVR because of the connection of the position state IVR's prefactor to a determinant discussed by Van Vleck in a paper from 1928.<sup>5</sup> One easy derivation of the Van Vleck propagator (obviously not available to Van Vleck in 1928!) starts by taking the stationary phase approximation to the Feynman path integral propagator.

The propagator for the Feynman path integral<sup>6,7</sup> to get from position state  $|x_0\rangle$  to position state  $|x_N\rangle$  in time  $t$  is of the form:

$$\langle x_N | e^{-i\hat{H}t/\hbar} | x_0 \rangle = \lim_{N \rightarrow \infty} \left( \frac{Nm}{2\pi i \hbar t} \right)^{N/2} \int dx_N \cdots \int dx_0 e^{iS_N(x)/\hbar} \quad (1.2)$$

with

$$S_N(x) = \frac{Nm}{2t} \sum_{j=1}^N (x_j - x_{j-1})^2 - \frac{t}{N} \sum_{j=1}^N V(x_j) \quad (1.3)$$

The stationary phase approximation assumes that most of the contribution to the integral of an oscillatory function occurs at the points where the oscillatory function is at extrema. The phase function is Taylor-expanded to second order around those points, and the resulting Gaussian integral can be performed analytically. Mathematically, the stationary phase approximation in one dimension is:

$$\int dx e^{if(x)} \approx \sum_{\{a|f'(a)=0\}} \sqrt{\frac{2\pi i}{f''(a)}} e^{if(a)} \quad (1.4)$$

In multiple dimensions, the second derivative is a second derivative matrix, and the stationary phase approximation has the determinant of the second derivative matrix.

In order to apply the stationary phase approximation to equation (1.2), we must find the roots of the first derivative of the phase, and the value of the second derivative of the phase at those roots. The one subtle point here is that, any  $x_i$  appears in two terms of the sum  $\sum_j (x_j - x_{j-1})^2$ : one when  $i = j$ , and one when  $i = j - 1$ . With this warning, we calculate the stationary phase condition for each  $x_i$ :

$$0 = \frac{\partial S_N}{\partial x_i} = \frac{\partial}{\partial x_i} \left( \frac{Nm}{2t} \left( (x_i - x_{i-1})^2 + (x_{i+1} - x_i)^2 \right) - \frac{t}{N} V(x_i) \right) \quad (1.5)$$

$$= \frac{Nm}{t} (2x_i - x_{i-1} - x_{i+1}) - \frac{t}{N} V'(x_i) \quad (1.6)$$

If we define  $\Delta t \equiv t/N$ , we can show that this gives us the finite difference expression for Newton's equation:

$$-V'(x_i) = m \frac{x_{i+1} + x_{i-1} - 2x_i}{\Delta t^2} \approx m\ddot{x}_i \quad (1.7)$$

This has to be true at each time slice, which means that satisfying the stationary phase condition is the same as selecting the classical paths.

Therefore, we can plug the stationary phase approximation (1.4) in for the Feynman path integral expression in equation (1.2) and we obtain:

$$\left\langle x_N \left| e^{-i\hat{H}t/\hbar} \right| x_0 \right\rangle \approx \lim_{N \rightarrow \infty} \sum_{\text{paths}} \sqrt{\left( \frac{m}{\Delta t} \right)^N \frac{1}{2\pi i \hbar} \left| \frac{\partial^2 S_N}{\partial x_i \partial x_j} \right|^{-1}} e^{iS_N/\hbar} \quad (1.8)$$

where the sum is over discretized paths that satisfy the classical equations of motion at each discrete point.

Note that the second derivative from the stationary phase approximation will become our prefactor. Since our phase is the action, the stationary phase condition thus selects the classical path. The second derivative captures the curvature of our Gaussian approximation, and therefore we consider the physical meaning of the prefactor to be capturing some of the quantum dynamical fluctuations about the classical path.

At this point, we observe that the action  $S$  as it appears above is actually a function of all the positions  $\{x_0, \dots, x_N\}$  (although the derivatives are only over  $\{x_1, \dots, x_N\}$ ). Since we're considering the sum over classical paths, this is redundant. For a given potential energy surface, the set of classical paths (which we sum over) is specified by the initial position  $x_0$ , the final position  $x_N$ , and the time  $t$  separating them. So instead of having the action be a function of all positions  $S_N(x_0, \dots, x_N)$ , we would like to be able to write it as a function of just initial and final position,  $S(x_N, x_0)$ .

This is trivial when the action appears in the exponent: the value of  $S$  should be the same no matter how it is calculated. However, it is notably non-trivial to do this for the determinant of the second derivative matrix. In both cases, the equation for the action can be written as in equation (1.3), but I will write it as  $S_N$  if the intermediate variables  $\{x_1, \dots, x_{N-1}\}$  are independent, and  $S$  if only  $x_0$  and  $x_N$  are independent variables.

Since we know we'll have a second-derivative matrix, but with independent variables  $x_0$  and  $x_N$ , we assume that we'll be interested in the second derivatives with respect to those variables. In particular, the cross-derivative, based on equation (1.3) (taking the derivative with respect to  $x_0$  first) is:

$$\frac{\partial^2 S}{\partial x_N \partial x_0} = -\frac{m}{\Delta t} \frac{\partial x_1}{\partial x_N} \quad (1.9)$$

where we recall that all the  $x_i$  such that  $i \in \{1, \dots, N-1\}$  are now functions of  $x_N$ , and that  $x_0$  and  $x_N$  are independent variables. From here, our goal is to solve for  $\frac{\partial x_1}{\partial x_N}$  in terms of the second derivative matrix which appears in our determinant in equation (1.8).

Assume that the first derivative satisfies the stationary phase condition (*i.e.*, is zero, giving us a classical trajectory), the second derivative for all other degrees of freedom  $i$  is

$$\frac{\partial^2 S}{\partial x_N \partial x_i} = 2 \frac{\partial x_i}{\partial x_N} - \frac{\partial x_{i+1}}{\partial x_N} - \frac{\partial x_{i-1}}{\partial x_N} - \frac{\Delta t^2}{m} V''(x_i) \frac{\partial x_i}{\partial x_N} \quad (1.10)$$

where, for  $i = 1$ , the term  $\frac{\partial x_{i-1}}{\partial x_N}$  vanishes (because  $x_0$  and  $x_N$  are independent) and for  $i = N-1$

the term  $\frac{\partial x_{i+1}}{\partial x_N}$  is unity. This can also be written as

$$\frac{\partial^2 S}{\partial x_N \partial x_i} = \sum_j K_{i,j} \frac{\partial x_j}{\partial x_N} - \delta_{i,N-1} \quad (1.11)$$

$$\frac{\partial^2 S}{\partial x_N \partial x} = \mathbf{K} \frac{\partial x}{\partial x_n} - \mathbf{1}_{N-1} \quad (1.12)$$

where the second equation is matrix-vector multiplication and subtraction of  $\mathbf{1}_{N-1}$ , a vector where the  $N-1$ th element equals 1 and all other elements equal to 0, and with the matrix  $\mathbf{K}$  given by

$$\mathbf{K} = \begin{pmatrix} 2 - \frac{\Delta t^2}{m} V''(x_1) & -1 & 0 & \cdots & 0 \\ -1 & 2 - \frac{\Delta t^2}{m} V''(x_2) & -1 & \cdots & 0 \\ \vdots & \ddots & \ddots & \ddots & \vdots \\ 0 & 0 & \cdots & -1 & 2 - \frac{\Delta t^2}{m} V''(x_{N-1}) \end{pmatrix} \quad (1.13)$$

Note that this matrix  $\mathbf{K}$  is proportional to the second derivative matrix  $\frac{\partial^2 S_N}{\partial x_i \partial x_j}$ , which appears in equation (1.8).

Since the path (and therefore the action) is determined by the initial and final positions (to within the set of classical solutions), it should be independent of the intermediate points  $x_i$ . This means that its derivative with respect to them should be zero (as should a further differentiation with respect to  $x_N$ ). Therefore, equation (1.12) becomes

$$\frac{\partial x}{\partial x_N} = \mathbf{K}^{-1} \mathbf{1} \quad (1.14)$$

Since only the last element of  $\mathbf{1}_{N-1}$  is nonzero (and it is 1), this tell us that  $\frac{\partial x}{\partial x_N}$  is given by the last column of  $\mathbf{K}^{-1}$ .

*A fortiori*, if we can get all the elements of the vector  $\frac{\partial x}{\partial x_N}$ , we can get the first element, which is what we were looking for. However, we can extract just the first element by using the rule

$$A_{ij}^{-1} = \frac{(-1)^{i+j} m_{ji}}{\det(\mathbf{A})} \quad (1.15)$$

where  $m_{ji}$  is the determinant of the matrix formed by removing the  $j$ th row and the  $i$ th column from  $\mathbf{A}$ .

In this case, we want:

$$\frac{\partial x_1}{\partial x_N} = K_{1,N-1}^{-1} = \frac{(-1)^N m_{N-1,1}}{\det(\mathbf{K})} \quad (1.16)$$

where  $m_{N-1,1}$  is given by

$$m_{N-1,1} = \det \begin{pmatrix} -1 & 2 - \frac{\Delta t^2}{m} V''(x_2) & -1 & \cdots & 0 \\ 0 & -1 & 2 - \frac{\Delta t^2}{m} V''(x_3) & \cdots & 0 \\ \vdots & \ddots & \ddots & \ddots & \vdots \\ 0 & 0 & \cdots & -1 & 2 - \frac{\Delta t^2}{m} V''(x_{N-2}) \\ 0 & 0 & \cdots & 0 & -1 \end{pmatrix} \quad (1.17)$$

This is an  $N - 2 \times N - 2$  upper-triangular matrix, so its determinant is the product of its diagonal elements (which, in this case, are all  $-1$ ). Thus we have

$$m_{N-1,1} = (-1)^{N-2} \quad (1.18)$$

and

$$\frac{\partial x_1}{\partial x_N} = \frac{(-1)^{2N-2}}{\det(\mathbf{K})} = \frac{1}{\det(\mathbf{K})} = \left| \frac{\partial^2 S_N}{\partial x_i \partial x_j} \right|^{-1} \quad (1.19)$$

Inserting this into equation (1.9), we find

$$\left| \frac{\partial^2 S_N}{\partial x_i \partial x_j} \right|^{-1} = - \left( \frac{\Delta t}{m} \right)^N \frac{\partial^2 S}{\partial x_N \partial x_0} \quad (1.20)$$

Substituting this in equation (1.8), we get

$$\langle x_N | e^{-i\hat{H}t/\hbar} | x_0 \rangle \approx \sum_{\text{paths}} \sqrt{\frac{-1}{2\pi i \hbar} \frac{\partial^2 S}{\partial x_N \partial x_0}} e^{iS_t/\hbar} \quad (1.21)$$

Now we'll rewrite that second derivative in terms of initial conditions. The trick for this is to remember that  $x_N$  can also be seen as a function of  $x_0$  and the initial classical momentum,  $p_0$ . As such, we can formally write the derivative

$$\left( \frac{\partial S(x_N, x_0)}{\partial x_0} \right)_{p_0} = \frac{\partial S(x_N, x_0)}{\partial x_N} \frac{\partial x_N(p_0, x_0)}{\partial x_0} + \frac{\partial S(x_N, x_0)}{\partial x_0} \quad (1.22)$$

However, we know that the action is defined as the integral of the Lagrangian. So we write that derivative in those terms, and use Hamilton's equations of motion to integrate it by parts:

$$\frac{\partial S(x_N(p_0, x_0), x_0)}{\partial x_0} = \frac{\partial}{\partial x_0} \int_0^t dt' p_{t'} \dot{x}_{t'} - H(p_0, x_0; t) \quad (1.23)$$

$$= \int_0^N dt' \frac{\partial p_{t'}}{\partial x_0} \dot{x}_{t'} + p_{t'} \frac{d}{dt'} \frac{\partial x_{t'}}{\partial x_0} - \dot{x}_{t'} \frac{\partial p_{t'}}{\partial x_0} - \dot{p}_{t'} \frac{\partial x_{t'}}{\partial x_0} \quad (1.24)$$

$$= \int_0^N dt' p_{t'} \frac{d}{dt'} \frac{\partial x_{t'}}{\partial x_0} - \dot{p}_{t'} \frac{\partial x_{t'}}{\partial x_0} \quad (1.25)$$

$$= p_N \frac{\partial x_N}{\partial x_0} - p_0 \quad (1.26)$$

By identifying this with equation (1.22), we get the results

$$\frac{\partial S}{\partial x_N} = p_N \quad (1.27a)$$

$$\frac{\partial S}{\partial x_0} = -p_0 \quad (1.27b)$$

Inserting the second of these equations into the second derivative in equation (1.21), we rewrite it in the form

$$\frac{\partial^2 S}{\partial x_N \partial x_0} = \frac{\partial}{\partial x_N} \frac{\partial S}{\partial x_0} = -\frac{\partial}{\partial x_N} p_0 = -\left(\frac{\partial x_N}{\partial p_0}\right)^{-1} \quad (1.28)$$

Putting this into equation (1.21) (and generalizing to multiple dimensions by changing the derivative to its determinant), we obtain the primitive semiclassical result:

$$\langle x_N | e^{-i\hat{H}t/\hbar} | x_0 \rangle \approx \sum_{\text{paths}} \sqrt{\frac{1}{2\pi i\hbar} \left| \frac{\partial q_t}{\partial p_0} \right|^{-1}} e^{iS_t/\hbar} \quad (1.29)$$

This expression for the propagator has been derived several times. Our derivation is linked to that of Miller.<sup>8</sup> Another derivation based on path integrals is given by Gutzwiller.<sup>9</sup> Although it was one of the first practical semiclassical propagators, its usefulness is limited by a couple of factors. First, the quantity  $\partial q_t / \partial p_0$  can clearly approach zero. When this occurs, the propagator goes to infinity. Second, the problem of finding all possible paths connecting two positions in time  $t$  is nontrivial for all but the simplest of systems. In general there are many different initial momenta which can solve that problem.

The initial value representation solves this “root-search” problem by changing the variables of integration to initial conditions, which determine a unique classical path. A key insight is that, in general, the object of interest is not the coordinate representation propagator (which connects specific points  $q_0$  and  $q_t$ ) but the time-evolution operator (which can connect any point with its corresponding time-evolved positions).

Mathematically, we begin with the time evolution operator and add a resolution of the identity in position eigenkets before and after the time evolution. Recalling that the position  $q_t$  can be seen as a classically time-evolved position beginning at  $q_0$  with some initial momentum  $p_0$ , we invoke Liouville’s theorem in order to make the appropriate change of variables.

$$e^{-i\hat{H}t/\hbar} = \int dq_0 \int dq_t |q_t\rangle \langle q_t| e^{-i\hat{H}t/\hbar} |q_0\rangle \langle q_0| \quad (1.30)$$

$$= \int dq_0 \int dp_0 \left| \frac{\partial q_t}{\partial p_0} \right| |q_t\rangle \langle q_t| e^{-i\hat{H}t/\hbar} |q_0\rangle \langle q_0| \quad (1.31)$$

We should note that in the second line,  $q_t$  is really the function  $q(q_0, p_0; t)$ . With this, we have introduced a theme which runs through all of semiclassical theory: the time-evolved phase space is determined through classical dynamics, but the results of those classical dynamics (such as the time-evolved positions above) are treated as inputs to quantum and semiclassical formulae.

Figure 1.1 gives a visual explanation of the initial value idea. The curve traces the path of possible initial momenta and final positions (at a fixed time) from a given initial position, for some hypothetical system. The horizontal line demonstrates that more than one trajectory can connect the initial position to a given final position in a certain amount of time (it intersects the curve twice). However, no such line can be drawn vertically — we know the positions and momenta at  $t = 0$ , and so, as Laplace would have it, “the future, like the past, is an open book.”

We can immediately insert the Van Vleck expression (1.29) into our IVR (1.31), and the IVR Jacobian has the convenient side effect that it removes the singularities from the prefactor.

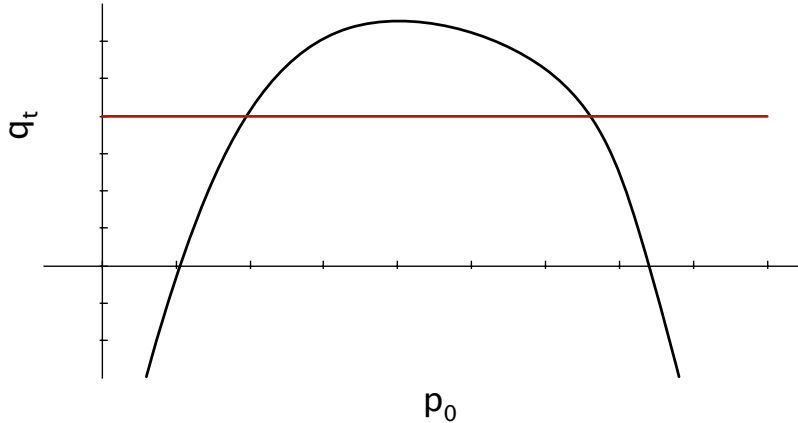


Figure 1.1: The IVR “Trick”: The black curve takes a given initial position  $q_0$  for some hypothetical system and shows possible final positions  $q_t$  reached from different initial momenta. The red line highlights the fact that a given  $q_t$  can be reached from more than one  $p_0$ . The initial value representation switches the axis of integration from  $q_t$  to  $p_0$ .

The final result (generalized to a system with  $F$  degrees of freedom) is known as the Van Vleck Initial Value Representation:

$$e^{-i\hat{H}t/\hbar} \approx \int dq_0 \int dp_0 e^{iS_t/\hbar} \sqrt{\frac{\det(\partial q_t / \partial p_0)}{(2\pi i\hbar)^F}} |q_t\rangle \langle q_0| \quad (1.32)$$

### 1.1.2 The Herman-Kluk IVR

The most commonly used semiclassical IVR propagator is probably the coherent state, or Herman-Kluk, version. It can be derived in several ways; here we’ll consider Miller’s derivation,<sup>10</sup> which is based on using the “modified Filinov filtering” method<sup>11,12</sup> on the primitive semiclassical expression given in equation (1.29). The original derivation of Herman and Kluk<sup>13</sup> follows a similar mathematical path, although we find the physical description in Miller’s derivation to be more elegant. Hermak and Kluk make a specific change of variables which corresponds to Miller’s choice of parameter, but the reason for that choice (we regain an expression in terms of the overlaps of coherent states) is more easily seen in Miller’s derivation. Further, since the Herman-Kluk is seen as a specific choice of parameter in Miller’s derivation, it is more general than the Herman and Kluk’s derivation.

The modified Filinov filtering method which serves as the basis of Miller’s derivation involves multiplying by 1 in the form of a normalized Gaussian integral, and then expanding the phase of the original integrand to second order about the integration variable from the added integral. Then the order of integration is switched: the original variable is integrated out, and the expression is left in terms of the newly added integration.

We start by noting the identity

$$1 = \int_{\mathbb{R}} dx \sqrt{\frac{A}{\pi}} \exp(-A(x - x_0)^2) \quad (1.33)$$

which we insert into the arbitrary integral  $I$ :

$$I = \int_{\mathbb{R}} dx_0 e^{i\phi(x_0)} \quad (1.34)$$

$$= \int_{\mathbb{R}} dx_0 \int_{\mathbb{R}} dx \sqrt{\frac{A}{\pi}} e^{-A(x-x_0)^2} e^{i\phi(x_0)} \quad (1.35)$$

Now we replace  $\phi(x_0)$  with its second-order Taylor expansion around  $x$ . The argument is that for any given  $x$ , this will be reasonable since the Gaussian  $\exp(-A(x - x_0)^2)$  makes it so that values of  $x_0$  near  $x$  will dominate.

$$I \approx \int_{\mathbb{R}} dx_0 \int_{\mathbb{R}} dx \sqrt{\frac{A}{\pi}} e^{-A(x-x_0)^2} e^{i(\phi(x) + \phi'(x)(x_0 - x) + \frac{1}{2}\phi''(x)(x_0 - x)^2)} \quad (1.36)$$

$$\approx \int_{\mathbb{R}} dx_0 \int_{\mathbb{R}} dx \sqrt{\frac{A}{\pi}} e^{-(A - \frac{i}{2}\phi''(x))(x_0 - x)^2 + i\phi'(x)(x_0 - x) + \phi(x)} \quad (1.37)$$

Now we perform the integration over  $x_0$ :

$$I \approx \int_{\mathbb{R}} dx \sqrt{\frac{A}{A - \frac{i}{2}\phi''(x)}} \exp\left(-\phi'(x)^2 / \left(4\left(A - \frac{i}{2}\phi''(x)\right)\right)\right) \quad (1.38)$$

Makri and Miller<sup>12</sup> noted that the identity (1.33) is true even if  $A$  is complex, and that it remains approximately true if  $A$  is a function of  $x$ . Therefore, they suggested selecting  $A$  (which can be chosen arbitrarily according to the identity (1.33)) as  $A = \frac{1}{2}(i\phi''(x) + \frac{1}{c})$ . When we use this choice of  $A$  in equation (1.38), we obtain the result:

$$\int_{\mathbb{R}} dx_0 \exp(i\phi(x)) \approx \int_{\mathbb{R}} dx (1 + ic\phi''(x))^{1/2} \exp\left(-\frac{c}{2}\phi'(x)^2 + i\phi(x)\right) \quad (1.39)$$

This is the fundamental result of the modified Filinov method. In particular, it's worth noting that this result is just the original integrand (now over the variable  $x$ , instead of  $x_0$ ) multiplied by the damping factor  $(1 + ic\phi''(x))^{-1/2} \exp(-\frac{c}{2}\phi'(x)^2)$ .

The result shown here is for one dimension. The generalization to multiple dimensions is trivial: the constant  $c$  becomes a constant matrix in the exponent (sandwiched between the row and column vector forms of  $\phi'(x)$ ) and the prefactor is a determinant.

Miller's derivation of the Herman-Kluk IVR starts by considering the propagation from a coherent state  $|\psi_i\rangle$  to a coherent state  $|\psi_f\rangle$ , both of width  $\gamma$ , using the primitive semiclassical approximation (1.29) to the time-evolution operator:

$$\langle \psi_f | e^{-i\hat{H}t} | \psi_i \rangle = \int dq_t \int dq_0 \langle \psi_f | q_t \rangle \left(2\pi i \frac{\partial q_t}{\partial p_0}\right)^{-1/2} e^{iS_t} \langle q_0 | \psi_i \rangle \quad (1.40)$$

The (complex) phase (except for the prefactor,  $\left(2\pi i \frac{\partial q_t}{\partial p_0}\right)^{-1/2}$ ), is given by

$$\phi(q_t, q_0) = S_t(q_t, q_0) + p_i(q_0 - q_i) - p_f(q_t - q_f) + \frac{i\gamma}{2} ((q_t - q_f)^2 + (q_0 - q_i)^2) \quad (1.41)$$

For the Filinov expression, we'll need the first and second derivatives with respect to  $q_0$  and  $q_t$ :

$$\frac{d\phi}{dq_t} = \frac{d}{dq_t} S_t(q_t, q_0) - p_f + i\gamma(q_t - q_f) \quad (1.42)$$

$$= p_t - p_f + i\gamma(q_t - q_f) \quad (1.43)$$

where the second equality comes from equation (1.27a). For the first derivative with respect to  $q_0$ :

$$\frac{d\phi}{dq_0} = p_i - p_0 + i\gamma(q_0 - q_i) \quad (1.44)$$

The second derivative matrix is given by

$$\begin{pmatrix} \frac{\partial^2 \phi}{\partial q_t^2} & \frac{\partial^2 \phi}{\partial q_0 q_t} \\ \frac{\partial^2 \phi}{\partial q_t q_0} & \frac{\partial^2 \phi}{\partial q_0^2} \end{pmatrix} = \begin{pmatrix} \frac{\partial p_t}{\partial q_t} + i\gamma & \frac{\partial p_t}{\partial q_0} \\ -\frac{\partial p_0}{\partial q_t} & -\frac{\partial p_0}{\partial q_0} + i\gamma \end{pmatrix} \quad (1.45)$$

With those necessary preliminaries, we consider what happens when we apply the modified Filinov approximation (1.39) to equation (1.40), under the approximation that the prefactor in equation (1.40), which is ruled by the monodromy matrix element  $M_{qp}$ , varies much more slowly than the phase. This approximation allows us to treat that prefactor as a constant while applying the modified Filinov approximation to the rest of the integrand. Therefore, the complex phase to which we apply the modified Filinov approximation is  $\phi(q_0, q_t)$  as defined above.

We'll assume that the Filinov parameter  $\mathbf{c}$  is diagonal; *i.e.*,

$$\mathbf{c} = \begin{pmatrix} c_1 & 0 \\ 0 & c_0 \end{pmatrix} \quad (1.46)$$

In this case, the Filinov modification's damping exponent  $\phi_{\text{Folini}}$  is

$$\phi_{\text{Folini}} = -\phi'(p_t, q_0)^T \cdot \frac{\mathbf{c}}{2} \cdot \phi'(q_t, q_0) \quad (1.47)$$

$$\begin{aligned} &= -\frac{c_1}{2} ((p_t - p_f)^2 + 2i\gamma(p_t - p_f)(q_t - q_f) - \gamma^2(q_t - q_f)^2) \\ &\quad - \frac{c_0}{2} ((p_i - p_0)^2 + 2i\gamma(p_i - p_0)(q_0 - q_i) - \gamma^2(q_0 - q_i)^2) \end{aligned} \quad (1.48)$$

and the Filinov damping prefactor  $\mathcal{C}_{\text{Filinov}}$  is given according to

$$\mathcal{C}_{\text{Filinov}}^2 = \det \left( \mathbf{1} + i\mathbf{c} \begin{pmatrix} \frac{\partial^2 \phi}{\partial q_t^2} & \frac{\partial^2 \phi}{\partial q_0 q_t} \\ \frac{\partial^2 \phi}{\partial q_t q_0} & \frac{\partial^2 \phi}{\partial q_0^2} \end{pmatrix} \right) \quad (1.49)$$

$$= \det \begin{pmatrix} 1 + ic_0 \frac{\partial p_t}{\partial q_t} - c_0 \gamma & ic_0 \frac{\partial p_t}{\partial q_0} \\ -ic_1 \frac{\partial p_0}{\partial q_t} & 1 - ic_1 \frac{\partial p_0}{\partial q_0} - c_1 \gamma \end{pmatrix} \quad (1.50)$$

$$= \left( 1 + ic_0 \frac{\partial p_t}{\partial q_t} - c_0 \gamma \right) \left( 1 - ic_1 \frac{\partial p_0}{\partial q_0} - c_1 \gamma \right) - \left( ic_0 \frac{\partial p_t}{\partial q_0} \right) \left( -ic_1 \frac{\partial p_0}{\partial q_t} \right) \quad (1.51)$$

$$= (1 - c_0 \gamma) (1 - c_1 \gamma) - ic_1 \frac{\partial p_0}{\partial q_0} (1 - c_0 \gamma) + ic_0 \frac{\partial p_t}{\partial q_t} (1 - c_1 \gamma) \\ + c_0 c_1 \left( \frac{\partial p_t}{\partial q_t} \frac{\partial p_0}{\partial q_0} - \frac{\partial p_0}{\partial q_t} \frac{\partial p_t}{\partial q_0} \right) \quad (1.52)$$

Now we express the partial derivatives which appear in the damping prefactor in terms of the initial conditions. There are three main tricks used here:

$$\left( \frac{\partial x}{\partial y} \right)_w = \left( \frac{\partial x}{\partial z} \right)_w \left( \frac{\partial z}{\partial y} \right)_w \quad (1.53)$$

$$\left( \frac{\partial x}{\partial y} \right)_z = - \left( \frac{\partial x}{\partial z} \right)_y \left( \frac{\partial z}{\partial y} \right)_x \quad (1.54)$$

$$1 = \frac{\partial q_t}{\partial q_0} \frac{\partial p_t}{\partial p_0} - \frac{\partial p_t}{\partial q_0} \frac{\partial q_t}{\partial p_0} \quad (1.55)$$

The first two are standard identities from differential equations. The last is a property of those specific derivatives. It can be shown by noting that the right side of equation (1.55) is the Jacobian determinant of the transformation between  $(q_t, p_t)$  and  $(q_0, p_0)$ . Since that is a canonical transformation, and the volume elements are canonically invariant, the value of the determinant is unity.<sup>14</sup>

The hardest to determine is probably the derivative  $\partial p_t / \partial q_0$ , so we'll show that calculation in its entirety:

$$\frac{\partial p_t(q_t(p_0, q_0), q_0)}{\partial q_0} = \left( \frac{\partial p_t}{\partial q_t} \right)_{q_0} \left( \frac{\partial q_t}{\partial p_0} \right)_{p_0} + \left( \frac{\partial p_t}{\partial q_0} \right)_{q_t} \quad (1.56)$$

$$= \left( \frac{\partial p_t}{\partial q_0} \right)_{p_0} \left( \frac{\partial q_0}{\partial q_t} \right)_{p_0} \left( \frac{\partial q_t}{\partial q_0} \right)_{p_0} - \left( \frac{\partial p_t}{\partial q_t} \right)_{q_0} \left( \frac{\partial q_t}{\partial q_0} \right)_{p_t} \quad (1.57)$$

The portions of the first term which held  $q_0$  constant vanish because  $\frac{\partial p_0}{\partial q_0} = 0$ . So far, we've applied the chain rule and identity (1.54). Now we assume that  $\frac{\partial q_0}{\partial q_t} \frac{\partial q_t}{\partial q_0} = 1$  and we get

$$\frac{\partial p_t(q_t(p_0, q_0), q_0)}{\partial q_0} = \left( \frac{\partial p_t}{\partial q_0} \right)_{p_0} - \left( \frac{\partial p_t}{\partial q_t} \right)_{q_0} \left( \frac{\partial p_0}{\partial q_t} \right)_{q_0} \left( \frac{\partial q_t}{\partial q_0} \right)_{p_0} \quad (1.58)$$

$$= \frac{1}{\partial q_t / \partial p_0} \left( \frac{\partial q_t}{\partial p_0} \frac{\partial p_t}{\partial q_0} - \frac{\partial p_t}{\partial p_0} \frac{\partial q_t}{\partial q_0} \right) \quad (1.59)$$

where once again we have assumed that we can treat the reciprocal of the partial derivative naïvely. Finally, we apply the rule (1.55), and we get our final result:

$$\frac{\partial p_t(q_t, q_0)}{\partial q_0} = \frac{-1}{\partial q_t / \partial p_0} \quad (1.60)$$

After doing similar manipulations on all the derivatives, we obtain:

$$\frac{\partial p_t(q_t, q_0)}{\partial q_t} = \frac{\partial p_t / \partial p_0}{\partial q_t / \partial p_0} \quad (1.61a)$$

$$\frac{\partial p_t(q_t, q_0)}{\partial q_0} = \frac{-1}{\partial q_t / \partial p_0} \quad (1.61b)$$

$$\frac{\partial p_0(q_t, q_0)}{\partial q_t} = \frac{1}{\partial q_t / \partial p_0} \quad (1.61c)$$

$$\frac{\partial p_0(q_t, q_0)}{\partial q_0} = \frac{-\partial q_t / \partial q_0}{\partial q_t / \partial p_0} \quad (1.61d)$$

where we have already shown equation (1.61b). We get equation (1.61a) from a single direct application of the rule (1.53), equation (1.61c) is trivial, and equation (1.61d) is just the direct application of equation (1.54).

Again using (1.55), we have:

$$\frac{\partial p_t}{\partial q_0} \frac{\partial p_0}{\partial q_t} - \frac{\partial p_0}{\partial q_t} \frac{\partial p_t}{\partial q_0} = -\frac{\partial p_t / \partial p_0}{\partial q_t / \partial p_0} \frac{\partial q_t / \partial q_0}{\partial q_t / \partial p_0} + \frac{1}{\partial q_t / \partial p_0^2} \quad (1.62)$$

$$= \frac{1 - \partial p_t / \partial p_0 \cdot \partial q_t / \partial q_0}{\partial q_t / \partial p_0^2} = \frac{-\partial q_t / \partial p_0 \cdot \partial p_t / \partial q_0}{\partial q_t / \partial p_0^2} \quad (1.63)$$

$$= -\frac{\partial p_t / \partial q_0}{\partial q_t / \partial p_0} \quad (1.64)$$

Substituting equations (1.61) and (1.64) in equation (1.52) we obtain:

$$\mathcal{C}_{\text{Filinov}}^2 = (1 - c_0\gamma)(1 - c_1\gamma) + \left(\frac{\partial q_t}{\partial p_0}\right)^{-1} \left( i c_1 \frac{\partial q_t}{\partial q_0} (1 - c_0\gamma) + i c_0 \frac{\partial p_t}{\partial p_0} (1 - c_1\gamma) - c_0 c_1 \frac{\partial p_t}{\partial q_0} \right) \quad (1.65)$$

At this point, we recall how this fits into the overall picture of our propagation from one coherent state to another. We rewrite equation (1.40) to include the modified Filinov approximation:

$$\langle \psi_f | e^{-i\hat{H}t} | \psi_i \rangle \approx \int dq_0 \int dq_t \left(\frac{\gamma}{\pi}\right)^{1/2} \left(2\pi i \frac{\partial q_t}{\partial p_0}\right)^{-1/2} \mathcal{C}_{\text{Filinov}} \exp(i\phi(q_t, q_0) + \phi_{\text{Filinov}}) \quad (1.66)$$

Now we perform the “IVR trick”: we change the (thus far, implicit) sum over paths and integral over final positions into an integral over initial momenta. This transform has the Jacobian matrix  $\partial q_t / \partial p_0$ . The result is

$$\langle \psi_f | e^{-i\hat{H}t} | \psi_i \rangle \approx (2\pi)^{-1} \int dq_0 \int dp_0 \left(-2i\gamma \frac{\partial q_t}{\partial p_0}\right)^{1/2} \mathcal{C}_{\text{Filinov}} \exp(i\phi(q_t, q_0) + \phi_{\text{Filinov}}) \quad (1.67)$$

First we'll calculate the prefactor for this Filinov-filtered Van Vleck (FFVV) IVR:

$$(\mathcal{C}^{\text{FFVV}})^2 = 2\gamma \left( -i(1 - c_0\gamma)(1 - c_1\gamma) \frac{\partial q_t}{\partial p_0} + c_1(1 - c_0\gamma) \frac{\partial q_t}{\partial q_0} + c_0(1 - c_1\gamma) \frac{\partial p_t}{\partial p_0} + i c_0 c_1 \frac{\partial p_t}{\partial q_0} \right) \quad (1.68)$$

Now we'll look at the argument to the exponential (*i.e.*, the complex phase):

$$\phi^{\text{FFVV}} = \phi_{\text{Flinov}} + i\phi(p_0, q_0; t) \quad (1.69)$$

$$\begin{aligned} &= -\frac{c_1}{2} ((p_t - p_f)^2 + 2i\gamma(p_t - p_f)(q_t - q_f) - \gamma^2(q_t - q_f)^2) \\ &\quad - \frac{c_0}{2} ((p_i - p_0)^2 + 2i\gamma(p_i - p_0)(q_0 - q_i) - \gamma^2(q_0 - q_i)^2) \\ &\quad - \frac{\gamma}{2} ((q_t - q_f)^2 + (q_0 - q_i)^2) + ip_i(q_0 - q_i) - ip_f(q_t - q_f) + iS_t(q_0, p_0) \end{aligned} \quad (1.70)$$

$$\begin{aligned} &= -\frac{\gamma}{2}(1 - c_1\gamma)(q_t - q_f)^2 - \frac{\gamma}{2}(1 - c_0\gamma)(q_0 - q_i)^2 - \frac{c_1}{2}(p_t - p_f)^2 - \frac{c_0}{2}(p_0 - p_i)^2 \\ &\quad - ic_1\gamma \left( p_t - \left( 1 - \frac{1}{c_1\gamma} \right) p_f \right) (q_t - q_f) + ic_0\gamma \left( p_0 - \left( 1 - \frac{1}{c_0\gamma} \right) p_i \right) (q_0 - q_i) \\ &\quad + iS_t(q_0, p_0) \end{aligned} \quad (1.71)$$

At this point we have the entirety of what I'm calling the Filinov-filtered Van Vleck IVR. However, the FFVV-IVR leaves the parameter matrix  $\mathbf{c}$  undefined. Miller noted that if one makes the choice

$$c_0 = c_1 = \frac{1}{2\gamma} \quad (1.72)$$

one recovers the Herman-Kluk IVR. The argument of the exponential becomes

$$\begin{aligned} \phi^{\text{HK}} &= iS_t(q_0, p_0) - \frac{\gamma}{4}(q_0 - q_i)^2 - \frac{1}{4\gamma}(p_0 - p_i)^2 + \frac{i}{2}(p_0 + p_i)(q_0 - q_i) \\ &\quad - \frac{\gamma}{4}(q_t - q_f)^2 - \frac{1}{4\gamma}(p_t - p_f)^2 - \frac{i}{2}(p_t + p_f)(q_t - q_f) \end{aligned} \quad (1.73)$$

which gives us

$$\exp(\phi^{\text{HK}}) = \langle \psi_f | \psi_t \rangle e^{iS_t} \langle \psi_0 | \psi_i \rangle \quad (1.74)$$

Under Miller's choice of Filinov parameters (1.72), the Filinov-filtered Van Vleck prefactor given in equation (1.68) becomes the Herman-Kluk prefactor:

$$\mathcal{C}^{\text{HK}} = \det \left( \frac{1}{2} \left( \frac{\partial q_t}{\partial q_0} + \frac{\partial p_t}{\partial p_0} + i\gamma \frac{\partial p_t}{\partial q_0} + \frac{1}{i\gamma} \frac{\partial q_t}{\partial p_0} \right) \right)^{1/2} \quad (1.75)$$

Substituting all of this back into the expression for the propagator between two coherent states, we can easily identify the Herman-Kluk propagator (since the initial and final states  $|\psi_i\rangle$  and  $|\psi_f\rangle$  can be chosen arbitrarily):

$$\langle \psi_f | e^{-i\hat{H}t} | \psi_i \rangle \approx (2\pi)^{-1} \int dq_0 \int dp_0 \mathcal{C}^{\text{HK}} e^{iS_t} \langle \psi_f | \psi_t \rangle \langle \psi_0 | \psi_i \rangle \quad (1.76)$$

$$\approx \left\langle \psi_f \left| \int dq_0 \int dp_0 \mathcal{C}^{\text{HK}} |\psi_t\rangle \langle \psi_0| e^{iS_t} \right| \psi_i \right\rangle \quad (1.77)$$

After generalizing to  $F$  degrees of freedom, the Herman-Kluk approximation to the time-evolution operator is therefore

$$e^{-i\hat{H}t} \approx (2\pi)^{-F} \int dq_0 \int dp_0 e^{iS_t} \mathcal{C}^{\text{HK}} |p_t q_t; \gamma\rangle \langle p_0 q_0; \gamma| \quad (1.78)$$

where the states  $|p q; \gamma\rangle$  are coherent states centered on  $(p, q)$  with width parameter  $\gamma$  and  $\mathcal{C}^{\text{HK}}$  is defined in equation (1.75). Frequently, the width parameter is omitted from the state label. We use the convention

$$\langle x | p q; \gamma \rangle = \left(\frac{\gamma}{\pi}\right)^{1/4} \exp\left(\frac{\gamma}{2}(x - q)^2 + ip(x - q)\right) \quad (1.79)$$

When comparing with other literature, it is important to be aware that other authors will often use a width parameter equal to twice our width,  $2\gamma$ .

### 1.1.3 Implementation of a Semiclassical Propagator

We now have the formalism in place for both versions of the semiclassical propagator, however there remain a few subtleties of implementation worth mentioning.

#### Time Evolution of the Monodromy Matrices

The semiclassical prefactors require knowledge of elements of the monodromy (or stability) matrix. In classical terms, the monodromy matrix measures the sensitivity of the trajectory to changes in the initial conditions. In the context of the SC-IVR, it appears due to the inclusion of quantum fluctuations about the classical path from the Feynman path integral.

The monodromy (or stability) matrix is a  $2F \times 2F$  matrix of derivatives, where each row corresponds to a time evolved dimension in phase space, and each column takes the derivative according to the initial condition of that dimension in phase space. It is typically split into four blocks, which are described using a specific notation:

$$\begin{aligned} M_{qq} &\equiv \frac{\partial q_t}{\partial q_0} & M_{qp} &\equiv \frac{\partial q_t}{\partial p_0} \\ M_{pq} &\equiv \frac{\partial p_t}{\partial q_0} & M_{pp} &\equiv \frac{\partial p_t}{\partial p_0} \end{aligned}$$

The way we have usually calculated the monodromy matrix has been through the time evolution of auxiliary equations for the monodromy matrix. These auxiliary equations are easily determined for each monodromy matrix element. As an example, we sketch out calculation of the time derivative of the monodromy matrix element  $M_{qp} = \frac{\partial q_t}{\partial p_0}$ :

$$\frac{d}{dt} \frac{\partial q_t}{\partial p_0} = \frac{\partial}{\partial p_0} \frac{dq_t}{dt} \quad (1.80)$$

$$= \frac{\partial}{\partial p_0} \frac{\partial H}{\partial p_t} \quad (1.81)$$

$$= \frac{\partial^2 H}{\partial p_t^2} \frac{\partial p_t}{\partial p_0} + \frac{\partial^2 H}{\partial p_t \partial q_t} \frac{\partial q_t}{\partial p_0} \quad (1.82)$$

where we have left implicit the dependence of  $H$  on  $p_t$  and  $q_t$  and used Hamilton's equations to put the time derivative in terms of the Hamiltonian.

If we define the second derivative matrices of the Hamiltonian as

$$(H_{\alpha\beta})_{ij} \equiv \frac{\partial^2 H}{\partial \alpha_i \partial \beta_j} \quad (1.83)$$

where  $i$  and  $j$  are element labels and  $\alpha, \beta \in \{q_t, p_t\}$ , then we can write the results of the analysis described above for all monodromy matrix elements as:

$$\begin{pmatrix} \dot{M}_{qq} & \dot{M}_{qp} \\ \dot{M}_{pq} & \dot{M}_{pp} \end{pmatrix} = \begin{pmatrix} H_{pq} & H_{pp} \\ -H_{qq} & -H_{qp} \end{pmatrix} \begin{pmatrix} M_{qq} & M_{qp} \\ M_{pq} & M_{pp} \end{pmatrix} \quad (1.84)$$

In many cases, the position and momentum dependence of the Hamiltonian is separable: that is, the Hamiltonian can be written as  $H(q, p) = T(p) + V(q)$ , where we usually refer to  $T(p)$  and the kinetic energy and  $V(q)$  as the potential energy.\* When this is the case, obviously  $H_{qp} = H_{pq} = 0$ , and the equation of motion simplifies to:

$$\dot{M} = \begin{pmatrix} 0 & m^{-1} \\ -\nabla\nabla V & 0 \end{pmatrix} M \quad (1.85)$$

where  $m^{-1}$  is the inverse mass matrix (if we have the standard kinetic energy term) and  $\nabla\nabla V$  is the Hessian for the potential energy surface.

Other methods for calculating the monodromy matrix will be discussed in chapter 4.

### The sign of the prefactor: Maslov tracking

As seen in equations (1.32) and (1.75), the semiclassical prefactor is generally the square root of the determinant of a matrix. We expect this quantity to trace a continuous line when plotted in complex space. However, the square root is a multivalued function (*i.e.*,  $\sqrt{4} = \pm 2$ ), and a computer program must choose to only return one of these. Generally, computer implementations of the square root return complex numbers with positive real parts. This means that there is a discontinuity as the radicand crosses the negative real axis. This line of discontinuity is an example of a “branch cut.”

In order to keep the prefactor continuous in time, we must track what is called the Maslov index,  $\nu$ . In this situation, the Maslov index is merely the number of times we have crossed the branch cut. The easiest way to calculate this is to multiply a variable (initially 1) by  $-1$  every time the real part of the radicand is negative and the product of the imaginary part from the previous radicand with the imaginary part of the current radicand is negative. If we let `maslov` be this variable (which equals  $e^{i\pi\nu}$ , not the Maslov index  $\nu$  itself), and let `oldrad` be the old radicand and `rad` be the new radicand, the the following pseudocode implements this idea:

---

\* The reader who is curious as to when this would not be the case is directed toward the sections on nonadiabatic dynamics in the Meyer-Miller-Stock-Thoss representation, such as section 1.3. In classical mechanics, momentum-dependent friction provides another example of a Hamiltonian with nonseparable position and momentum terms.

```

if (Real(rad) < 0.0) && (Imag(rad)*Imag(olddrad) < 0.0) {
    maslov = -maslov
}
result = maslov * sqrt(rad)

```

This involves a lot of comparisons, which tend to be slow operations. It also involves a full floating point multiplication when only the sign is useful. I have developed a faster method based on bitwise operations and the IEEE standard representation for floating point numbers. Assuming a mask (called `mask`) where the sign bit is one and all other bits are zero, that `rad` and `olddrad` are the current and previous radicands, and that `maslov` is the previous Maslov multiplier, then the following pseudocode implements the Maslov tracking:<sup>15</sup>

```

r1 = XOR(Imag(rad), Imag(olddrad))
r2 = AND(Real(rad, r1))
ifclause = AND(mask, r2)
maslov = XOR(maslov, ifclause)
result = XOR(maslov, sqrt(rad))

```

### Selection of Initial Conditions

The selection of initial conditions is a non-trivial matter for systems with many degrees of freedom. A grid method would grow exponentially with system size, and is therefore to be avoided.

Generally, we would like to perform the phase space integral using Monte Carlo methods. In order to do this, we need to split the integral into a distribution and a quantity to be averaged. Our weight function needs to be real-valued and non-negative for all inputs. If it is not normalized, we'll have to calculate the normalization constant for the distribution.

One advantage of the HK-IVR is that it can easily provide a sampling function for both the position and momentum coordinates. The position VV-IVR, on the other hand, does not have a natural sampling function for momentum.

In order to perform the Monte Carlo sampling, we have historically tried to sample using as much of the time-independent ( $t = 0$ ) information as possible. This means that a single weight is associated with each trajectory, and that the Monte Carlo can be completely decoupled from the trajectory calculations. This has the important advantage that after the Monte Carlo, the average over trajectories is an embarrassingly parallel problem.

For the HK-IVR, we simply multiply the time-independent overlap by its complex conjugate to get the weight function, and divide the remaining expression by the same for the quantity we will average. That, is we make the transformation:

$$\langle \psi_f | e^{-i\hat{H}t/\hbar} | \psi_i \rangle = \int dq_0 \int dp_0 \mathcal{C}_t e^{iS_t/\hbar} \langle \psi_f | q_t p_t \rangle \langle q_0 p_0 | \psi_i \rangle \quad (1.86)$$

$$= \int dq_0 \int dp_0 \mathcal{C}_t e^{iS_t/\hbar} \frac{\langle \psi_f | q_t p_t \rangle}{\langle \psi_i | q_0 p_0 \rangle} |\langle q_0 p_0 | \psi_i \rangle|^2 \quad (1.87)$$

where the function  $w(q_0, p_0) = |\langle q_0 p_0 | \psi_i \rangle|^2$  satisfies our need for a weight function (including normalization). The remainder of the integrand is the function we're averaging.

For other correlation function IVR methods, described below, we typically try to find simple sampling functions based on one of the operators, and apply a procedure similar to the one described above to ensure that we're solving a mathematically equivalent problem.

One would like for a Monte Carlo method to use as few trajectories as possible. Efforts to change our sampling function in order to reduce the number of trajectories required are described in chapter 2.

## 1.2 Semiclassical Correlation Functions

In practice, we generally prefer to apply semiclassical methods to the study of time correlation functions rather than just using the semiclassical propagator directly. There are several reasons for this.

From a theoretical standpoint, a very wide range of the experimental properties can be expressed in terms of time correlation functions, from exact expressions for reaction rates<sup>16</sup> to quantities related to correlation functions through linear response theory.

A more practical consideration is that the sign problem we encounter from the rapidly oscillating phase factor in the SC-IVR expressions can be partially cancelled out in a correlation function. A quantum correlation function is written as

$$C_{AB}(t) = \text{tr}(\hat{A}e^{i\hat{H}t/\hbar}\hat{B}e^{-i\hat{H}t/\hbar}) \quad (1.88)$$

where one of the operators is usually the “Boltzmann-ized” form: *i.e.*, it includes the density matrix. The premise used to develop semiclassical treatments of the entire correlation function is that the forward and backward propagators associated with the Heisenberg-evolved operator  $\hat{B}(t)$  may show some cancellation. Clearly, if  $\hat{B}$  were  $\hat{1}$ , the cancellation would be exact.

This idea allows us to develop methods specific to the calculation of time correlation functions, several of which are described below.

### 1.2.1 Double Herman-Kluk

The most obvious way to apply the HK-IVR to the problem of correlation functions is the brute force approach of inserting a full HK-IVR propagator for both the forward and backward propagation. We call this the double Herman-Kluk (DHK) IVR. Although we can do this, in its naïve implementation it can be difficult to converge. In addition to requiring integration of the double phase space (squaring the volume of phase space), the highly oscillatory nature of the integrand makes it difficult to converge numerically.

Since the “backward” time-evolution operator is just the Hermitian adjoint of the standard time-evolution operator, we can implement it by taking the Hermitian adjoint of the semi-

classical approximation. That is,

$$C_{AB}(t) = \text{tr} \left( \hat{A} \left( \int dq'_0 \int dp'_0 \mathcal{C}_{t'} e^{iS_{t'}} |q'_t p'_t\rangle \langle q'_0 p'_0| \right)^\dagger \hat{B} \left( \int dq_0 \int dp_0 \mathcal{C}_t e^{iS_t} |q_t p_t\rangle \langle q_0 p_0| \right) \right) \quad (1.89)$$

$$= \text{tr} \left( \hat{A} \int dq'_0 \int dp'_0 \mathcal{C}_{t'}^* e^{-iS_{t'}} |q'_0 p'_0\rangle \langle q'_t p'_t| \hat{B} \int dq_0 \int dp_0 \mathcal{C}_t e^{iS_t} |q_t p_t\rangle \langle q_0 p_0| \right) \quad (1.90)$$

where  $t'$  indicates the time associated with the backward trajectory. Allowing the integrals to move outside the trace, and invoking the cyclic property of the trace, this becomes:

$$C_{AB}(t) = \int dq_0 \int dp_0 \int dq'_0 \int dp'_0 e^{i(S_t - S_{t'})} \mathcal{C}_t \mathcal{C}_{t'}^* \langle q_0 p_0 | \hat{A} | q'_0 p'_0 \rangle \langle q'_t p'_t | \hat{B} | q_t p_t \rangle \quad (1.91)$$

This can be calculated by choosing some variant of  $\langle q_0 p_0 | \hat{A} | q'_0 p'_0 \rangle$  which is appropriate for Monte Carlo sampling (*e.g.*,  $|\langle q_0 p_0 | \hat{A} | q'_0 p'_0 \rangle|^2$ , or some other positive semidefinite function which can be normalized.)

### 1.2.2 Linearized SC-IVR

One of the advantages hoped for in studying correlation functions (in addition to their flexibility in describing chemical phenomena) is that the forward and backward propagation might cancel each other out to reduce some of the oscillatory nature of the integrand, which is the source of the requirement for many trajectories in SC-IVR methods.

The most brutal approximation to take advantage of this is to assume that the forward and backward trajectories are infinitesimally close to each other. Mathematically, we start by writing out a double van Vleck expression (where we have used Liouville's theorem to write the backward propagator in terms of forward trajectories):

$$C_{AB}(t) = \int dq_0 \int dp_0 \int dq'_0 \int dp'_0 e^{\frac{i}{\hbar}(S_t(q_0, p_0) - S_t(q'_0, p'_0))} |M_{qp}|^{1/2} |M'_{qp}|^{1/2} \times \text{tr} \left( \hat{A} |q'_0\rangle \langle q'_t | \hat{B} |q_t\rangle \langle q_0| \right) \quad (1.92)$$

$$= \int dq_0 \int dp_0 \int dq'_0 \int dp'_0 e^{\frac{i}{\hbar}(S_t(q_0, p_0) - S_t(q'_0, p'_0))} |M_{qp}|^{1/2} |M'_{qp}|^{1/2} \times \langle q_0 | \hat{A} | q'_0 \rangle \langle q'_t | \hat{B} | q_t \rangle \quad (1.93)$$

The second equality is due to the cyclic property of the trace.

Now we change variables, and instead of having variables describing the forward and backward trajectories, the new variables will describe the average and difference of the trajectories. For the position variables, these new coordinates are defined as

$$\bar{q}_0 = \frac{q_0 + q'_0}{2} \quad (1.94)$$

$$\Delta q = q_0 - q'_0 \quad (1.95)$$

The new momentum variables are similarly defined, and the Jacobian determinant of this transformation is 1.

Up to this point, we are (semiclassically) exact. But now we will introduce a rather harsh approximation by assuming that the forward and backward trajectories are infinitesimally close to each other. Expressed mathematically, we will describe all the time dependent quantities from the original variables in terms of first-order Taylor expansions in  $\Delta q$ . Replacing the dependence on  $q_0$  and  $p_0$  with  $\bar{q}_0 + \frac{\Delta q}{2}$ , one obtains the first-order Taylor approximation:

$$q_t\left(\bar{q}_0 + \frac{\Delta q}{2}, \bar{p}_0 + \frac{\Delta p}{2}\right) \approx q_t(\bar{q}_0, \bar{p}_0) + \frac{\partial \bar{q}_t}{\partial \bar{q}_0} \cdot \frac{\Delta q}{2} + \frac{\partial \bar{q}_t}{\partial \bar{p}_0} \cdot \frac{\Delta p}{2} \quad (1.96)$$

$$S_t\left(\bar{q}_0 + \frac{\Delta q}{2}, \bar{p}_0 + \frac{\Delta p}{2}\right) \approx S_t(\bar{q}_0, \bar{p}_0) + \frac{\partial S_t}{\partial \bar{q}_0} \cdot \frac{\Delta q}{2} + \frac{\partial S_t}{\partial \bar{p}_0} \cdot \frac{\Delta p}{2} \quad (1.97)$$

The derivatives of the action can be written in a more useful form using Hamilton's equations of motion and integration by parts. For the derivative  $\frac{\partial S_t}{\partial \bar{q}_0}$ , we have:

$$\frac{\partial S_t}{\partial \bar{q}_0} = \frac{\partial}{\partial \bar{q}_0} \int_0^t dt' \frac{\dot{\bar{p}}_{t'}^2}{2m} - V(\bar{q}_{t'}) \quad (1.98)$$

$$= \int_0^t dt' \bar{p}_{t'} \frac{\partial \bar{p}_{t'}/m}{\partial \bar{q}_0} - \frac{\partial V(\bar{q}_{t'})}{\partial \bar{q}_{t'}} \frac{\partial \bar{q}_{t'}}{\partial \bar{q}_0} \quad (1.99)$$

$$= \int_0^t dt' \bar{p}_{t'} \left( \frac{\partial}{\partial t'} \frac{\partial \bar{q}_{t'}}{\partial \bar{q}_0} \right) + \int_0^t dt' \left( \frac{\partial \bar{p}_{t'}}{\partial t'} \right) \frac{\partial \bar{q}_{t'}}{\partial \bar{q}_0} \quad (1.100)$$

$$= \bar{p}_{t'} \frac{\partial \bar{q}_{t'}}{\partial \bar{q}_0} \Big|_0^t - \int_0^t dt' \left( \frac{\partial \bar{p}_{t'}}{\partial t'} \right) \frac{\partial \bar{q}_{t'}}{\partial \bar{q}_0} + \int_0^t dt' \left( \frac{\partial \bar{p}_{t'}}{\partial t'} \right) \frac{\partial \bar{q}_{t'}}{\partial \bar{q}_0} \quad (1.101)$$

$$= \bar{p}_t \frac{\partial \bar{q}_t}{\partial \bar{q}_0} - \bar{p}_0 \frac{\partial \bar{q}_0}{\partial \bar{q}_0} = \bar{p}_t \bar{M}_{qq} - \bar{p}_0 \quad (1.102)$$

(where, for simplicity, we have treated this as a one-dimensional problem.) An analogous calculation can be made for  $\frac{\partial S_t}{\partial \bar{p}_0}$ . Substituting these into the expansion of the action given in equation (1.97), we get:

$$S_t\left(\bar{q}_0 + \frac{\Delta q}{2}, \bar{p}_0 + \frac{\Delta p}{2}\right) \approx S_t(\bar{q}_0, \bar{p}_0) + \frac{1}{2} \left( \left( \bar{p}_t^T \frac{\partial \bar{q}_t}{\partial \bar{q}_0} - \bar{p}_0^T \right) \Delta q + \bar{p}_t^T \frac{\partial \bar{q}_t}{\partial \bar{p}_0} \Delta p \right) \quad (1.103)$$

A similar calculation can be done for the quantities depending on  $q'_0$  and  $p'_0$ , where the signs in front of the displacements  $\Delta q$  and  $\Delta p$  are negative.

Looking at the result for the action, we see that the difference in the forward and backward actions is

$$S_t(q_0, p_0) - S_t(q'_0, p'_0) \approx \bar{p}_t^T \left( \frac{\partial \bar{q}_t}{\partial \bar{q}_0} \Delta q + \frac{\partial \bar{q}_t}{\partial \bar{p}_0} \Delta p \right) - \bar{p}_0^T \Delta q \quad (1.104)$$

$$= \bar{p}_t^T (\bar{M}_{qq} \Delta q + \bar{M}_{qp} \Delta p) - \bar{p}_0^T \Delta q \quad (1.105)$$

As an aside, we note that we get the same result by expanding the difference in action to second order instead of first, since the difference in action is an odd function of the difference variables.

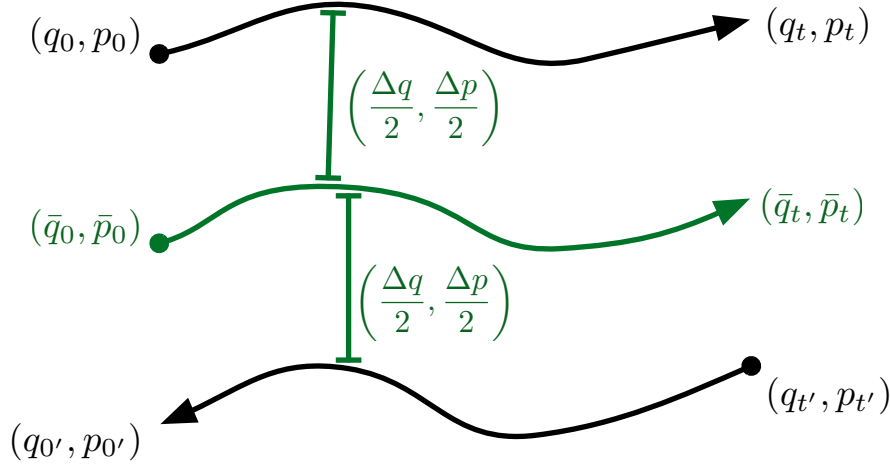


Figure 1.2: Cartoon of the linearized semiclassical initial value representation (LSC-IVR) method for calculating correlation functions. The original forward and backward trajectories (black) are written in sum (average,  $(\bar{q}, \bar{p})$ ) and difference ( $\Delta q, \Delta p$ ) variables (red). The linearization approximation is that the difference variables  $\Delta q$  and  $\Delta p$  remain very small.

Since the monodromy matrices are independent of  $\Delta q$  and  $\Delta p$  (to first order), we have  $M_{pq} = M'_{pq} = \bar{M}_{pq}$  and  $M_{qq} = M'_{qq} = \bar{M}_{qq}$ . Now we make the change of variables from  $\Delta p$  to  $\Delta q' = -(\bar{M}_{qq}\Delta q + \bar{M}_{qp}\Delta p)$ , which has the Jacobian  $J' = |\bar{M}_{qp}|$ . Inserting all of this into equation (1.93) we obtain:

$$\begin{aligned} C_{AB}(t) &\approx \int d\bar{q}_0 \int d\bar{p}_0 \int d\Delta q \int d\Delta q' \frac{1}{|\bar{M}_{qp}|} |\bar{M}_{qp}|^{1/2} |\bar{M}_{qp}|^{1/2} e^{\frac{i}{\hbar} (\bar{p}_a^\top t \Delta q' - \bar{p}_0^\top \Delta q_0)} \\ &\quad \times \left\langle \bar{q}_0 + \frac{\Delta q}{2} \middle| \hat{A} \middle| \bar{q}_0 - \frac{\Delta q}{2} \right\rangle \left\langle \bar{q}_t - \frac{\Delta q'}{2} \middle| \hat{B} \middle| \bar{q}_t + \frac{\Delta q'}{2} \right\rangle \end{aligned} \quad (1.106)$$

$$\begin{aligned} &\approx \int d\bar{q}_0 \int d\bar{p}_0 \left( \int d\Delta q e^{\frac{i}{\hbar} \bar{p}_0 \cdot \Delta q} \left\langle \bar{q}_0 + \frac{\Delta q}{2} \middle| \hat{A} \middle| \bar{q}_0 - \frac{\Delta q}{2} \right\rangle \right) \\ &\quad \times \left( \int d\Delta q' e^{\frac{i}{\hbar} \bar{p}_t \cdot \Delta q'} \left\langle \bar{q}_t + \frac{\Delta q'}{2} \middle| \hat{B} \middle| \bar{q}_t - \frac{\Delta q'}{2} \right\rangle \right) \end{aligned} \quad (1.107)$$

$$\approx \int d\bar{q}_0 \int d\bar{p}_0 A_W(\bar{q}_0, \bar{p}_0) B_W(\bar{q}_t, \bar{p}_t) \quad (1.108)$$

where we have used the Hermiticity of  $\hat{B}$  and where  $X_W(q, p)$  is the Wigner function of an operator  $\hat{X}$ , defined by

$$X_W \equiv \int d\Delta q e^{\frac{i}{\hbar} p \cdot \Delta q} \left\langle q + \frac{\Delta q}{2} \middle| X \middle| q - \frac{\Delta q}{2} \right\rangle \quad (1.109)$$

Equation (1.108) gives us the linearized semiclassical initial value representation (LSC-IVR).<sup>17–20</sup> The idea behind this derivation is illustrated in figure 1.2. The forward trajectory,

$(q_0, p_0) \rightarrow (q_t, p_t)$ , and the backward trajectory,  $(q_{t'}, p_{t'}) \rightarrow (q_{0'}, p_{0'})$ , are replaced by their average (forward) trajectory,  $(\bar{q}_0, \bar{p}_0) \rightarrow (\bar{q}_t, \bar{p}_t)$ , and the difference between the trajectories  $(\Delta q, \Delta p)$ . The linearization approximation assumes that this last is very small, and that the forward, backward, and average trajectories are all about the same.

The LSC-IVR is also known as the “classical Wigner” model. As such, it was already in use before its derivation in the context of semiclassical IVRs. However, that derivation reignited interest in the linearized IVR/classical Wigner method, and it is one of the more widely used IVR-based methods. It has many advantages: mainly, it has much in common with classical methods of calculating correlation functions. As written above, the only differences are that the initial conditions are sampled from a the Wigner distribution of an observable instead of the classical distribution, and that the time-evolved operator is also a Wigner function instead of a classical function. Although the LSC-IVR is a rough approximation, Liu and Miller recently showed that it can be seen as the first terms in a series of dynamical terms which lead to exact quantum mechanics.<sup>21</sup>

Practically speaking, there are other important differences that make the LSC-IVR harder to implement (or at least converge) than classical methods. The first is that not all Wigner distributions can be calculated analytically. Much work has gone into this problem, particularly in the context of the Boltzmann operator.<sup>22–24</sup> Another problem is that the LSC-IVR correlation function doesn’t allow the time-translation symmetry that is exploited by various classical algorithms to improve the convergence of classical time correlation functions, such as the Fourier transform method described in section 6.3.2 of reference 25. This lack of time-translation symmetry is because the classical mechanics do not preserve the quantum distributions.

It is also worth reiterating that the LSC-IVR approximation is a rather harsh one. In particular, by only selecting trajectories which are infinitesimally close to one another, it removes the possibility of “true” quantum coherence effects. A quick glance at the equation for the LSC-IVR correlation function shows that it doesn’t contain the complex exponential of the action, which is the source of interference between paths in the path integral (and single-propagator IVR) formulae. The inability of the LSC-IVR to capture quantum interference effects causes it to fail for many interesting problems. Considering figure 1.2 and imagining the two-slit experiment, we can again see that we wouldn’t expect to capture dynamical quantum interferences. It is impossible for two paths close enough for the linearization approximation to pass through different slits. That simple gedankenexperiment for the two-slit problem has been verified by computational studies.<sup>26</sup> While the LSC-IVR can capture electronic surface populations<sup>20</sup> (with the assistance of the MMST Hamiltonian, to be presented in section 1.3), it is unable to resolve two separate nuclear momenta in nonadiabatic dynamics.<sup>27</sup> It also fails to capture interference in the radial distribution function<sup>28</sup> or recurrences due to quantum recoherence in calculations of the survival amplitude.<sup>29</sup>

With all of these weaknesses enumerated, one might wonder why it has become such a popular tool. The answer is that it is one of the few methods that are feasible for large systems, and that in large systems we generally don’t expect quantum coherences in the nuclear dynamics to play a major role. It has been used to good effect in the calculation of diffusion constants in liquid *para*-hydrogen<sup>30</sup> and in water.<sup>31</sup> While it cannot capture nuclear quantum coherences, methods like the Meyer-Miller-Stock-Thoss treatment of multiple electronic states (see section 1.3) can add

electronic coherent dynamics to the classical equations of motion, which then get carried into the LSC-IVR. This technique has been used to treat the spin-boson problem with different spectral densities<sup>20,32</sup> and has even been applied to the problem of energy transfer in a photosynthetic protein.<sup>33</sup> In these cases, the “nuclear” motion is simply a discretization of the spectral density as coupled harmonic oscillators; asking about coherences in the nuclear dynamics is physically meaningless. Therefore, the linearized IVR is a perfectly good choice of method for that kind of problem!

### 1.2.3 Forward-Backward IVR

The basic idea of the forward-backward (FB) IVR<sup>34</sup> begins by writing the  $\hat{B}$  operator in some unitary form. Usually, we accomplish this only for operators which are functions of only position or functions of only momenta, but for the purposes of this derivation, we will consider the general case in which  $\hat{B}$  can be written as  $e^{-i\phi(p,q)}$ .

The trick here is that now we can see the  $e^{-i\phi(p,q)}$  term as a kind of single-time Hamiltonian. In fact, we can see the whole sequence of unitary operators,  $e^{i\hat{H}t}e^{-i\phi(p,q)}e^{-i\hat{H}t}$  as the time-evolution operator for a time dependent Hamiltonian:

$$\hat{H}(t) = \begin{cases} H(t) & 0 \rightarrow t' \\ \phi(p, q) & t = t' \\ H(t) & t' \rightarrow 0 \end{cases} \quad (1.110)$$

That is to say, the Hamiltonian behaves normally up until time  $t'$  (forward dynamics). At time  $t'$ , it makes an instantaneous jump (which depends on the operator  $\hat{B}$ ), and then propagates backward in time (with the negative Hamiltonian) for the same amount of time as the forward propagation.

This idea is intuitive if one looks at the full quantum time correlation function, as written in equation (1.88). In the Schrödinger picture, we see that a state at the right side of the trace propagates forward to time  $t'$ , is acted on by operator  $\hat{B}$ , and is propagated backward in time by  $t'$ , where it is acted on by operator  $\hat{A}$ . In our semiclassical picture, the action of operator  $\hat{B}$  at time  $t'$  is an instantaneous jump in phase space.

We'll refer to the function  $\phi(q, p)$  as the “jump Hamiltonian,” since it clearly plays to role of an instantaneous Hamiltonian by analogy to the time evolution operator. Since it only applies at time  $t$ , it can be added to either the forward or the backward propagation, multiplied by the Dirac delta  $\delta(t - t')$ . Since the jump “time”-evolution operator  $\exp(-i\phi(p, q))$  does not involve  $t$  (unlike the normal time-evoution operator  $\exp(-i\hat{H}t)$ ) the jump is truly instantaneous, and is not multiplied by the time differential  $dt$  when integrated.

This is an approximation beyond the DHK-IVR. The “full semiclassical” forward-backward idea would involve inserting a resolution of the identity on either side of the jump Hamiltonian. The additional approximation made in the FB-IVR is effectively to make the stationary phase approximation between each of the propagators and time evolved operator  $\hat{B}$ .

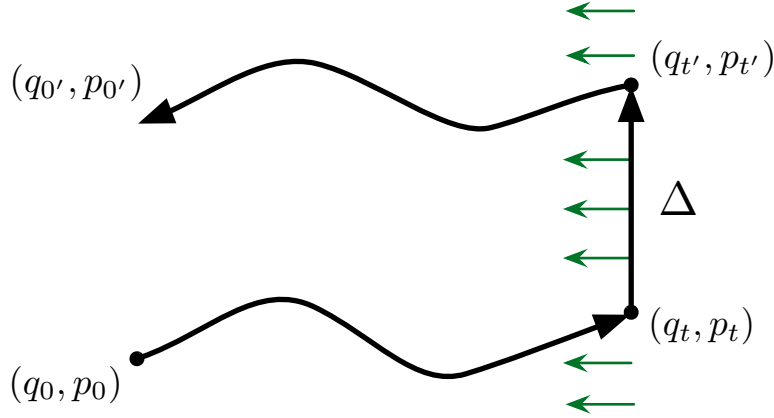


Figure 1.3: Cartoon of the forward-backward IVR (FB-IVR) method for calculating correlation functions. For each forward trajectory  $(q_0, p_0) \rightarrow (q_t, p_t)$ , a number of jumps  $\Delta$  are made, and a backward trajectory is run from each jump from  $(q_{t'}, p_{t'})$  to  $(q_0', p_0')$ . One such backward trajectory is shown in full; the starts of others are shown as the green arrows.

By analogy with Hamilton's equations of motion, we find:

$$\Delta p = -\frac{d\phi(p, q)}{dq} \quad (1.111)$$

$$\Delta q = \frac{d\phi(p, q)}{dp} \quad (1.112)$$

The change in the action is just the Lagrangian at time  $t'$ , which we calculate as the Legendre transform of the jump Hamiltonian  $\phi(p, q)$ .

$$\Delta S = p \frac{d\phi(p, q)}{p} - \phi(p, q) \quad (1.113)$$

Finally, the jump in the monodromy matrix is calculated in analogy to equation (1.84) from section 1.1.3 above.

$$\Delta \mathbf{M} = \begin{pmatrix} \phi_{pq} & \phi_{pp} \\ -\phi_{qq} & -\phi_{pq} \end{pmatrix} \mathbf{M} \quad (1.114)$$

where the subscripts refer to taking derivatives with respect to those variables.

The forward-backward idea is illustrated in figure 1.3. For a given set of initial conditions  $(q_0, p_0)$ , the trajectory is propagated forward in time to  $(q_t, p_t)$ . At this point, jump Hamiltonian causes an instantaneous jump in phase space to  $(q_{t'}, p_{t'})$  (although we note that in most practical examples, only one  $q_t$  or  $p_t$  is changed by the jump). Finally, the trajectory is propagated backward in time from  $(q_{t'}, p_{t'})$  to  $(q_0', p_0')$ . The entire process is treated as one dynamical trajectory for the purposes of integrating the action and monodromy matrices. For each forward trajectory, many backward trajectories must be calculated, as indicated by the small arrows starting along the jump path.

As an aside, two situations which we commonly use are when the jump Hamiltonian  $\phi(q, p)$  is a linear function of only  $p$  or only  $q$ . In either case, it's easy to see that  $\Delta\mathbf{M}$  is null. In the case that the  $\phi(p, q)$  is a linear function of only  $p$ , we can also see that the jump in action is zero.

This leaves us with the question of how one can represent a given operator in that unitary form. One approach is to use the identity

$$\hat{B} = \lim_{\lambda \rightarrow 0} i \frac{d}{d\lambda} e^{-i\lambda\hat{B}} \quad (1.115)$$

However, when this derivative identity is applied, it fails to capture quantum interference effects.<sup>35</sup> This is because, when  $\lambda = 0$ , we recover a situation where the forward and backward trajectories are equivalent (allowing no interference), as in the LSC-IVR. This derivative-based FB-IVR thus gets results which are similar to those achieved by the LSC-IVR. In order to capture interference effects, the method we typically use is to take the Fourier transform of the operator in question.

For a general operator, this would require doing the Fourier transform for every degree of freedom that contributes to the functional form of operator  $\hat{B}$ . In order to make the calculation feasible, we instead do the one dimensional Fourier transform of some collective function. To make the jump calculation feasible, we also require that this collective function be of either the momenta or the positions, but not both. A typical example is for rate calculations: the rate can be calculated from the long-time limit of the flux-side time correlation function. In this case, the  $\hat{B}$  operator is the “side” function: a Heaviside function of the dividing surface. This function gives 1 if the system is in the product state, 0 otherwise.

In a case like this, we have  $\hat{B} = B(s(\hat{q}))$ . (In the specific case of the side function,  $s(q)$  defines the dividing surface, and  $B(s)$  is the Heaviside function.) To obtain a correlation function with the second operator written in terms of the jump time-evolution operator  $\exp(-i\phi(p, q))$ , we write  $B(s)$  in terms of its Fourier transform,  $\tilde{B}(p_s)$ :

$$B(s(\hat{q})) = \int dp_s \tilde{B}(p_s) e^{ip_s s(\hat{q})} \quad (1.116)$$

When we insert this into the quantum time correlation function, we obtain

$$\text{tr} \left( \hat{A} e^{i\hat{H}t} \hat{B} e^{-i\hat{H}t} \right) = \text{tr} \left( \hat{A} e^{i\hat{H}t} \int dp_s \tilde{B}(p_s) e^{ip_s s(\hat{q})} e^{-i\hat{H}t} \right) \quad (1.117)$$

$$= \int dp_s \tilde{B}(p_s) \text{tr} \left( \hat{A} e^{i\hat{H}t} e^{ip_s s(\hat{q})} e^{-i\hat{H}t} \right) \quad (1.118)$$

Now we see that we have  $\phi(p, q) = -p_s s(q)$ . At time  $t$ , we make a jump in momentum according to equation (1.111)

$$\Delta p = p_s \nabla s(q) \quad (1.119)$$

If we have some idea of the scale associated with the features of the function we hope to see, then we can use that information to estimate the range and step size of the jump parameter in the Fourier transform method. This is due to fundamental interactions between a discretized function and its Fourier transform: the resolution in one representation is determined by the range

in the other representation. Consider conjugate variables  $\rho$  and  $\chi$ . Assume we want a result which is a function of  $\chi$  — this means that our jump in the FB-IVR is in  $\rho$ . The resolution  $\Delta\chi$  and the range  $\chi_{\max}$  are given in terms of their counterparts in the  $\rho$  representation:

$$\Delta\chi = \frac{2\pi}{\rho_{\max} - \rho_{\min}} \quad (1.120)$$

$$\chi_{\max} = \frac{\pi}{\Delta\rho} \quad (1.121)$$

An FFT routine will give  $\chi_{\min} = -\chi_{\max}$ .

The FB-IVR retains the phase dependence on the action, which allows it to capture the interferences of true quantum dynamical effects, which, as discussed previously, the LSC-IVR is unable to do. However, this comes with a couple of significant costs. First, any FB-IVR calculation can be very expensive. Since we need to do the Fourier integral over the jump parameter, each forward trajectory corresponds to some number (on the order of thousands) of backward trajectories. The trick of taking the Fourier transform of some collective function, as described above, prevents this from being a much uglier situation. However, it is still extremely expensive.

The other problem with the FB-IVR is that it requires a completely separate calculation at each time. The jump must be made at a specific time, and all the backward trajectories must start from there. This means that the FB-IVR is not a very efficient way to calculate a time-correlation function (at least, not with sufficient resolution to calculate the integral of that time-correlation function and use a Green-Kubo relation to determine some property). Fortunately, many quantities are either of interest as a specific time (such as the radial distribution function<sup>28</sup>) or are interesting in the long-time limit (such as the rate as the long-time limit of the flux-side correlation function<sup>36</sup> or various distributions after some scattering process<sup>27</sup>).

#### 1.2.4 Other SC-IVR Methods for Correlation Functions

There exist several other methods to calculate correlation functions which are based on the SC-IVR. These include the double-backward IVR,<sup>36</sup> the exact forward-backward IVR,<sup>37</sup> and the generalized forward-backward IVR.<sup>29</sup> Since they do not pertain to the rest of this thesis, they will not be discussed here.

### 1.3 The Meyer-Miller-Stock-Thoss Hamiltonian

Although not strictly confined to the SC-IVR, I will take this opportunity to introduce the Meyer-Miller (or Meyer-Miller-Stock-Thoss, MMST) “classical electron” Hamiltonian for nonadiabatic systems. A notable subset of my work has involved developing methodologies for nonadiabatic systems based on the MMST Hamiltonian and applications of the MMST Hamiltonian to specific systems of interest.

#### 1.3.1 Derivation

The original development of this Hamiltonian was done by Meyer and Miller in 1979.<sup>38</sup> They started by considering the amplitudes of the quantum electronic basis vectors, and con-

necing that to the action part of a pair of action-angle classical variables. They found that the classical equations of motion for these action-angle variables matched the quantum equations of motion for the amplitudes. One important point in their derivation was that they found it necessary to make the “Langer modification,”<sup>39</sup> shifting all action variables  $n$  to  $n + \frac{1}{2}$ . They had to correct their energy levels for this change by subtracting  $\frac{1}{2}$  from the diagonal matrix elements — in the more rigorous derivation that follows, we will see that this correction factor comes about due to the canonical commutation relations for bosons.

A more concise (and exact) introduction of the same Hamiltonian was developed by Stock and Thoss.<sup>40</sup> Their derivation, based on Schwinger’s ladder operator theory of angular momentum, will be sketched out here.

For a system with  $N$  discrete (typically electronic) states, we write the Hamiltonian as:

$$H = \sum_{i,j} |\Phi_i\rangle H_{ij}(Q, P) \langle\Phi_j| \quad (1.122)$$

where  $Q$  and  $P$  are the nuclear coordinates and momenta, respectively.

One can directly map the operators  $|\Phi_n\rangle \langle\Phi_m|$  to creation and annihilation operators: the bra annihilates excitation in the  $m$ th basis state, and the ket creates the excitation in the  $n$ th basis state. So we start by replacing the transfer operators  $|\Phi_i\rangle \langle\Phi_j|$  from equation (1.122) with their (bosonic) ladder operator representations:

$$H = \sum_{i,j} a_i^\dagger a_j H_{ij}(Q, P) \quad (1.123)$$

$$= T(P) + V_0(Q) + \sum_{i,j} a_i^\dagger a_j V_{ij}(Q) \quad (1.124)$$

In the second step, we have assumed that each element of the Hamiltonian matrix can be written  $H_{ij}(Q, P) = T(P) + V_0(Q) + V_{ij}(Q)$ .

We recall the isomorphism between the harmonic oscillator and the ladder operators,

$$a_n^\dagger = \frac{1}{\sqrt{2}} (\hat{x}_n - i\hat{p}_n) \quad (1.125)$$

$$a_n = \frac{1}{\sqrt{2}} (\hat{x}_n + i\hat{p}_n) \quad (1.126)$$

where we have assumed unit values for the mass and harmonic frequency.

Now we insert these relations into our Hamiltonian.

$$H = T(P) + V_0(Q) + \frac{1}{2} \sum_{i,j} (\hat{x}_i - i\hat{p}_i)(\hat{x}_j + i\hat{p}_j) V_{ij}(Q) \quad (1.127)$$

$$= T(P) + V_0(Q) + \frac{1}{2} \sum_{i,j} (\hat{x}_i \hat{x}_j + \hat{p}_i \hat{p}_j + i\hat{x}_i \hat{p}_j - i\hat{p}_i \hat{x}_j) V_{ij}(Q) \quad (1.128)$$

Now we observe that the sum goes over all states for both  $i$  and  $j$  — that is, there are  $N^2$  terms. That means that for every ordered pair  $(i, j)$  with  $i \neq j$  from that set of  $N^2$  terms, there will also

be an ordered pair  $(i', j') = (j, i)$ . Splitting off the diagonal terms and combining the ordered pairs of  $(i, j)$  and  $(j, i)$ , we get (assuming that  $V_{ij}(Q)$  is Hermitian):

$$\begin{aligned} H &= T(P) + V_0(Q) + \frac{1}{2} \left( \sum_i (\hat{x}_i^2 + \hat{p}_i^2 + i\hat{x}_i\hat{p}_i - i\hat{p}_i\hat{x}_i) V_{ii}(Q) \right. \\ &\quad \left. + \sum_{i < j} (\hat{x}_i\hat{x}_j + \hat{x}_j\hat{x}_i + \hat{p}_i\hat{p}_j + \hat{p}_j\hat{p}_i + i\hat{x}_i\hat{p}_j - i\hat{p}_j\hat{x}_i - i\hat{p}_i\hat{x}_j + i\hat{x}_j\hat{p}_i) V_{ij}(Q) \right) \end{aligned} \quad (1.129)$$

$$\begin{aligned} &= T(P) + V_0(Q) + \frac{1}{2} \left( \sum_i (\hat{x}_i^2 + \hat{p}_i^2 + i[\hat{x}_i, \hat{p}_i]) V_{ii}(Q) \right. \\ &\quad \left. + \sum_{i < j} (\{\hat{x}_i, \hat{x}_j\} + \{\hat{p}_i, \hat{p}_j\} + i[\hat{x}_i, \hat{p}_j] + i[\hat{x}_j, \hat{p}_i]) V_{ij}(Q) \right) \end{aligned} \quad (1.130)$$

where the braces represent the anticommutator and the brackets represent the commutator. Recalling the canonical commutation relations:

$$[\hat{x}_n, \hat{p}_m] = i\delta_{nm} \quad (1.131)$$

Now we obtain one of the forms of the MMST Hamiltonian:

$$H = T(P) + V_0(Q) + \frac{1}{2} \sum_i (\hat{x}_i^2 + \hat{p}_i^2 - 1) V_{ii}(Q) + \sum_{i < j} (\hat{x}_i\hat{x}_j + \hat{p}_i\hat{p}_j) V_{ij}(Q) \quad (1.132)$$

I usually prefer to express it in the equivalent form:

$$H = T(P) + V_0(Q) + \frac{1}{2} \sum_{i,j} (\hat{x}_i\hat{x}_j + \hat{p}_i\hat{p}_j - \delta_{ij}) V_{ij}(Q) \quad (1.133)$$

Now the electronic degrees of freedom have been included in a form which is suitable for semiclassical treatment. The positions and momenta that came from the electronic degrees of freedom are treated as classical positions and momenta.

This mapping is only exact in the subspace of a single excitation, but that restriction still leaves many problems of great interest.

### 1.3.2 Using the MMST in the SC-IVR

To combine MMST methods with SC-IVR methods, we must also consider the description of an initial wavepacket in terms of these classical electronic degrees of freedom. These calculations are performed with one mode that initially has a single quantum of excitation: we'll call a state with the excitation in the  $i$ th mode  $|\Phi_i\rangle$ . The standard method<sup>41</sup> has been to select the initial electronic wavepacket using a direct product of harmonic oscillator states. For simplicity, we'll define the  $\phi_n(x)$  as the  $n$ th excited harmonic oscillator state. To generate  $|\Phi_i\rangle$  (in the position representation) for mode  $i$  we use the harmonic oscillator first excited state  $\phi_1(x_i)$ ,

and for modes  $j \neq i$  we use the harmonic oscillator ground state  $\phi_0(x_j)$ . Thus, the full position representation is

$$\langle x | \Phi_i \rangle = \phi_1(x_i) \prod_{j \neq i} \phi_0(x_j) \quad (1.134)$$

It is relatively simple to show that this prescription selects the correct matrix elements of the Hamiltonian (1.133) if we integrate over the electronic variables (still treating the operators quantum mechanically).

For the HK-IVR and FB-IVR, we typically want to sample from something that resembles the overlap of the initial state with a coherent state. We write the multidimensional coherent state  $|\mathbf{p} \mathbf{q}\rangle$  as the direct product of one-dimensional coherent states  $|p_n q_n\rangle$ . As such, our initial (electronic) overlap is the product of terms of the form  $\langle \phi_k(x_n) | p_n x_n \rangle$ . We choose the width of the coherent state to be  $\gamma = 1$  for all electronic states (which simplifies the math). The resulting overlap for the unoccupied electronic degrees of freedom is:

$$\langle \phi_0 | p x \rangle = \exp \left( -\frac{1}{4} (x^2 + p^2) - \frac{i}{2} x p \right) \quad (1.135)$$

For the occupied degree(s) of freedom, we have

$$\langle \phi_1 | p x \rangle = \frac{1}{\sqrt{2}} (x - ip) \exp \left( -\frac{1}{4} (x^2 + p^2) - \frac{i}{2} x p \right) \quad (1.136)$$

When we apply the MMST method directly to the LSC-IVR (starting in a specific electronic state) we apply a similar procedure, but instead of looking at the overlaps, we take the Wigner transform of the electronic projection operator  $|\Phi_i\rangle \langle \Phi_i|$ . Again (assuming an initially uncorrelated state, as we typically do) this can be decomposed into the product of contributions from each mode. For the unoccupied modes  $j$ ,

$$(|\phi_0\rangle \langle \phi_0|)_W = 2 \exp(-x^2 - p^2) \quad (1.137)$$

For the occupied mode  $i$ ,

$$(|\phi_1\rangle \langle \phi_1|)_W = \sqrt{8} \left( x^2 + p^2 - \frac{1}{2} \right) \exp(-x^2 - p^2) \quad (1.138)$$

### 1.3.3 Numerical Challenges in MMST Dynamics

However, one can run into numerical problems with the MMST Hamiltonian. As I discovered when attempting to use SC-IVR methods to study the photodissociation of IBr, the MMST dynamics can be problematic. Under certain circumstances, the nuclear motion can go in the wrong direction (effectively on the inverted potential!).

To see why this is, we should return to the original Meyer-Miller formulation of the problem, where the Cartesian electronic coordinates  $(x_i, p_i)$  are derived from more fundamental action-angle variables  $(n_i, q_i)$ . In fact, the action variables  $n_i$  are directly related to quantum numbers (one can backtrack to a similar position from the Stock-Thoss derivation outlined above).

Since we do not restrict our initial electronic coordinates to have the correct quantum numbers, we can find sets of initial electronic coordinates such that:

$$x_i^2 + p_i^2 - \frac{1}{2} < 0 \quad \forall i \quad (1.139)$$

For simplicity, consider a two-state system. If we assume a system with  $V_0(Q)$  constant and  $V_{12}(Q)$  near zero in the region of initial conditions (as is common), then the effect of equation (1.139) is that instead of the effective nuclear potential looking like some (positive) linear combination of  $V_{11}$  and  $V_{22}$ , it looks like a linear combination of the inverted potentials  $-V_{11}$  and  $-V_{22}$ ! As a result, a system with steep walls will lead to trajectories that overflow, reporting not-a-number. Furthermore, the condition above is a weak requirement: it is sufficient to guarantee that this problem will occur, but it is not necessary. If only one state is problematic, that can be enough for the whole calculation to fail, depending on the specifics of the diabats.

How likely are we to have this problem? If we're sampling the wavefunction described in section 1.3.2 (using the magnitude of the functions listed in that section), then the probability of an unoccupied degree of freedom satisfying part of that condition (if we're sampling for an HK-IVR or FB-IVR) is 11.75%. Looking at the modulus in terms of  $r = \sqrt{x^2 + p^2}$ , we have the probability that  $r^2 < \frac{1}{2}$  as

$$\frac{\int_0^{2\pi} d\theta \int_0^{\sqrt{1/2}} dr r \exp(-\frac{1}{4}r^2)}{\int_0^{2\pi} d\theta \int_0^{\infty} dr r \exp(-\frac{1}{4}r^2)} \quad (1.140)$$

Similarly, the probability of an occupied state (if we sample from the modulus) satisfying that is 3.08%. For the LSC-IVR, the results are worse. In that case, 39.35% of trajectories give the inverted surface for the unoccupied state and 14.94% give the inverted surface for the occupied state.

Putting this together, for a system with two electronic states, one of which is initially occupied (a common situation to study), the probability of satisfying the criterion (1.139), *i.e.*, both states match, guaranteeing failure, is 0.36% for the HK-IVR and FB-IVR case, and 5.88% for the LSC-IVR. These numbers may seem small, but with tens of thousands of trajectories required in a typical IVR calculation, they are not insignificant. The probability that one state or the other will match that criterion (risking failure, but not guaranteeing it) is 14.47% for the HK-IVR and FB-IVR and 51.59% for the LSC-IVR. Of course, as we go to more electronic states, the probability of satisfying the strong condition (1.139) decreases, but the probability of satisfying the weaker condition where at least one degree of freedom risks causing trouble increases. If, as is the case for IBr, the unoccupied state has a much larger energy and slope than the occupied state, then the probability of failure is the probability of that state contributing to the criterion (1.139) (for the photodissociation of IBr, 11.75% for the FB-IVR and HK-IVR and 39.35% for the LSC-IVR).

Details of the sampling methodology (sampling by Gaussians of various widths, for example) can change the specific percentages cited above. However, nothing will change the fact that the distribution at  $t = 0$  has a large amplitude in the regions where each individual degree of freedom contribute to the criterion (1.139). In order to accurately sample the wavefunction,

one must sample those regions. And by sampling those regions, one causes the failure of the calculation.

A quick-and-dirty approach to this problem is to kill any trajectories which will cause this problem, either by imposing a check on the geometry (to ensure that the system isn't far into a repulsive wall) or by imposing a check on the energy. But even that idea is bound to fail: while it might work for a one-dimensional system that starts out on a repulsive wall (such as the IBr system that initiated my thoughts on this) within forward-propagator methods, it is likely to fail for calculations using the FB-IVR. This is because some of those trajectories which are killed in the forward direction may have made a significant contribution after backward propagation (in fact, the zero-jump backward trajectory is guaranteed to have a good overlap!) Along a similar line of thought, even in the LSC-IVR it seems fishy: at relatively short time (that is, long enough for the distribution to start evolving but not long enough for a significant number of trajectories to violate the constraint) a wavepacket with initially zero average momentum and which, classically, should be evolving to forward momentum, will show both positive and negative peaks in the momentum distribution. There's also the question of what killing these trajectories means for normalization.

A similar issue occurs when one looks at other kinds of physical problems. For example, consider an atom-diatom potential energy surface, with a conical intersection near the saddle point of the ground state. If, due to coupling near the saddle point, we end up on an inverted surface in the direction perpendicular to the reaction coordinate (*i.e.*, if our saddle point becomes a maximum) then we can fall off into the abyss. If we don't know the details of the potential energy surface's geometry near our transition state *a priori*, then we only know what we've fallen into the abyss after we've already fallen. In this case, fixes based on the initial conditions aren't sufficient.

To my knowledge, there does not yet exist a method which avoids these problems while directly combining this mapping approach with the specific semiclassical methods described in sections 1.1 and 1.2. Quasiclassical sampling might ameliorate the problems from starting at a highly-sloped part of the surface (at least for certain geometries of the crossing point), but they would still fail to fix the problem near the transition state in the atom-diatom reaction.

However, there is a method which is largely in line with the philosophy of the methodologies described above, but which doesn't suffer from these problems. The “linearized approach to nonadiabatic dynamics based on the mapping formalism” (LAND-map) of Bonella and Coker<sup>42,43</sup> and subsequent work such as the “iterative linearized approach to nonadiabatic dynamics” (ILND)<sup>44</sup> doesn't seem to suffer from these problems. These approaches represent more of a “half-linearized” approach (despite their names): in the LSC-IVR, we have linearized the entire trajectory. In LAND-map and ILND, only the nuclear dynamics are linearized. The classical electronic degrees of freedom are not linearized. A similar “half-linearized” approach to dynamics was developed by Sun and Miller,<sup>17</sup> although their method was not applied to nonadiabatic dynamics. Sun and Miller's method does not solve the inverted potential problem. In the LAND-map method, the dynamics do not evolve directly according to the MMST Hamiltonian. The result is that they do not suffer from the inverted potential problem.

## Chapter 2

# Time-Dependent Monte Carlo

One of the major challenges in semiclassical theory is the large number of trajectories required to converge a trajectory. As discussed in chapter 1, this is largely the result of the sign problem, and can't be avoided without losing the ability to capture some parts of physics.

Even so, any effort to reduce the number of trajectories required by semiclassical calculations will make semiclassical methods more attractive, and so this chapter will describe several related ideas to reduce the total number of trajectories required by including time-dependent information in the Monte Carlo sampling function.

Some of the ideas to use TDMC methods were originally explored by Sun and Miller.<sup>45</sup> However, that work focused on the phase histograms (which we will return to in chapter 3), whereas this work focuses on the structure of the time-dependent sampling function in phase space.

### 2.1 Time-Dependent Monte Carlo

When we perform Monte Carlo integration, we rewrite the integral as

$$\int dx_0 f(x_0) = \int dx_0 w(x_0) \tilde{A}(x_0) = \langle \tilde{A} \rangle_w \quad (2.1)$$

where  $w(x)$  is a normalized distribution function.

We have our choice of how to separate our integrand. In chapter 1, we split it into a time-independent sampling function and a time-dependent quantity to be averaged. I'll call that initial value Monte Carlo.

In this chapter, we're interested in the idea of trying to include as much of the integrand as feasible in the the sampling function. Before specializing to examples using the SC-IVR (in particular, the DHK-IVR), let's treat the problem as follows. We assume that our integrand,  $f(x_0)$ , can be written as:

$$f(x_0; t) = A(x_0)B(x_0; t) \quad (2.2)$$

where all the time dependence is contained in  $B(x_0; t)$  ( $A(x_0)$  is time-independent).

When we write the integrand like that, it becomes clear that for any point to contribute to the integral, it must be non-negligible for both the function  $A(x_0)$  and the function  $B(x_0; t)$ . This

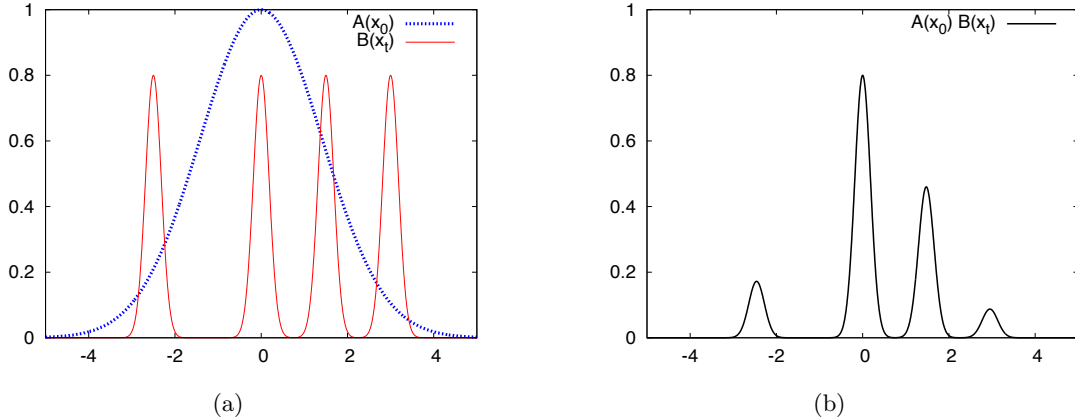


Figure 2.1: Comparison of two ways of sampling a positive definite  $A(x_0)B(x_t)$ . (a) Using  $A(x_0)$  as the sampling function, we see that we sample many regions where the total integrand is nearly zero. (b) Using the whole function for sampling, we have several distinct regions of sampling, but we don't sample where the integrand is nearly zero.

means that we can consider  $A(x_0)$  as an envelope for the whole function. This idea is illustrated for a hypothetical function in figure 2.1. We show a broad (Gaussian) initial distribution  $A(x_0)$ , and a time-evolved distribution  $B(x_0; t)$  which has contributions at four distinct peaks.\* If we sample using just the initial envelope distribution  $A(x_0)$ , we are certain to capture all the peaks of  $B(x_0; t)$  which contribute to the total integrand. However, if  $B(x_0; t)$  is sufficiently sparse, we will also spend a lot of time sampling regions where  $B(x_0; t) \approx 0$ . For example, in figure 2.1, we're less likely to sample around  $x = -2.5$  (the leftmost peak of  $B(x_0; t)$ ) than we are to sample around  $x = -1.0$  (where  $B(x_0; t) \approx 0$ ). Those samples where  $B(x_0; t) \approx 0$  represent wasted computational time.

On the other hand, if we sample from the product  $A(x_0)B(x_0; t)$ , shown in figure 2.1(b), we (by construction) only sample the regions which are important to the total integral. However, we do find another problem: we end up with distinct sampling regions, so we must find ways to get from one region to another.

In this chapter, we'll explore three different plans for Monte Carlo sampling: Initial Value Monte Carlo, Endpoint Time-Dependent Monte Carlo, and Path Sampling Time-Dependent Monte Carlo. Cartoons illustrating the difference in these three sampling methods are shown in figure 2.2.

### 2.1.1 Initial Value Monte Carlo

Before introducing the time-dependent Monte Carlo methods, let's start by reviewing the advantages and disadvantages of the more familiar Monte Carlo sampling method described previously, which I'll call initial value Monte Carlo (IVMC).

---

\* This hypothetical is not at all an impossible case — in fact, it is designed to be reminiscent of the situation we find in section 2.2.2, in particular figure 2.9.

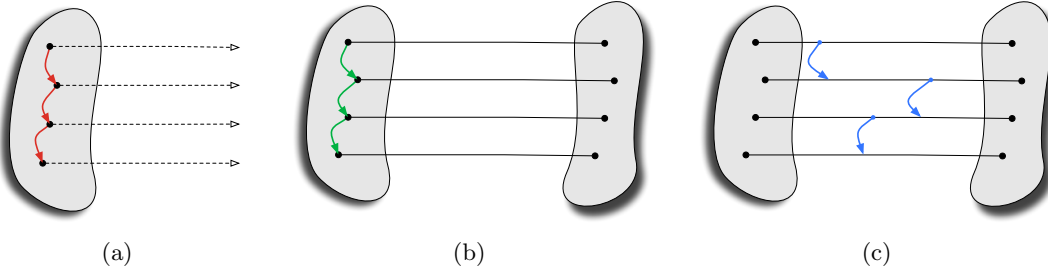


Figure 2.2: Cartoon illustrating (a) Initial Value Monte Carlo, (b) Endpoint Time-Dependent Monte Carlo, and (c) Path Sampling Time-Dependent Monte Carlo.

IVMC is defined by taking a sampling function at time zero, using it to select initial conditions, and then running trajectories from that set of initial conditions.

One of the primary advantages of IVMC is that it allows one to separate the Monte Carlo from the dynamics. This means that a single Monte Carlo calculation can be used for all times in the correlation function.

Another advantage of IVMC is that by doing the Monte Carlo first, the remaining problem of running the many (independent) trajectories is embarrassingly parallel. It's also quite simple to code.

On the other hand, it has the potential to be very wasteful. The sampling function for IVMC, which is typically related to the time independent function, can be seen as an envelope that goes over the whole of the important space. However, not all points within that envelope will be important — the points that are important will be selected by the time-dependent function.

This means that many points which are selected by IVMC will end up giving a contribution of zero to the total integrand (at least, at a given time). Which points are irrelevant will vary by time. However, some quantities only require calculation at a given time (or, frequently, at long time — many quantities are related to long-time limits of correlation functions). For these cases, it would be good to avoid the waste of calculating the points which are irrelevant at that time.

### 2.1.2 Endpoint Time-Dependent Monte Carlo

The basic idea of time-dependent Monte Carlo is that, instead of sampling from some function based on the time-independent envelope, we'd like to sample from the full time-dependent function. This allows us to avoid wasting effort by calculating points that do not contribute to the integral. In fact, we can choose to sample from the magnitude of the time dependent integrand, and simply average the associated phase. That is, we can calculate the integrand as

$$\int dx_0 A(x_0)B(x_0; t) \propto \left\langle e^{i \arg(A(x_0)B(x_0; t))} \right\rangle_{|A(x_0)B(x_0; t)|} \quad (2.3)$$

All of our time-dependent Monte Carlo methods will use this scheme for sampling. The difference between endpoint time-dependent Monte Carlo and path sampling time-dependent Monte Carlo will be in the method used to move through the phase space of initial conditions.

Endpoint time-dependent Monte Carlo (EP-TDMC) samples by moving in phase space at time  $t = 0$ . This picture corresponds naturally with the idea that the integral is over initial conditions: we start with a value of  $x_0$ , calculate the time-dependent sampling function associated with that initial condition, and our Monte Carlo step moves us to another initial condition  $x'_0$ .

As mentioned above, the weight function from which we sample must be normalized. In IVMC,  $\rho(x)$  is chosen so that it is normalized (frequently, the normalization constant can be determined analytically). In TDMC, we need to calculate the norm, *i.e.*, we need to calculate

$$N_t = \int dx |A(x_0)B(x_0; t)| \quad (2.4)$$

We return to the IVMC method to solve this. The key assumption here is that this integrand, which is positive semidefinite, will converge more quickly than the complex integrand with which we started. In the case of SC-IVRs, that complex integrand tends to be highly oscillatory — moreover, the interesting quantum effects are due to the highly oscillatory nature of the integrand. So to average the phase (a difficult problem) we limit ourselves to important trajectories using TDMC. To calculate the magnitude (a simpler problem) we use IVMC.

### 2.1.3 Path Sampling Time-Dependent Monte Carlo

To extend EP-TDMC, I developed path sampling time-dependent Monte Carlo (PS-TDMC). The premise of PS-TDMC is that, when dealing with deterministic trajectories of fixed length in time, an integral over initial conditions is equivalent to an integral over paths. So instead of treating the Monte Carlo move as a step in the space of initial conditions, PS-TDMC treats the Monte Carlo move as a step in the space of trajectories.

PS-TDMC uses the same sampling function as EP-TDMC, but it allows different moves in trajectory space. Taking its inspiration from transition path sampling, PS-TDMC proposes a two-step rule to select a new trajectory. First, a point in time is randomly selected along the trajectory, and the point in phase space is moved at that time. Then the trajectory is calculated forward and backward in time, and the value of the sampling function is determined.

If the probability of generating a trial move is equal to the probability of generating the reverse trial move (*i.e.*, the underlying matrix of the Markov chain is symmetric) then the Metropolis scheme will satisfy detailed balance.<sup>46</sup> For this algorithm, that's clearly the case: we have an equal probability of choosing the same time along the trajectory, and then, just as in the original algorithm, we have an equal probability of choosing the reverse move in phase space.

### 2.1.4 Sampling Multiple Domains: The Dual-Delta Method

One of the downsides of using TDMC is that the sampling function can consist of multiple domains on importance, as shown as a cartoon in figure 2.1 (and shown in a realistic situation in figure 2.9). The source of this can be made clear if we consider a survival amplitude calculation at long time. The basic problem is a manifestation of the root search problem described in section 1.1.1: any trajectory that starts and ends in an important region of phase space will contribute to the overall integrand. But, for a given pair of positions (within the envelope of

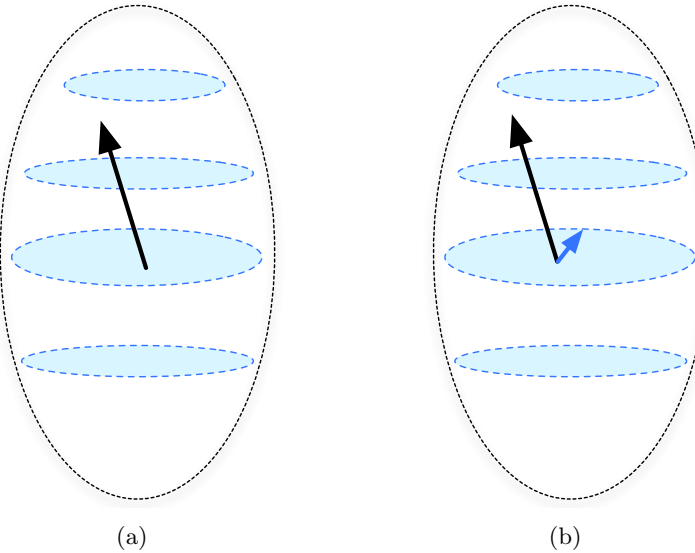


Figure 2.3: Cartoon illustrating two methods for sampling distributions with multiple domains within an envelope: (a) represents the “big-delta” method, which only uses the Monte Carlo step appropriate to the envelope function; (b) represents the “dual-delta” function, where two step sizes are possible; one from the envelope function and one from the smaller domain.

important points), there could be more than one momentum (also within the envelope of important points) to connect them.

This can be a problem if the Monte Carlo step size is determined without prior knowledge of the multiple domains of the distribution — one can find an optimal acceptance ratio for a single domain, instead of for the whole probability distribution function, and be left with a Monte Carlo step size that is unable to traverse from one domain to another. This procedure of optimizing the Monte Carlo step size to a given acceptance ratio, which is risky for TDMC sampling, will be referred to as the “optimized-delta” trial step size.

The most naïve way to fix this problem would be to use a large step size: since all the domains of the TDMC distribution fall within the envelope of the IVMC distribution, we could use the step size appropriate to the IVMC step size. I call this method “big-delta.” The problem with the big-delta method returns to the issue that TDMC was trying to avoid, because we calculate, and then reject, the trajectories that make negligible contributions to the integral. As a result, the Monte Carlo will have a very low acceptance rate.<sup>†</sup>

I propose another way to do this, which will allow us to have a good Monte Carlo acceptance rate regardless of the sparsity of the TDMC sampling function in the IVMC sampling function. My idea, which I call “dual-delta,” involves storing two Monte Carlo step sizes: one associated with the IVMC sampling, and one associated with the TDMC sampling. At each

---

<sup>†</sup> This isn’t actually as bad as it sounds: if we compare it to IVMC, then the many rejected trajectories are trajectories which would not have contributed significantly to the integral. As we’ll note in section 2.1.5, we don’t include the Herman-Kluk prefactor (the most expensive part of the calculation) in the sampling function. Therefore, we do obtain an improvement by throwing those trajectories before wasting the time to calculate the prefactor.

Monte Carlo step, one selects which step size to use at random (we'll define  $p_{\text{big}}$  as the probability of using the IVMC step, leaving the probability of using the smaller TDMC step as  $1 - p_{\text{big}}$ ). Then we make the rest of the Monte Carlo move as usual.

The probability  $p_{\text{big}}$  is a free parameter — as long as it is non-zero, we should sample the full distribution (assuming that the larger MC step size is on the order of the size of the time-independent envelope distribution). In the limit that  $p_{\text{big}}$  approaches unity, we recover the big-delta method. In the limit that  $p_{\text{big}}$  approaches zero, we recover the original result from TDMC sampling. This indicates that too small of a value of  $p_{\text{big}}$  will make it difficult to converge the calculation, since the proportion of trajectories in each subdomain will not be converged.

Either of these methods will work for either EP-TDMC or for PS-TDMC sampling methods. Both the underlying matrix of the Markov chain for both EP-TDMC and PS-TDMC is symmetric. Detailed balance for the big-delta method is completely trivial, since it is equivalent to a (poor) choice of step size in the standard version of the algorithm. For the dual-delta method, we simply add a step where we choose which Monte Carlo step size to use: since the probability of each choice is the same at all points, the symmetry of the underlying matrix is retained, and we still have detailed balance.

It is also worth noting that PS-TDMC was originally developed in the hope that it might solve the problem of sampling multiple domains. In fact, it could — however, that will only happen if the system is chaotic. By definition, a small change in a trajectory at one time leading to large changes in the trajectory at other times indicates chaos. Normally we think of that as a change in the initial conditions affecting the final conditions, but it applies equally to a change at some arbitrary time on the trajectory affecting the initial conditions. The problem is that our move in phase space is the same kind of move as used in our EP-TDMC. Another approach might be to use a shooting-like algorithm, where the total energy of the particle is drawn from a distribution based on the IVMC sampling, but the direction of the velocity is chosen at random.

### 2.1.5 Specializing to the DHK-IVR

To this point, we've discussed a generic phase space integral (although we've been motivated by considerations from the SC-IVR). Now I'd like to consider the specific case of the Double Herman-Kluk IVR, which is given by:

$$C_{AB}(t) = \int d\Omega_0 \int d\Omega_{0'} \langle \Omega_0 | \hat{A} | \Omega_{0'} \rangle \langle \Omega_{t'} | \hat{B} | \Omega_t \rangle C_t C_{t'}^* e^{i\Delta S} \quad (2.5)$$

where  $\Omega = (p, q)$ , a point in phase space.

In this case, the time-independent quantity from the previous sections is  $\langle \Omega_0 | \hat{A} | \Omega_{0'} \rangle$ . However, we'll note a slight subtlety in the time-dependent part: we can split the time-dependent part into multiple sub-parts. First, we have an “easy” part,  $\langle \Omega_{t'} | \hat{B} | \Omega_t \rangle$ , which only requires the calculations of normal dynamics. Then we have a “hard” part,  $C_t C_{t'}^*$ , which requires the propagation of matrices as well as the phase space vector. The dynamics for this second part takes more computational effort than the dynamics for the first part. Finally, we have the term

$e^{i\Delta S}$ , which is just a phase factor, and therefore plays no role in the magnitude of the time dependent function.

IVMC sampling on this integrand is done in the usual way: we define some normalized sampling function  $\rho(\Omega_0, \Omega_{0'})$  which typically resembles the magnitude of  $\langle \Omega_0 | \hat{A} | \Omega_{0'} \rangle$ . Then we sample the integrand as:

$$C_{AB}(t) = \left\langle \frac{\langle \Omega_0 | \hat{A} | \Omega_{0'} \rangle}{\rho(\Omega_0, \Omega_{0'})} \langle \Omega_{t'} | \hat{B} | \Omega_t \rangle C_t C_{t'}^* e^{i\Delta S} \right\rangle_{\rho(\Omega_0, \Omega_{0'})} \quad (2.6)$$

The TDMC sampling on this integrand makes use of the fact that Metropolis Monte Carlo rejects some trial moves. We choose to sample the integrand as

$$C_{AB}(t) = \left\langle C_t C_{t'}^* e^{i\Delta S} e^{i\phi} \right\rangle_{|\langle \Omega_0 | \hat{A} | \Omega_{0'} \rangle \langle \Omega_{t'} | \hat{B} | \Omega_t \rangle|} \quad (2.7)$$

where  $\phi = \arg(\langle \Omega_0 | \hat{A} | \Omega_{0'} \rangle \langle \Omega_{t'} | \hat{B} | \Omega_t \rangle)$ . By not putting the prefactor in our sampling function, we avoid the waste of calculating the expensive prefactor dynamics for a trajectory that we then reject. However, this does mean that each trajectory must be run twice: once to select the points from the sampling function, and once to track the dynamics of the semiclassical prefactor.

## 2.2 Results

The DHK-IVR can be used to study a wide variety of systems, but for our first analyses, we'll restrict ourselves to 1-dimensional systems (which means a 4-dimensional integral for the DHK-IVR). In fact, these are both Morse oscillators (with very different parameters). Both of these systems start with a (pure) coherent state a projection operator as the  $\hat{A}$  operator, which makes the IVMC sampling particularly simple. We look at two different  $\hat{B}$  operators.

### 2.2.1 Position Probability Distribution for $I_2$

The position probability distribution is a typical function for TDMC, because it is a quantity which we usually want to observe at a specific given time. In this case, we'll look at it for a Morse oscillator representation of  $I_2$  at 192 fs, which is roughly one period.

The potential energy function for this system is given by

$$V(q) = D_e \left( 1 + \left( 1 - e^{-\beta(q-q_0)} \right)^2 \right) \quad (2.8)$$

with the parameters

$$D_e = 0.0571682424 \text{ a.u.} \quad (2.9)$$

$$\beta = 0.9826704 \text{ a.u.}^{-1} \quad (2.10)$$

$$q_0 = 5.0402645 \text{ a.u.} = 2.666 \text{ \AA} \quad (2.11)$$

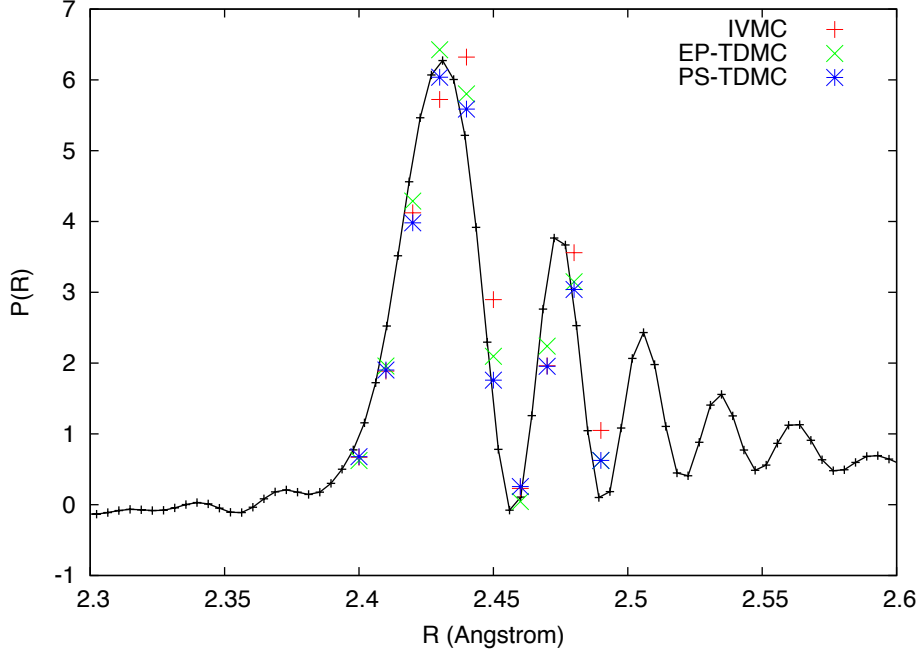


Figure 2.4: Radial probability distribution for  $\text{I}_2$ , calculated by FB-IVR (black line), and DHK-IVR with IVMC (red), EP-TDMC (green), and PS-TDMC (blue) sampling.

The position probability distribution  $P(R; t)$  is the correlation function where  $\hat{A} = |\psi\rangle\langle\psi|$  and  $\hat{B} = \delta(\hat{q} - R)$ . We use the initial state  $|\psi\rangle$  given in the position representation by

$$\langle q|\psi\rangle = \left(\frac{\gamma}{\pi}\right)^{1/4} e^{-\frac{\gamma}{2}(q-q_\psi)^2 + ip_\psi(q-q_\psi)} \quad (2.12)$$

where our state has the parameters

$$\gamma = 135.413108 \quad (2.13)$$

$$q_\psi = 4.536862 \text{ a.u.} = 2.4 \text{ \AA} \quad (2.14)$$

$$p_\psi = 0 \text{ a.u.} \quad (2.15)$$

The width  $\gamma$  is chosen to fit the harmonic frequency of the potential surface, *i.e.*,  $\gamma = \sqrt{V''(q)/m}$  with mass  $m = 116500.0$  a.u. (the reduced mass of  $\text{I}_2$ ).

These parameters correspond to a iodine molecule photoexcited from its ground state into an electronically excited state. The position probability function for this 1D system is equivalent to the (nuclear) wavefunction in terms of the internuclear distance.

For the IVMC sampling function, we use:

$$\rho(\Omega_0, \Omega_{0'}) = |\langle\Omega_0|\psi\rangle\langle\psi|\Omega_{0'}\rangle|^2 \quad (2.16)$$

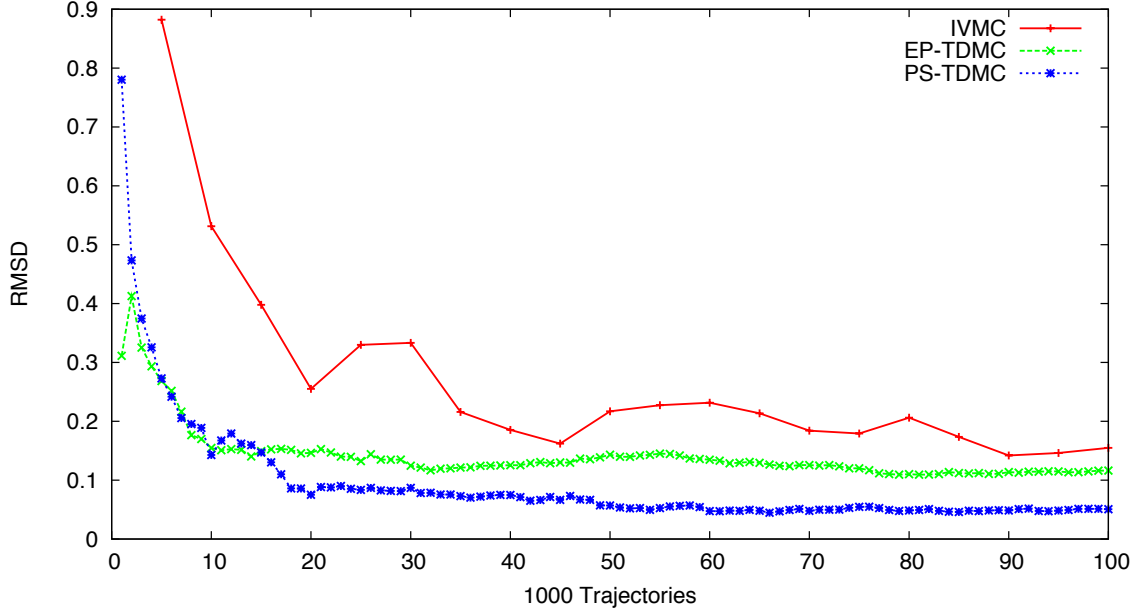


Figure 2.5: Convergence of various methods for the radial probability distribution of  $I_2$  (as a root-mean-square deviation over several initial random seeds).

The  $\hat{B}$  operator in this system is  $\hat{B} = \delta(\hat{q} - R)$  for a given  $R$ . Its matrix elements are easily calculated:

$$\langle q_a p_a | \delta(\hat{q} - R) | q_b \rangle [b] = \int dq' \langle q_a p_a | q' \rangle \langle q' | \delta(\hat{q} - R) | q_b p_b \rangle \quad (2.17)$$

$$= \langle q_a p_a | R \rangle \langle R | q_b p_b \rangle \quad (2.18)$$

$$= \sqrt{\frac{\gamma}{\pi}} \exp\left(-\frac{\gamma}{2} \left((R - q_a)^2 + (R - q_b)^2\right) - ip_a(R - q_a) + ip_b(R - q_b)\right) \quad (2.19)$$

We'll compare results to the FB-IVR result for the same, which has been shown to match well with the full quantum results for this system. The results from the LSC-IVR do not match the correct results, indicating that quantum coherences play an important role.<sup>28</sup>

Figure 2.4 shows that all three methods can accurately reproduce the FB-IVR result for the radial distribution. In particular, they all capture the oscillations, which are the result of quantum dynamical coherences. Both of the TDMC calculations are performed with the optimized-delta method for selecting trial points, and the accuracy indicates that, at least in this domain, this method is sufficient.

In figure 2.5 we consider how rapidly this result is achieved (for  $R = 2.43$  Å). The calculation was run with several different initial seeds, and the root-mean-square deviation was calculated as a function of the number of trajectories run. The IVMC sampling method is still settling to its asymptote around 100k trajectories, while both of the TDMC methods have reached

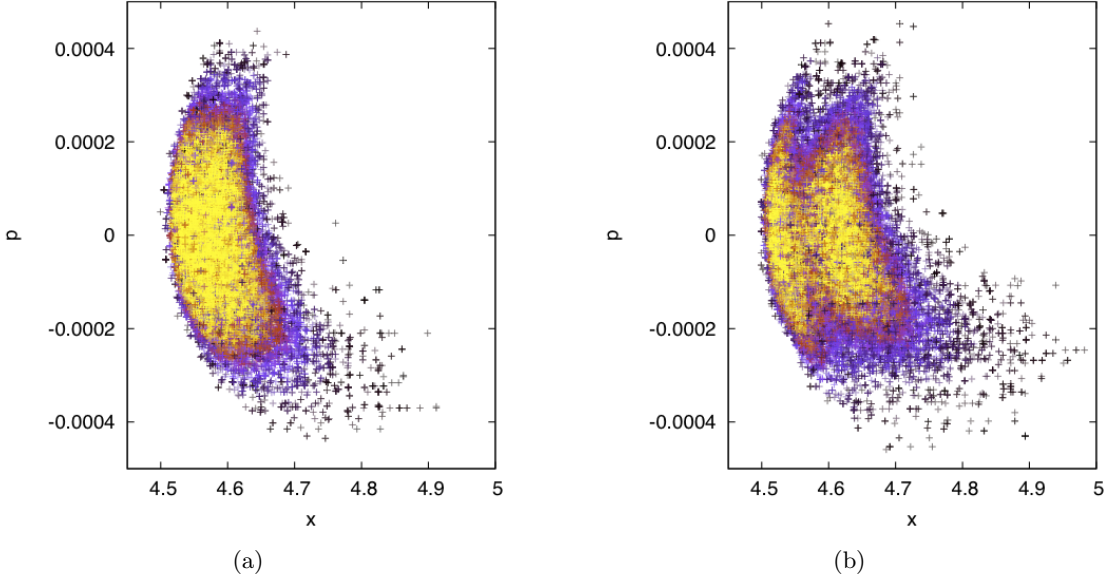


Figure 2.6: Phase space plots (in atomic units) of the distribution sampled by the TDMC methods for calculating the radial distribution of I<sub>2</sub> nuclei at  $t = 192$  fs for (a) 2.43 Å and (b) 2.49 Å.

theirs by 20k trajectories. Further, the RMSD is smaller for the EP-TDMC than for IVMC, and smaller still for PS-TDMC.

Figure 2.4 shows the results of using an optimized-delta version of the TDMC calculations (*i.e.*, using only the small steps from the dual-delta methodology). This is sufficient to accurately capture the results. Figure 2.6(a) shows the phase space sampled (first 50,000 points) by TDMC for  $R = 2.43 \text{ \AA}$ . Figure 2.6(b) shows the same for  $R = 2.49 \text{ \AA}$ . While figure 2.6(a) has one primary region of important phase space, figure 2.6(b) shows two regions which have begun to separate. When we compare this with the respective points in figure 2.4, we note that  $R = 2.43 \text{ \AA}$  (where there is only one important region of phase space) is at the top of a peak, where there is no destructive interference. On the other hand,  $R = 2.49 \text{ \AA}$  (where there is more than one important region in phase space) is at the bottom of a trough, where nearly all the probability is killed by destructive interference.

Using these TDMC methods allows us to study what regions of phase space contribute at different times. In particular, it allows us to identify what regions of phase space lead to the development of quantum coherences.

### 2.2.2 Survival Amplitude of an Anharmonic Morse Oscillator

We'll also test this method on a Morse oscillator with parameters originally described in reference 47. The potential energy is given by

$$V(q) = 30.0 \left( 1 + (1 - e^{-0.08q})^2 \right) \quad (2.20)$$

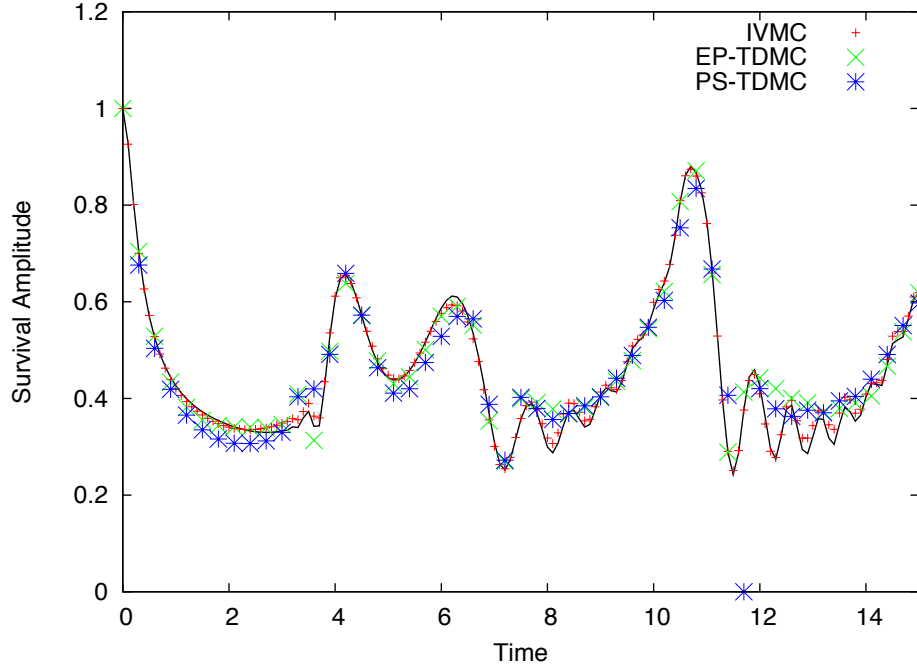


Figure 2.7: Survival amplitude for the anharmonic Morse oscillator calculated with optimized delta. Note the failure to reproduce the correct result from around times 7-9 and times 12-14.

and the initial wavepacket has the position-space representation

$$\langle q|\psi\rangle = \left(\frac{12}{\pi}\right)^{1/4} e^{-6q^2+ipq} \quad (2.21)$$

This system is described in detail in appendix A.2.

To test this methodology, we'll measure the survival amplitude of this system, which is given by  $\mathcal{A}(t) = \sqrt{C_{AB}(t)}$ , where  $\hat{A} = \hat{B} = |\psi\rangle\langle\psi|$ .

This particular quantity suffers from the problem that, as a time-dependent calculation, the TDMC methods require a separate calculation at each time, whereas the IVMC only requires one calculation for all times. However, using this sort of system allows us to see how the methodology fares for different types of distribution functions, and will highlight some of the practical challenges faced in time-dependent Monte Carlo sampling.

In this case, we use the single-HK method for calculating the survival amplitude as our standard. It has previously been shown to accurately reproduce the quantum results for this system.<sup>47</sup>

Since we have the same  $\hat{A}$  operator, we use the same IVMC sampling function as the  $I_2$  system:  $\rho(\Omega_0, \Omega_0') = |\langle\Omega_0|\psi\rangle\langle\psi|\Omega_0'\rangle|^2$ .

Our first calculation for this system is done using the automatically optimized choice of Monte Carlo step size (*i.e.*, the step size that gives approximately 50% acceptance rate for any degree of freedom). The result of this calculation can be seen in figure 2.7. While the gross

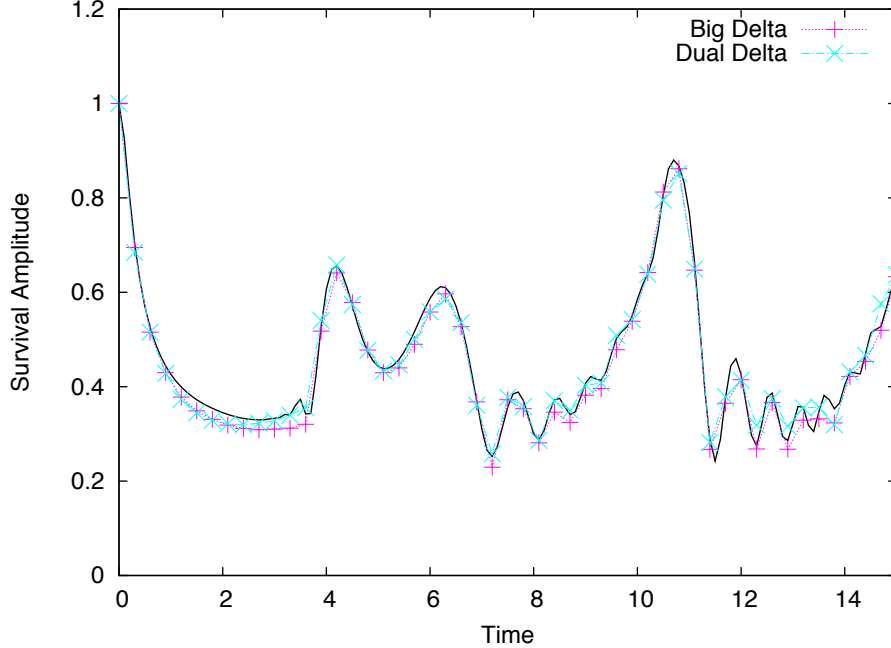


Figure 2.8: Survival amplitude for the anharmonic Morse oscillator calculated by the DHK-IVR, with EP-TDMC sampling. Sampling trials for the pink points were selected by the big-delta method; trials for the light blue points were selected by the dual-delta method.

structure of the correlation function is preserved, this method is unable to capture some of the oscillations between the main peaks. These oscillations are the result of interference from the action term between different trajectories (see section A.2 for a discussion of this).

The reason these features were not captured is evident when we consider the distribution of points sampled: in figure 2.9, we show the regions of phase space sampled by different methods for this system at time  $t = 12.3$ . Figure 2.9(a) shows the sampling for the IVMC method. This is our envelope function which plays a role at all times. In figures 2.9(b) and 2.9(d), we see the sampling that we should get from TDMC (with nearly the same results given by big-delta and dual-delta methods). Figure 2.9(c) shows what we actually get with the optimized-delta method to select trial states. Since the regions are completely separated, a Monte Carlo step that corresponds to a 50% acceptance rate is necessarily too small to make the jump from one region to another. In particular, we see in this the momentum coordinate. Along the momentum coordinate from one region to another, less than 50% of the space is occupied by important trajectories. Therefore, it is impossible to have a step size that gives a 50% acceptance rate and is large enough to sample multiple regions.

This leads us to the considerations discussed in section 2.1.4: in order to jump between these regions, we need to use a larger Monte Carlo step size. We can either use the big-delta method or the dual-delta method: as shown in figure 2.8, either reproduces the correct result. Figure 2.9 demonstrates that both methods also result in the same sampling of phase space.

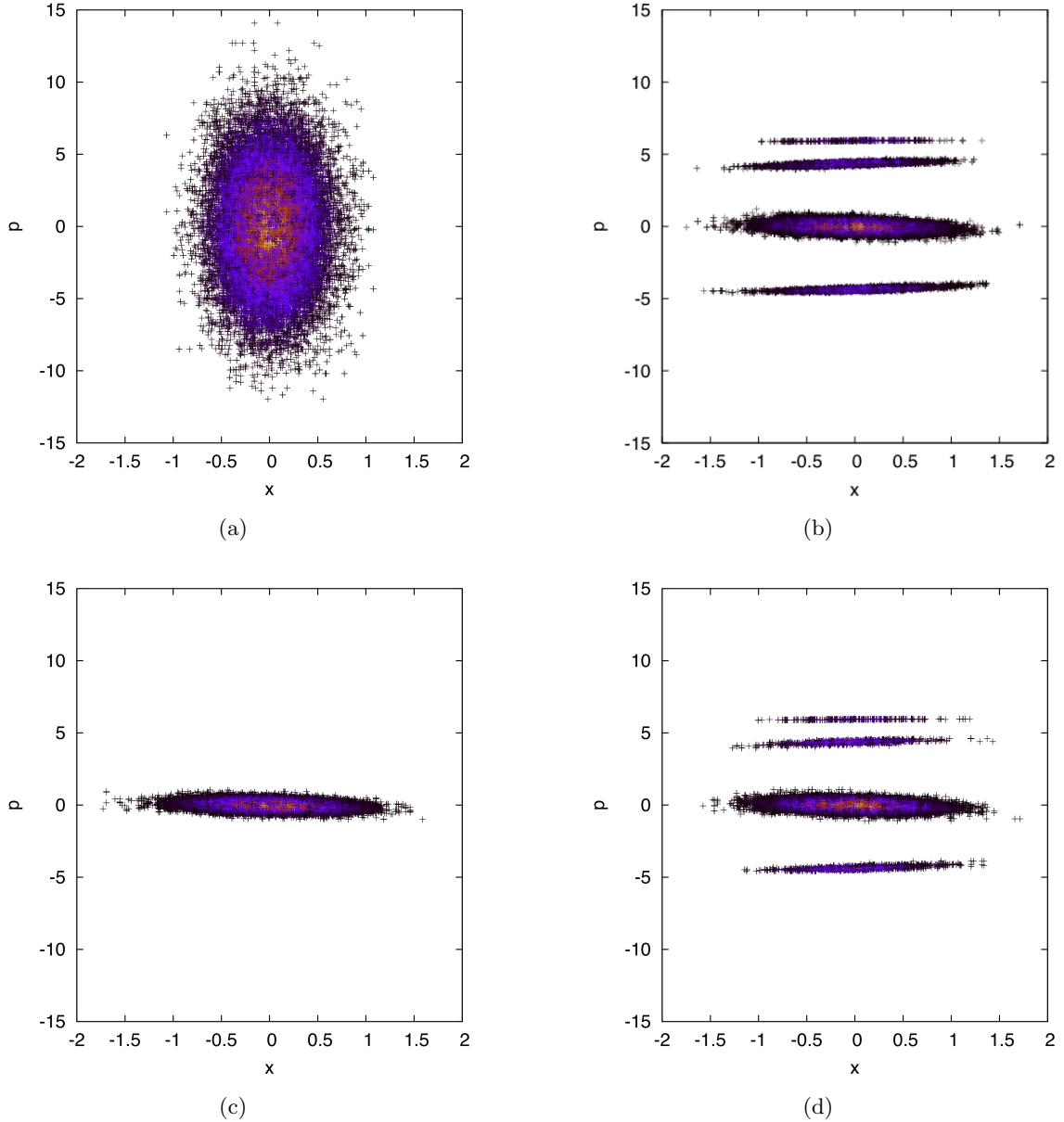


Figure 2.9: Phase space for calculating the anharmonic Morse oscillator survival amplitude at  $t = 12.3$  for various sampling methods: (a) IVMC, (b) EP-TDMC with big-delta trial selection, (c) EP-TDMC with optimized delta ( $\sim 50\%$  acceptance ratio) trial selection, and (d) EP-TDMC with dual-delta ( $p_{\text{big}} = 0.1$ ) trial selection.

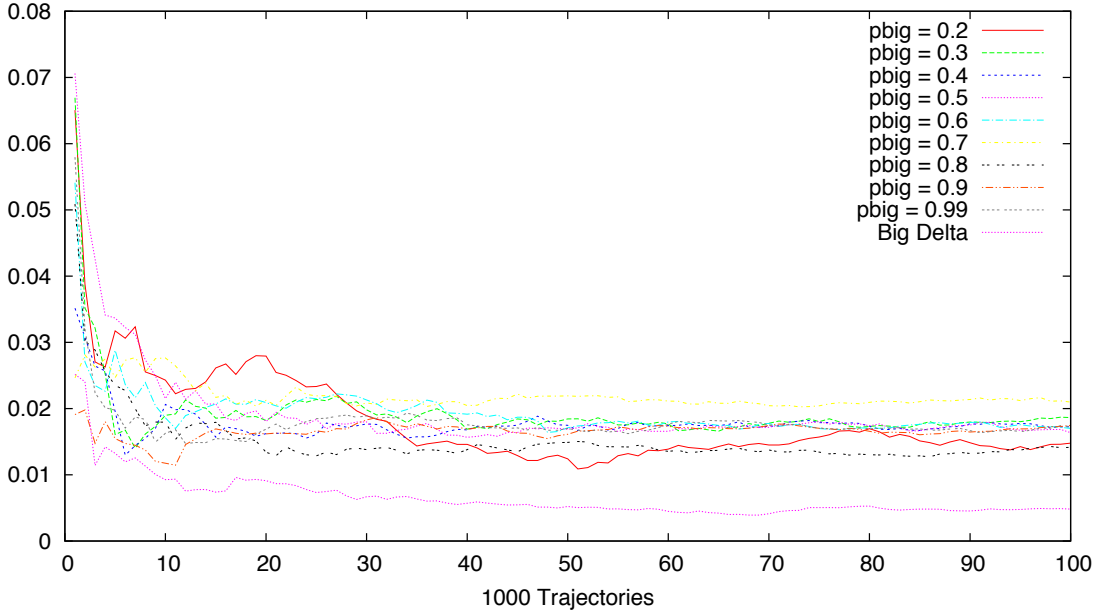


Figure 2.10: Convergence of the survival amplitude for the anharmonic Morse oscillator at  $t = 12.3$  for EP-TDMC with the dual-delta trial selection (with several values of  $p_{\text{big}}$ ) compared to big-delta trial selection.

The question then becomes about the relative efficiency of these two methods. In figure 2.10 we compare the convergence of the big-delta method to the dual-delta method with various choices of  $p_{\text{big}}$ . The result is, somewhat to my surprise, that the big-delta version is more efficient than the dual-delta version. The choice of  $p_{\text{big}}$  makes very little difference in the dual-delta results; the best results, from  $p_{\text{big}} = 0.8$ , are marginally better than the others. It's particularly interesting that it doesn't appear that we approach the big-delta result in the limit that  $p_{\text{big}}$  approaches unity.

This may be because the specific method employed here was to select the small step size such that the total probability of a move being accepted was around 50%. As a result, a larger frequency of choosing the larger step (larger value of  $p_{\text{big}}$ ) is compensated by increasing the acceptance probability of the smaller step, *i.e.*, making it smaller. This may not be the best way to approach the problem.

## 2.3 Discussion

This chapter has primarily explored three ideas: first, we compare the IVMC, EP-TDMC, and PS-TDMC methods for sampling. Second, we have compared the big-delta, dual-delta, and optimized-delta methods for selecting trial states when doing time-dependent Monte Carlo. Finally, we look at what these phase space plots can teach us about the way that we capture quantum effects.

As we see in figure 2.5, the convergence of IVMC is slower than that of either of the time-dependent Monte Carlo methods. This is hardly surprising, since IVMC is guaranteed to sample many trajectories which have a very small contribution to the total integrand, and that will significantly slow the convergence. For the system in figure 2.5, the PS-TDMC method converges to a slightly better RMSD than the EP-TDMC method does, although it takes a little longer to level off — around 20k trajectories for PS-TDMC, compared to 10k trajectories for EP-TDMC.

The method that we have usually used to select the Monte Carlo step size is the optimized-delta method: the step size is selected such that the acceptance ratio is around 50%. However, when using a time-dependent Monte Carlo method, our sampling function can consist of distinct areas in phase space separated by regions where the sampling function is nearly zero. This means that it can be impossible to have a single step size that is large enough to “jump” from one region to another while maintaining the 50% acceptance ratio, as evidenced in figure 2.9. Both the big-delta and dual-delta methods are capable of sampling the full phase space (and thus succeed in capturing the quantum effects). In figure 2.10 we found that the big-delta sampling method performed better than the dual-delta sampling for this system. This may be the result of the specific system: sampling along the position axis is about the same for any sampling method; only the momentum axis changes. Perhaps a more sparse time-dependent sampling function would be better served with the dual-delta method. The other point to note is that even if we find that the big-delta method is most efficient, we can still benefit from the TDMC methods for larger systems because our rejected trajectories don’t involve the expensive prefactor calculations. That is, while IVMC doesn’t “reject” the trajectories that contribute nearly zero to the integrand, they’re still wasted calculations, and they involve the expensive step of calculating the prefactor. Big-delta TDMC methods will reject those trajectories (after calculating the prefactor-free dynamics) but never calculate the prefactor for them. For systems of more than a few degrees of freedom, this can represent a significant reduction in computational time.

The last point to consider is less about computational efficiency than about how this perspective on the semiclassical calculation can improve our understanding and intuition about semiclassical calculations in general. As discussed in chapter 1, we know that certain types of quantum effects (which we typically refer to as “true quantum dynamical coherences” or some subset of those words) can be seen in the Feynman path integral picture as resulting from interferences of the path actions between different paths. In semiclassical theory, this means that the phase factors associated with the classical actions interfere when doing the integral over phase space.

When we consider this, it is not surprising that there might exist distinct regions in phase space which are associated with trajectories that would interfere with each other. Even so, it is interesting to see what these regions look like. Further, we have shown that even in cases of full destructive interference, these regions can still be connected (*e.g.*, figure 2.6(b)). In regions of partial destructive interference, we can see multiple widely-separated regions, as shown in figure 2.9. Even if this doesn’t provide us with a practical computational method, it does give us further insight into the nature of the semiclassical treatment of quantum effects.

## 2.4 Future Directions

The most obvious way to take this forward is to do exactly what I have already done, but on other systems. I do think that there's at least one more question to be answered that way, as described in subsection 2.4.1 below. However, a potentially more interesting future direction to take this line of research is to use the lessons learned from it (detailed in the discussion above) and develop algorithms which take advantage of those ideas to better approximate SC-IVR calculations.

One point to reiterate here is that, while we have used the tools developed in this chapter for the DHK-IVR, it is in no way limited to that problem. Application to the LSC-IVR and the single-propagator HK-IVR (or VV-IVR) are trivial. Techniques to apply this kind of approach to the FB-IVR were discussed by Sun and Miller.<sup>45</sup>

### 2.4.1 Another System: Tully Model 1

Another calculation which would be of interest is the nuclear momentum probability distribution for the Tully model 1 system.<sup>48</sup> In this system, we have two electronic states and one nuclear degree of freedom. We treat the nonadiabatic dynamics according to the MMST Hamiltonian given in section 1.3. In the Tully model 1 system, the two diabatic curves are symmetric such that  $V_{11}(R) + V_{22}(R) = 0$ . They are essentially flat to either side of an interaction region (where the coupling is described by a Gaussian). Previous studies with SC-IVR methods indicated that the resolution of two momentum peaks comes from the interference of action terms.<sup>27</sup> That is, we cannot capture two peaks in the nuclear momentum distribution using the LSC-IVR, but we can when using the FB-IVR. One presumes that the DHK-IVR will also capture this effect, since it is a more exact theory than the FB-IVR.

The question then becomes what one might expect from this system. We know that the nuclear dynamics from the MMST model essentially follow the Ehrenfest (average potential) dynamics. The conclusion in reference 27 is that destructive interference due to the action term removes contributions from between the two peaks.

Given this, my first hypothesis would be that, for the Tully Model 1 system, this interference would be visible in the  $t = 0$  nuclear momentum distribution. My general thought is that the initial nuclear momentum will serve as the envelope function, and the long-time result will be multiplied by a result (arising from the action) which separates the two peaks. If this proves to be true, it would confirm the interpretation in reference 27.

### 2.4.2 Proposed Method to Approximate IVR Results

The analysis presented above is interesting, but much of it might have been intuited by a sufficiently perspicacious reader. We're already aware that quantum dynamical coherences are the result of interferences between different action phases, and it is hardly surprising that this would lead to certain regions of the action getting “interfered out” of relevance.

The more useful question is whether we can take advantage of that insight to provide a simple approximation to an SC-IVR calculation which might still capture the relevant quantum effects (at least qualitatively, even if not quantitatively).

My proposal is that we should be able to do exactly that, and that the key idea is to use clustering algorithms to identify the regions of importance. Clustering algorithms take the points in a multidimensional space and sort them into groups. The problem is that many of these methods don't scale well with dimensionality. Even so, it would be worth exploring the idea in low dimensionality.

The outline of such a procedure would be this:

1. Run some number of trajectories (without the semiclassical prefactor) using the TDMC method. One must run a sufficient number to identify the sampling regions.
2. Use some clustering algorithm to define approximations to the sampling regions, and the relative weight of each region.
3. Sample from these regions (with appropriate weights) to generate an approximate IVR. The hope is that a small number of trajectories would work: I would start by sampling one trajectory from each region in phase space, starting at its barycenter, and weighted according to the relative weight of that region (determined in the previous step). The hope would be that this extraordinarily simple method would suffice to capture the qualitative nature of true quantum coherences (interference effects).

The basic goal would be to use many inexpensive trajectories (calculated without a prefactor) to determine a very small number of initial conditions to use in the semiclassical calculation. Of course, the benefits associated with not requiring the prefactor in the initial trajectories only become significant as the dimensionality grows — when, unfortunately, the clustering algorithms become difficult.

## Chapter 3

# Phase Histogram IVR

The ideas developed in chapter 2 were based largely on the observation that we could split the Monte Carlo average into its magnitude (as a sampling function) and its phase (the quantity being averaged). In this chapter, we present an idea which is similar in spirit, but takes a different approach to that idea.

In this chapter, we again consider the final calculation as an (appropriately-weighted) average of the phases. But in chapter 2, the phases were the dependent variable, with the trajectory as the independent variable. Here, we will perform the average after constructing a histogram by phase, making the phase the independent variable and the histogram weight into the dependent variable.

Sun and Miller<sup>45</sup> have previously studied phase distributions arising from semiclassical calculations, although they did not look at the time-dependence of the phase distribution, nor did they explore using fitting to further smooth the resulting distribution.

### 3.1 HK-IVR as a Phase Histogram Problem

In this chapter, we will study the phase histogram of the survival amplitude, calculated by a single (HK) propagator method. That is, we're looking at the quantity

$$\mathcal{A}(t) = \langle \psi | e^{-i\hat{H}t} | \psi \rangle \quad (3.1)$$

which, importantly, is complex. Many of the ideas in this chapter could be applied to other semiclassical methodologies and other quantities, and that might even open up other techniques. For example, should we choose to directly study a real-valued quantity (such as the modulus of the survival amplitude, instead of just the amplitude) we could also make use of the fact that the phase histogram would have to be symmetric about zero phase.

In chapter 2 we observed that we can sample a complex integrand by splitting it into its magnitude, which we use as a sampling function, and its phase, which is the quantity which we average. In this chapter, we take an extra step to make the angle associated with the phase into the dependent variable. We obtain a distribution as a function of this angle, which we call the phase histogram (since, in practice, it amounts to histogramming the phase associated with

each trajectory at given time). The Monte Carlo calculation generates the amplitude of the phase histogram.

Mathematically, we express the phase histogram idea as follows:

$$\int dx f(x) = \int dx |f(x)| \exp(i \arg(f(x))) \quad (3.2)$$

$$= \int dx'' |f(x'')| \int d\phi \frac{\int dx |f(x)| \delta(\phi - \arg(f(x)))}{\int dx' |f(x')|} e^{i\phi} \quad (3.3)$$

$$= N \int d\phi \langle \delta(\phi - \arg(f)) \rangle_{|f|} e^{i\phi} \quad (3.4)$$

where  $N = \int dx |f(x)|$ . The quantity  $P(\phi) = \langle \delta(\phi - \arg(f)) \rangle_{|f|}$  is the phase histogram. In order to calculate the integral at that point, the additional steps of multiplying by the normalization constant  $N$  (which is actually included in the phase histograms as described below) and averaging with the  $e^{i\phi}$  term. All of this can be directly applied to the HK-IVR survival amplitude, where the integrals over  $x$  in the expressions above are simply the phase space integrals.

## 3.2 Gaussian Fitting of the Phase Histogram

Of course, if all we do is histogram the phase and then re-average it, we can't expect to gain much in the process (although, as will be shown, the plots of those histograms can provide interesting insight on the nature of the physical processes involved). The more interesting question is whether we can get a good estimate to the correct result by fitting some function to the histogram. In this example, we fit the histogram to a sum of Gaussians, which are then analytically integrated to estimate the contribution at that time.

This shares some of the spirit of the method proposed in section 2.4.2. However, the major advantage to this method is that it only involves fitting a one-dimensional function. The cluster identification idea in section 2.4.2 is a very difficult problem for multidimensional systems.

Even so, the practical matter of fitting Gaussians to the phase histogram requires consideration of a few subtle points. The first is the matter of the bin width in the histogram. If we have too few bins, we risk losing important information about the nature of the interferences. If we have too many bins, the histogram will look jagged and it will be hard to accurately fit our Gaussians. There exist many different ways to estimate the best number of bins to use, usually based on the number of samples (trajectories in our case). One widely used rule of thumb is to use the square root of the number of trajectories. The work presented in this chapter, however, mainly serves as a proof of concept for the calculation we're doing, so the best number of bins will be "eyeballed" after initially calculating with 250 bins. The rehistogramming procedure assumes a flat distribution within each original histogram bin when re-apportioning the weights.

Another detail to consider is the fact that the domain is periodic. Therefore, the fitting function must account for all relevant periodic replicas of the Gaussian. This was done by defining the fitting function to be the sum of  $2\pi$ -periodic Gaussians. Until the Gaussian was 0.1% of its maximum height, its contributions were wrapped around as periodic images.

We use the Levenberg-Marquardt algorithm<sup>49–51</sup> (as implemented in SciPy<sup>52</sup>) to perform our nonlinear fit. One of the features of this method is that it requires an initial guess for the

parameters to be determined. We have split this guessing procedure into two parts: we fit our Gaussians sequentially, so when fitting  $N_g$  Gaussians, we use the results from the previous fit as the guess for  $N_g - 1$  of our Gaussians. The remaining guess is determined by considering the residual of the previous fit (or the full dataset when there is no previous fit) and finding the point with the largest absolute value. This provides a guess for the height and center of the Gaussian. We assume that all of our Gaussians decay to the baseline at zero, so we find the width at half maximum of this peak (paying careful attention to the periodic boundary conditions) in order to estimate the width of our Gaussian. The fit is then performed for the full dataset, allowing the previous Gaussian parameters to change to get the best fit with the addition of the new Gaussian.

### 3.3 Test System: The Quartic Oscillator

The first system we test is a quartic oscillator. This system has been studied before, and shows an interesting recoherence at long time (which the LSC-IVR fails to capture).<sup>29</sup> As explained in chapter 1, the LSC-IVR is unable to capture coherence effects which occur due to the interference of two trajectories with different actions. Since the action is one of the major contributors to the phase, we expect the phase histogram to be delocalized when quantum dynamical effects are important.

The potential energy for this system (with unit mass) is:

$$V(q) = q^2 - 0.1q^3 + 0.1q^4 \quad (3.5)$$

We start with an initial Gaussian wavepacket displaced to the right of the potential with parameters:

$$q_\psi = 1.0 \quad (3.6)$$

$$p_\psi = 0.0 \quad (3.7)$$

$$\gamma = \sqrt{2} \quad (3.8)$$

The phase histogram for calculating the survival amplitude (using the HK-IVR) is shown in figure 3.1(a). We can see that the overall structure of the phase histogram follows a slope that roughly corresponds to the harmonic approximation. At early times, most of the phases that contribute are near the harmonic phase. As time goes on, more structure develops in the phase histogram in regions far from the harmonic phase. This additional structure corresponds to the increasing inaccuracy of the survival amplitude as calculated by the LSC-IVR, as shown in figure 3.1(b). At later times, all phases make some contribution to the phase histogram, but there is still a lot of structure. As we can see in figure 3.1(b), the LSC-IVR treatment of this survival amplitude fails to capture the amplitude of the oscillations as time goes on, and also fails to capture the recurrence of the maximum which we see in the HK-IVR calculation just before  $t = 60.0$ .

To study the Gaussian approximation idea for this system, we choose the time  $t = 55.0$ . From figure 3.1(a) we can see that this is a region where the phase distribution is very delocalized, and as figure 3.1(b) shows, it is also a point where the recoherence which the LSC-IVR cannot

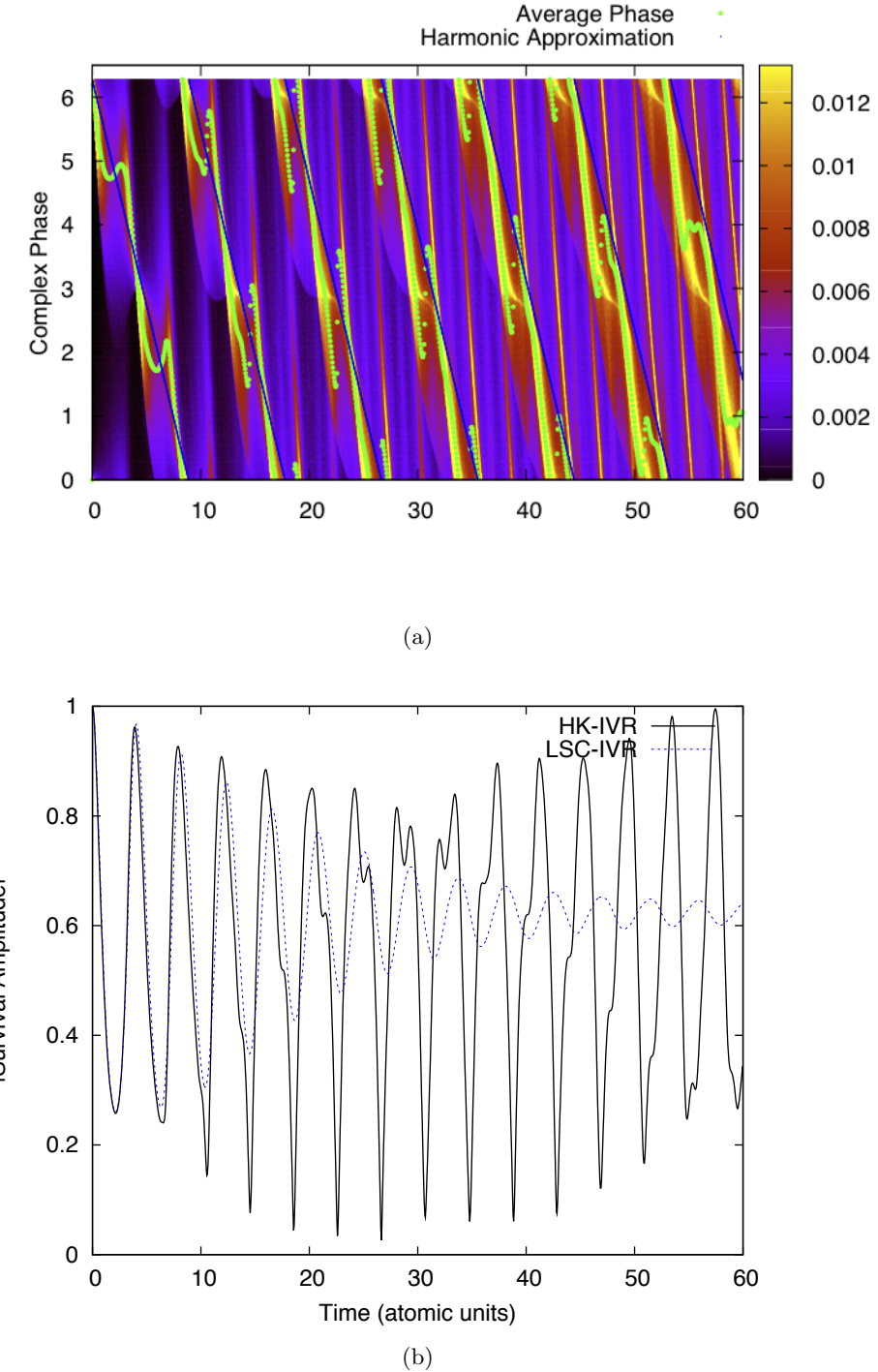


Figure 3.1: Survival amplitude of the quartic oscillator system. (a) Phase histogram of the survival amplitude as a function of time. (b) Modulus of the survival amplitude as calculated by the HK-IVR and LSC-IVR.

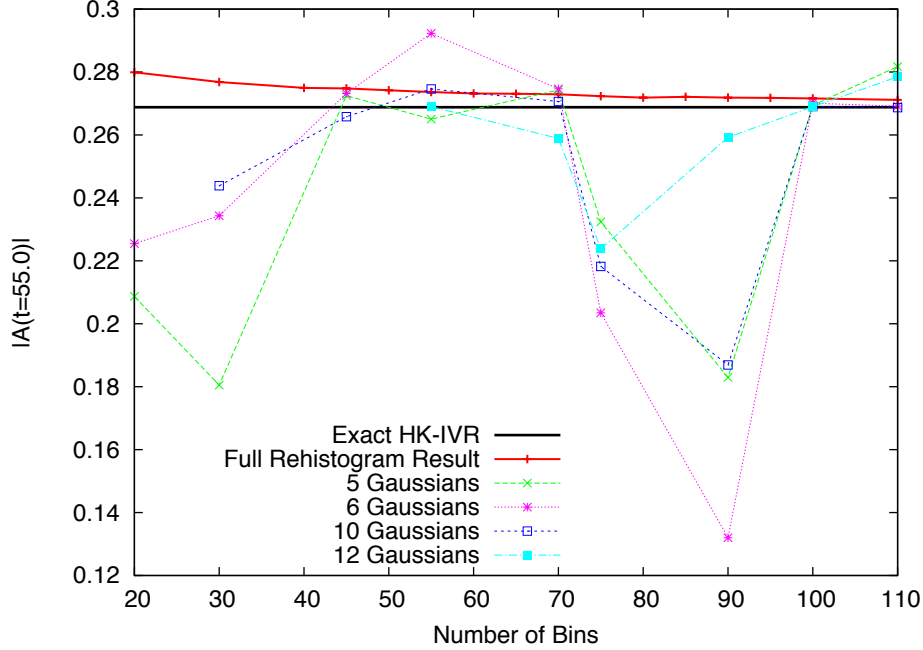


Figure 3.2: Convergence of the Gaussian fit for the quartic oscillator at  $t = 55.0$  as a function of the number of rehistogrammed bins, for different numbers of Gaussians. The exact HK-IVR result is shown, as is the rehistogrammed result for each number of bins.

recapture plays an important role. The HK-IVR gives  $|\mathcal{A}^{\text{HK}}(55.0)| = 0.2688$ . The LSC-IVR result is  $|\mathcal{A}^{\text{LSC}}(55.0)| = 0.6307$ ; more than a factor of 2 too high.

The fitting method described in section 3.2 occasionally fails to fit multiple Gaussians (and, of course, if it fails for  $N_g$  Gaussians, it necessarily fails for  $N_g+1$  Gaussians). This problem seems to be specific to the histogram; using a different number of bins fixes the problems. In addition to that, some numbers of rehistogrammed bins can be extraordinarily difficult to fit.

In addition to the obvious approximation made by fitting the rehistogrammed data to a sum of Gaussians, the re-histogramming is itself an approximation. In figure 3.2, the black line shows the exact HK-IVR result, and the red line shows the full rehistogram results for a given number of bins. As we use fewer bins, the error compared to the exact HK-IVR increases. The full HK-IVR calculation is equivalent to a direct calculation in the infinite-bin limit, and we have essentially no change between that infinite bin result and the 250-bin result with which we start our rehistogramming procedure.

The error introduced by the rehistogramming procedure is smaller than the error from the Gaussian fitting process for any number of bins, although the error due to the Gaussian fitting process in this case is frequently on the other of the error made by reducing the histogram to 20 bins. However, our ability to fit the rehistogrammed result to a sum of Gaussians is very sensitive to the number of bins we have used in the rehistogramming process (equivalently, the bin width). For some numbers of bins, the results converge quickly. For others, they don't.

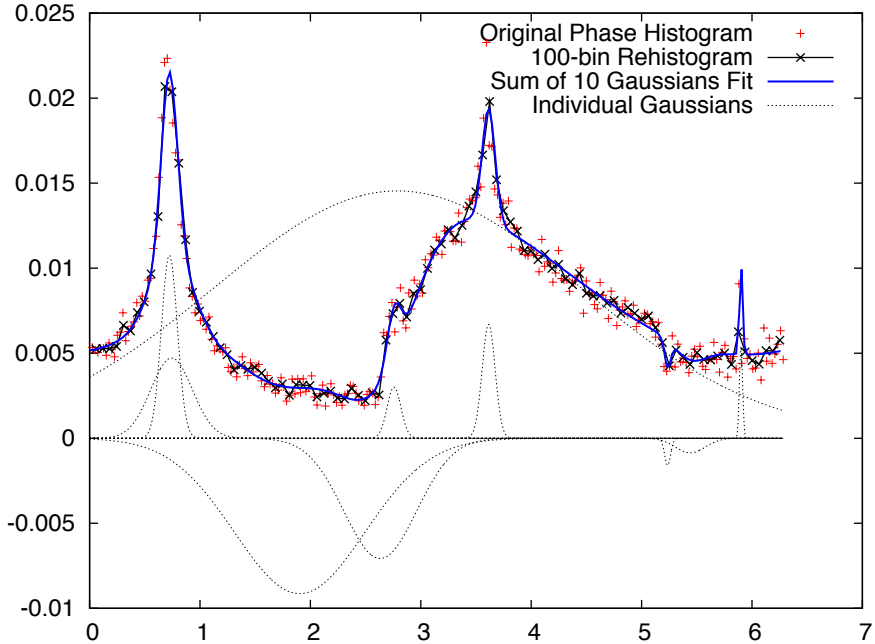


Figure 3.3: Phase histogram and sum-of-Gaussians fit for the quartic oscillator at  $t = 55.0$ , with 100 bins and 10 Gaussians.

Generally speaking, in figure 3.2 we see that adding more Gaussians will eventually improve our result. However, this is not uniformly true, especially if the choice of number of bins is poor. In particular, we note that the change from five Gaussians to six Gaussians leads to worse result for many choices of bin width.

For this problem, it appears that if adding Gaussians leads to little change in the final result, then the result was usually pretty good. The case at 75 bins might be an exception to this, but generally this inspires us to consider this as a criterion to determine whether a given Gaussian fitting is good or not.

We find that 100 bins does the best regardless of the number of Gaussians, and that ten Gaussians does the best regardless of the number of bins for this system. So in figure 3.3, we look more carefully at how we fit that particular result. The red points are the original phase histogram: this corresponds to a vertical slice of figure 3.1(a) at  $t = 55.0$ , where phase is now the dependent variable, and the color scale has been converted to the vertical axis. We note that with the sum of ten Gaussians, we're already starting to fit features which are probably artifacts of the noise remaining in the rehistogram (*e.g.*, the negative peaks near 5.1 and 5.5, as well as the positive peak near 2.8). Overall, the fit matches the rehistogrammed result (and the original phase histogram) very well.

The most useful question for the Gaussian fitting procedure is whether it can be used to estimate the final result using fewer trajectories. All the results discussed to this point are based on fully-converged (100k trajectories) results. In figure 3.2, we show the convergence by

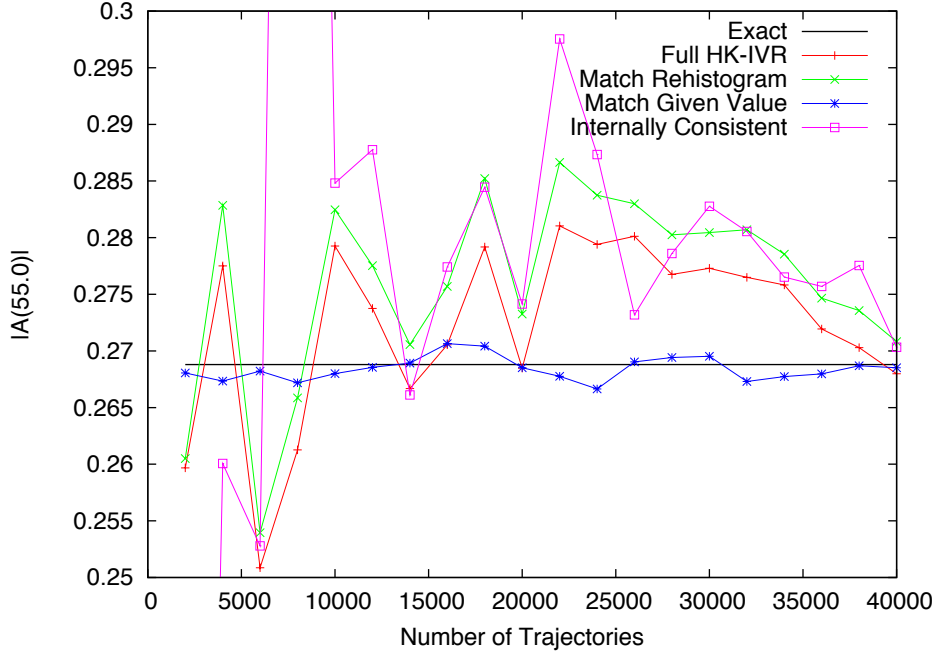


Figure 3.4: Convergence of the phase histogram for the quartic oscillator at  $t = 55.0$  as a function of trajectories for various methods of choosing the “best” number of bins and number of Gaussians for the Gaussian fitting method.

number of trajectories for three methodologies to pick the “best” Gaussian fit. The first method is to give the best match to the rehistogrammed value (which, as shown in figure 3.2, is typically closer to the exact result than the Gaussian fits are). The second method is to choose the best match to a given value — in this case the (known) exact converged HK-IVR result. This is basically cheating, since if we already know the exact converged HK-IVR result we have no need to do this calculation! However, it gives us an idea of the limitation of a hypothetical “perfect” method. Finally, we use a method based on considering the internal consistency. The idea behind this method starts with the observation that the cases where adding more Gaussians had little effect on the final result tended to be situations where we had good fits. For each number of bins, it finds the three consecutive fits with the smallest range in the result, and then these are compared across the numbers of Gaussians. The reported value is the one associated with the middle number of Gaussians from the three fits.

In addition to these three methods, figure 3.4 shows the exact (converged) HK-IVR result, and the full HK-IVR result for each number of trajectories. The only method that beats regular HK-IVR method is the “cheating” method, which matches to the known exact value. Neither of the practical possibilities are more efficient than the full HK-IVR for the same number of trajectories. The internal consistency method is particularly atrocious, making false choices at 2000 and 8000 trajectories. While there may exist a better method for selecting the number of bins and number of Gaussians, clearly, none of these algorithms can be recommended.

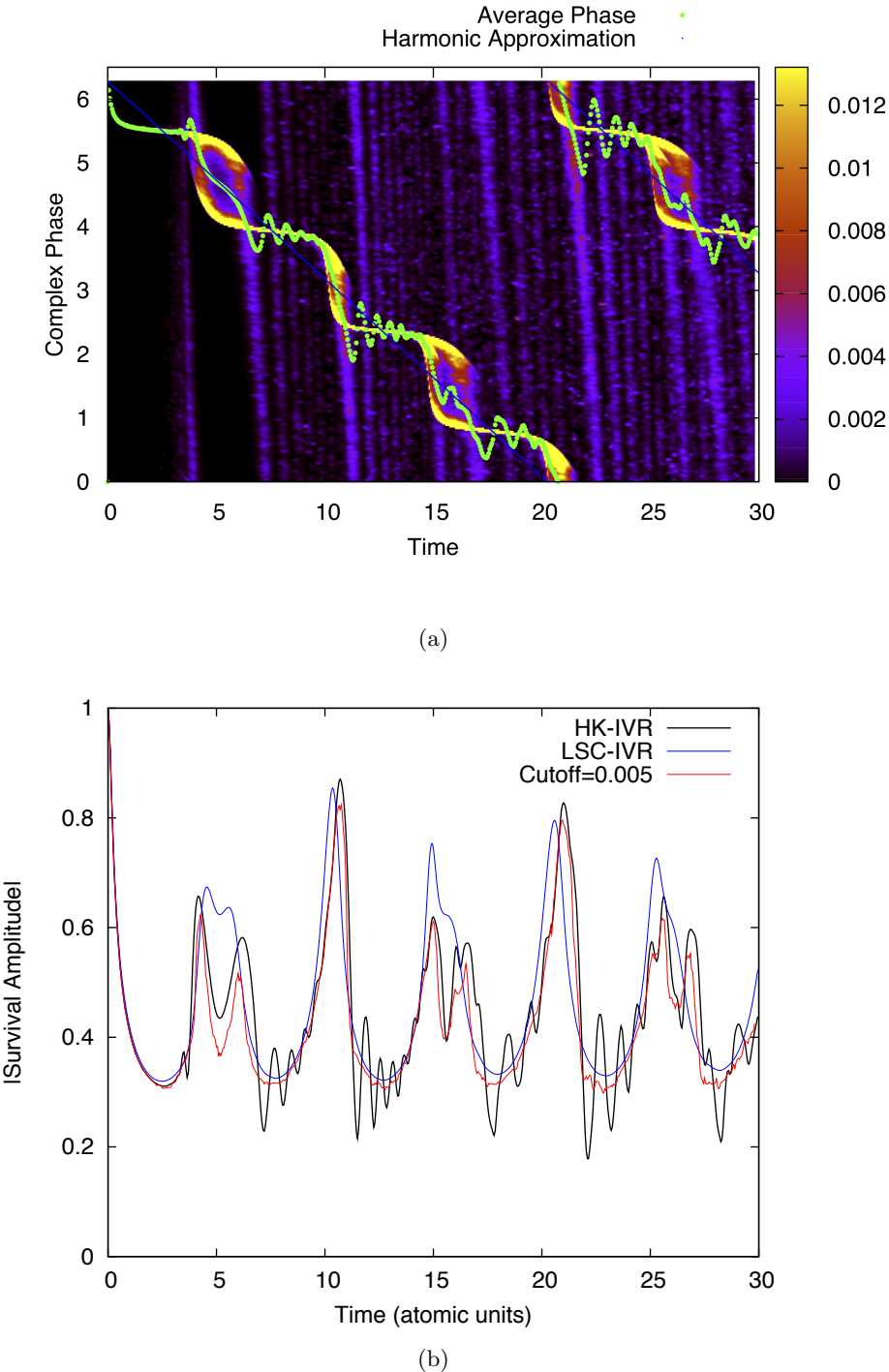


Figure 3.5: Survival amplitude of the anharmonic Morse oscillator system. (a) Phase histogram of the survival amplitude as a function of time. (b) Modulus of the survival amplitude as calculated by the HK-IVR, by the LSC-IVR, and by rebuilding the phase histogram with cutoff 0.005 (normalized to 250 bins).

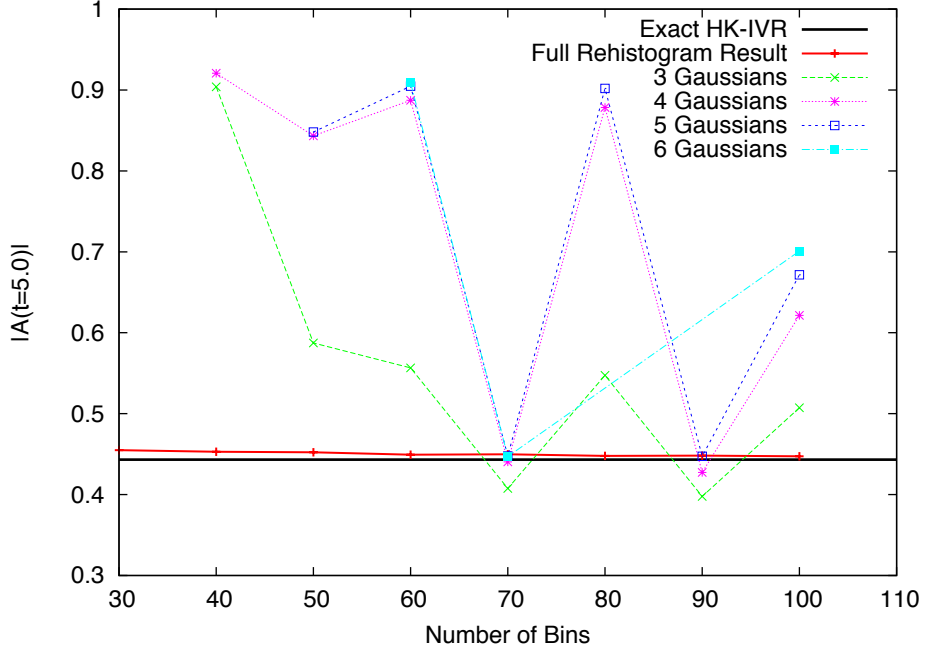


Figure 3.6: Convergence of the Gaussian fit for the anharmonic Morse oscillator at  $t = 5.0$  as a function of the number of rehistogrammed bins, for different numbers of Gaussians. The exact HK-IVR result is shown, as is the rehistogrammed result for each number of bins.

### 3.4 Test System: The Anharmonic Morse Oscillator

Another system we will study is the anharmonic Morse oscillator, which is described in detail in section A.2. The potential energy for this system is given by

$$V(q) = 30.0 \left( 1 + (1 - e^{-0.08q})^2 \right) \quad (3.9)$$

and the initial wavepacket is given in the position representation by

$$\langle q|\psi\rangle = \left( \frac{12}{\pi} \right)^{1/4} e^{-6q^2 + ipq} \quad (3.10)$$

The phase histogram for the survival amplitude of this system (using the HK-IVR) is shown in figure 3.5(a). Again, we see that the harmonic frequency follows the major feature in the phase histogram plot. Overall, this phase histogram is much more sparse than the phase histogram for the quartic oscillator. For this Morse oscillator, we can see that we have significant quantum effects whenever the average phase differs from the brightest features. We note two main types of such features: first, when the bright features bifurcate, as around  $t = 5$ ,  $t = 15$ , and  $t = 25$ . These correspond to the system completing  $n + \frac{1}{2}$  periods ( $n \in \mathbb{N}$ ), and the bifurcation is due to the significant anharmonicity of this potential.\* The other situation where the average

---

\* After completing a full period, this distinction is cancelled out, as is evident at  $t = 10$  and  $t = 20$ .

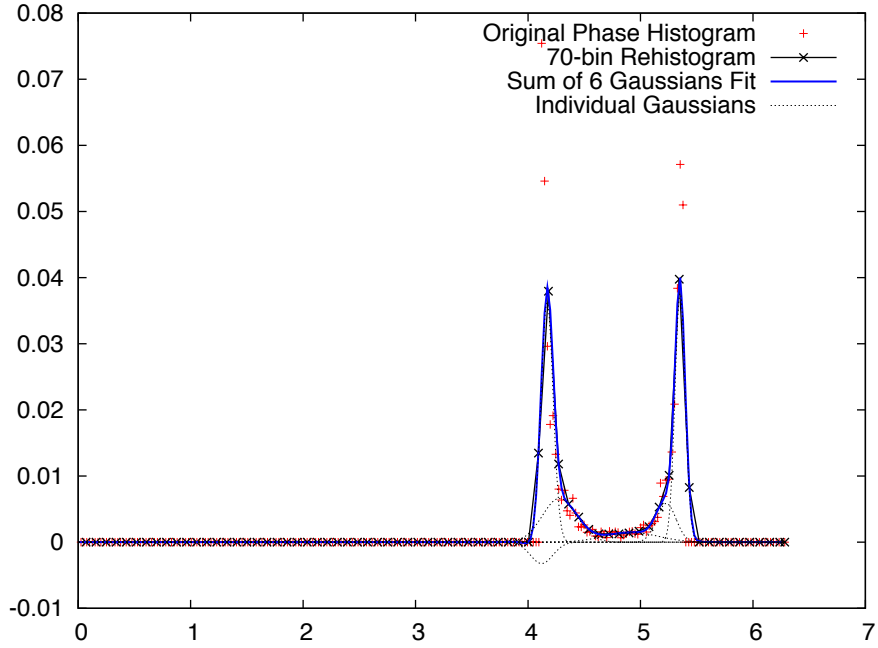


Figure 3.7: Phase histogram and sum-of-Gaussians fit for the anharmonic Morse oscillator at  $t = 5.0$ , with 70 bins and 6 Gaussians.

phase varies significantly from the brightest features are when the average phase is pulled away from the main feature by the highly-sloped low intensity (purple) lines, leading to wiggles in the survival amplitude between the main recurrence peaks as seen in the survival amplitude in figure 3.5(b).

For the first example, we'll look at the phase histogram at  $t = 5.0$ . For the second, we'll look at the phase histogram at  $t = 12.3$ . One important point about this system is that we can see two main features: the first is the bright feature which approximately follows the harmonic frequency. The second is the highly-sloped low intensity (purple) lines. These are much lower in magnitude than the bright feature (which actually goes off the scale of the numbers in figure 3.5(a)). This secondary feature is interesting: what looks at a casual glance like several lines is actually a single line corkscrewing around the bright feature in the  $2\pi$ -periodic phase domain.

In figure 3.5(b), we note that neither type of quantum effect is captured by the LSC-IVR. The first type of effect leads to a deeper drop between the peaks around  $t = 5$ , and further structure in the double peaks around  $t = 15$  and  $t = 25$ . None of this is captured by the LSC-IVR. The second type of quantum effect is also notably absent from the LSC-IVR calculation. In figure 3.5(b) there is also a third line, corresponding to only including phases that contribute at least 0.005 (based on histogramming the phases into 250 bins). This effectively removes the purple from figure 3.5(a), and, as we see, it recovers the first kind of effect, but not the second. If we compare this with the results from section A.2, we note that qualitatively, this cutoff approximation has a lot in common with the result we get by turning off the action (see figure A.3(b)). Both are

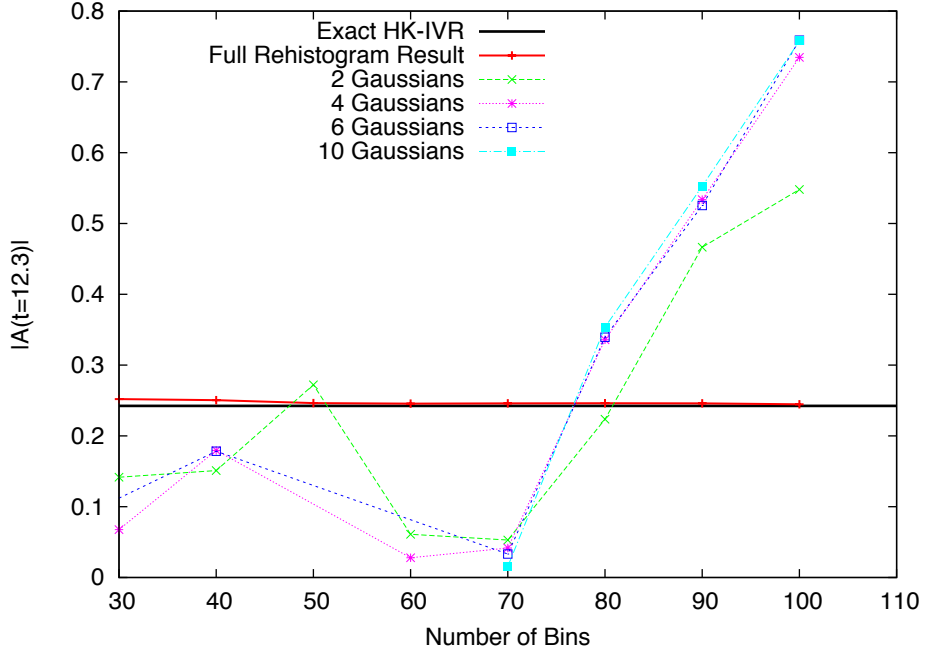


Figure 3.8: Convergence of the Gaussian fit for the anharmonic Morse oscillator at  $t = 12.3$  as a function of the number of rehistogrammed bins, for different numbers of Gaussians. The exact HK-IVR result is shown, as is the rehistogrammed result for each number of bins.

able to capture the deep dip around  $t = 5$  (which we do not capture if we turn off the prefactor, as shown in figure A.3(a)), but are unable to capture the wiggles between the recurrences. The cutoff method is notably more quantitative in its agreement with the original, but this still leads us to suggest that the low intensity lines from the phase histogram result from the action.

In figure 3.6, we see how different numbers of bins and different numbers of Gaussians affect the accuracy of the result from fitting the phase histogram at  $t = 5.0$ . In this case, we see that we have some numbers of bins that have very good results (70, 90) but most of them are very bad, to the point of giving meaningless numbers. With the exception of the “good” bin choices, results are actually made worse by using more than three Gaussians.

To see how a good fit works for this phase histogram, we choose the case of 70 bins and six Gaussians, shown in figure 3.7. The phase histogram is very simple: most features could clearly be reproduced with four Gaussians (one for each peak, and one each to correct the asymmetric tails). Yet, for some numbers of bins, the calculation fails completely.

Figure 3.8 shows the result of trying to fit the phase histogram of the anharmonic Morse oscillator at  $t = 12.3$  with different numbers of rehistogramming bins and different numbers of Gaussians. The result is an abject failure. Fitting to two Gaussians does best; adding more makes it worse. We have bad results for all numbers of bins, verging toward atrocious. Of greatest concern is that we find that we obtain very consistent results as we add more Gaussians at many numbers of bins — very consistent results, and very wrong results.

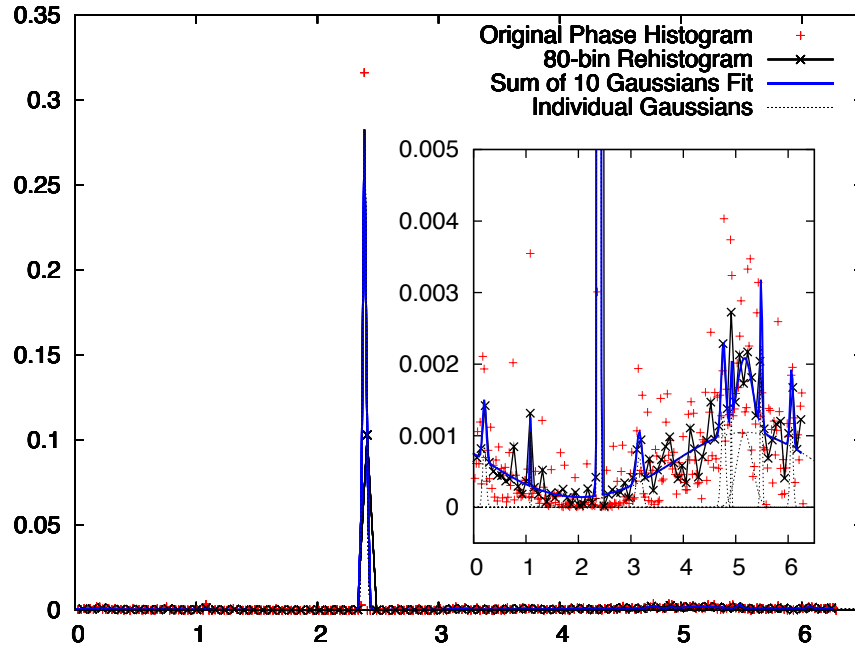


Figure 3.9: Phase histogram and sum-of-Gaussians fit for the anharmonic Morse oscillator at  $t = 12.3$ , with 80 bins and 10 Gaussians.

To try to understand why this fails, we look more closely at the fit with 80 bins and 10 Gaussians. The phase histogram at this time shows the two main features discussed in the time-dependent phase histogram in figure 3.5(a): the “bright” feature, which here is a very large, very thin peak near a phase of 2.4, and the low intensity “purple” feature, which is a broad peak centered near a phase of 5.1 (shown in the inset to figure 3.9). This short, broad feature has a peak that is an order of magnitude shorter than the peak of the bright feature, but the relative widths and relative phases mean that they are both able to contribute to the final result.

From figure 3.9, we know that we capture most of the features of the re-histogrammed result, although the original histogram is very noisy. Since the rehistogrammed results do reasonably well according to figure 3.8, we assume that it is not necessary to capture the noise exactly. Most likely, the Gaussian fit is unable to accurately capture the result for this phase histogram because the two main features are so different. A small error in the total width of the broad peak may lead to a substantial error in the calculation. In all the other examples we have seen, the features involved were of similar scales. It is the scale mismatch that leads to the complete failure for this example.

### 3.5 Discussion and Future Directions

Although we have not found a way to use the phase histogram idea to make semiclassical calculations more efficient, it still gives us a way to learn more about semiclassical methods and the way they capture quantum effects. In particular, we note the features in the time dependent phase histogram which nearly follow the harmonic approximation (and are probably the result of the prefactor) and the results which we showed (for the anharmonic Morse oscillator) result from the interference of action terms.

The fitting process obviously has problems: it doesn't work for all systems, and even when it does work, we don't have a good way to select the right number of bins and number of Gaussians to get the best fit. The particularly difficult problem to automate is to determine the appropriate bin width. The fitting procedure can be very sensitive to the number of bins.

Although we have automated the guessing procedure, it is quite possible that another procedure would be more efficient, or that different guessing algorithms would be better suited for different specific fits. The Levenberg-Marquardt algorithm is known to be very sensitive to the initial guess, so there's no guarantee that our results would be robust with respect to different guessing methodologies. All of these provide potential avenues for improvement.

## Chapter 4

# The Precision Finite Difference Monodromy Matrix

Most methods involving the semiclassical IVR also involve a prefactor, which is generally the square root of the determinant of an  $F \times F$  matrix, where  $F$  is the number of degrees of freedom. The matrix used in the prefactor involves the blocks of the monodromy matrix.

As was seen in section 1.1, the prefactor can be viewed as the result of quantum paths near the classical paths, or as it is often said, as quantum fluctuations about the classical path. The prefactor is one of the things that sets semiclassical theory apart from purely classical methods, and so we expect it to be important for capturing quantum effects.

However, calculating the prefactor is one of the most difficult problems in the semiclassical IVR, as the Hessian can be a very expensive calculation in complex systems. Further, the matrix multiplications required at each step have computational scaling on the order of  $F^3$  (which must then be multiplied by the number of time steps).

In this chapter we present a new method for calculating the monodromy matrix which requires neither the Hessian nor the matrix multiplications of other methods. We will first review several previous efforts to simplify the calculation of the prefactor, including a previous method to avoid the Hessian. Then we will introduce our method, dubbed the precision finite difference method, and finally we will compare the results of our technique to the other methods.

### 4.1 Older Methods

The most commonly used method to calculate the monodromy matrix, which requires second derivatives of the Hamiltonian (notably, the Hessian) and involves matrix multiplication in order to determine the time derivative of the monodromy matrix, is described in section 1.1.3. The most relevant equation, previously equation (1.84), is repeated below:

$$\begin{pmatrix} \dot{M}_{qq} & \dot{M}_{qp} \\ \dot{M}_{pq} & \dot{M}_{pp} \end{pmatrix} = \begin{pmatrix} H_{pq} & H_{pp} \\ -H_{qq} & -H_{qp} \end{pmatrix} \begin{pmatrix} M_{qq} & M_{qp} \\ M_{pq} & M_{pp} \end{pmatrix} \quad (4.1)$$

with  $(H_{\alpha\beta})_{ij} \equiv \frac{\partial^2 H}{\partial \alpha_i \partial \beta_j}$ , where  $H$  is the Hamiltonian. In many cases, equation (4.1) can be simplified by noting that, for a Hamiltonian  $H(p, q) = T(p) + V(q)$ , the terms  $H_{pq} = H_{qp} = 0$ .

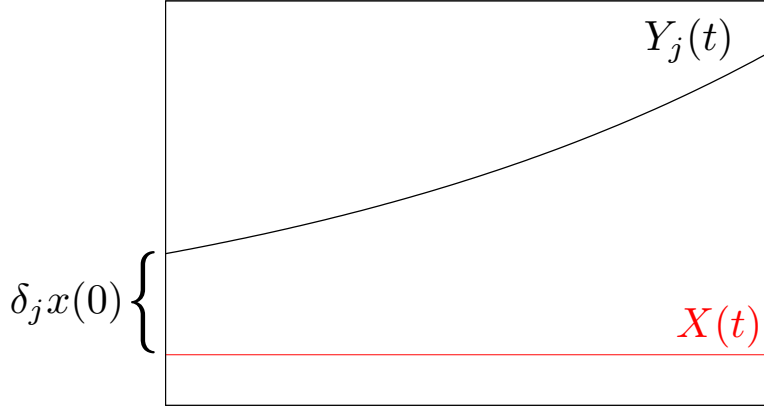


Figure 4.1: Cartoon of the naïve finite difference method for calculating the monodromy matrix.

The derivation of this method was outlined in section 1.1.3.

Most work in this thesis involves situations where we have an analytical form of the Hessian. However, in the general case, we need to determine the Hessian by finite difference on the forces. If the force at point  $q$  is given by  $F(q)$ , the matrix elements of the Hessian  $H_{qq}$  are given by:

$$(H_{qq})_{ij} = \frac{F(q + \Delta q_j)_i - F(q)_i}{\Delta q_j} \quad (4.2)$$

where  $\Delta q_j$  is a small displacement in the  $j$ th element of the position, and  $F(q)_i$  is the  $i$ th element of the force vector. We will use this when discussing the computational cost of this method.

#### 4.1.1 Naïve Finite Difference

The most obvious method to calculate the monodromy matrix is by finite difference. Our expectation is that it would fail, because one would assume that (at least, at long time) chaotic behavior of the system would mean that a finite change in initial conditions is, quite simply, too large to accurately represent the infinitesimal change which defines the derivative. However, this method would have the advantage over the standard method of not requiring the calculation of the Hessian. To my knowledge, a simple finite difference method had not been previously explored in the literature on the SC-IVR.

However, we have tried it as a part of our work below, and found that it worked far better than expected. We found that it works quite well even for unstable trajectories in the Hénon-Heiles potential — it only failed at long time when the initial displacements were made orders of magnitude larger than necessary.

The procedure for this method is quite straightforward. For each set of initial conditions from our IVR, we propagate  $2F + 1$  trajectories: the central trajectory plus a trajectory corresponding to a small change in each initial condition. We will refer to the  $2F$ -dimensional

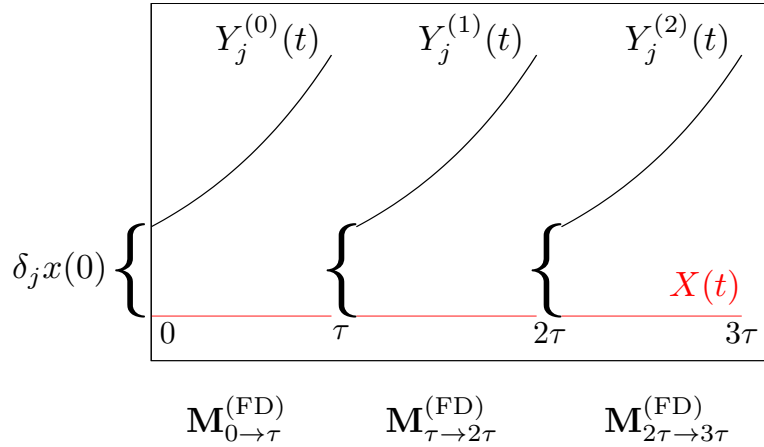


Figure 4.2: Cartoon of Garashchuk and Light’s method for calculating the monodromy matrix.

phase space vector for the central trajectory as  $X(t)$ , and the auxiliary trajectory for phase space dimension  $j$  will be labeled as  $Y_j(t)$ .

The (naïve) finite difference monodromy matrix is then:

$$M_{ij}^{(FD)}(t) = \frac{(Y_j(t) - X(t))_i}{\delta_j x(0)} \quad (4.3)$$

where  $\delta_j x(0) \equiv (Y_j(0) - X(0))_j$ . The subscripts outside the parentheses indicate an element of the vector within the parentheses.

An illustration of the naïve finite difference method for calculating the monodromy matrix is shown in figure 4.1. The red line at the bottom represents the original trajectory  $X(t)$ , and the black line diverging from it is an auxiliary trajectory  $Y_j(t)$ . The initial distance between these,  $\delta_j x(0)$ , is what is used for the finite difference.

#### 4.1.2 Garashchuk and Light’s Finite Difference Method

Garashchuk and Light presented a different kind of finite difference method to calculate the monodromy matrix elements without requiring the Hessian.<sup>53</sup> The key insight that led to their method is the fact that the monodromy matrix is unitary. As a result, the monodromy matrix  $\mathbf{M}(t_2, t_0)$  which describes evolution from time  $t_0$  to time  $t_2$  can be described as the product of matrices connecting intermediate times, *e.g.*:

$$\mathbf{M}_{t_0 \rightarrow t_2} = \mathbf{M}_{t_1 \rightarrow t_2} \mathbf{M}_{t_0 \rightarrow t_1} \quad (4.4)$$

This is easily verified by writing the phase space variables as nested functions of the internal times (such as  $q_{t_2}(q_{t_1}(q_{t_0}, p_{t_0}), p_{t_1}(q_{t_0}, p_{t_0}))$ ) and taking the appropriate derivatives using the chain rule.

The technique proposed by Garashchuk and Light is then to simply make a short-time finite difference approximation to the monodromy matrix between simulation timesteps, and to

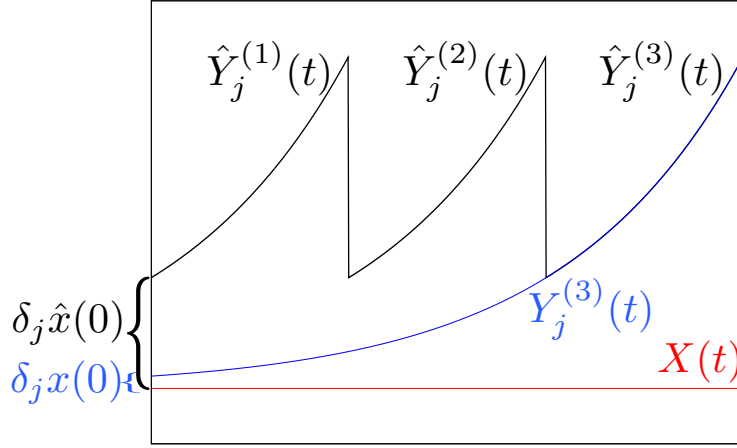


Figure 4.3: Cartoon of the precision finite difference method for calculating the monodromy matrix.

multiply the resulting matrices together in order to obtain the monodromy matrix for longer times. Mathematically, we have (for some  $\delta t$ ):

$$\mathbf{M}^{(\text{GL})}(t) = \mathbf{M}_{t-\delta t \rightarrow t}^{(\text{FD})} \mathbf{M}_{t-2\delta t \rightarrow t-\delta t}^{(\text{FD})} \cdots \mathbf{M}_{0 \rightarrow \delta t}^{(\text{FD})} \quad (4.5)$$

where  $\mathbf{M}^{(\text{FD})}(t_2, t_1)$  is the finite difference prefactor from equation (4.3), replacing time  $t$  with  $t_2$  and time 0 with  $t_1$ .

In figure 4.2 we have a cartoon of Garashchuk and Light’s method for calculating the monodromy matrix. It consists of several disconnected naïve finite difference monodromy calculations, which are then multiplied together to obtain the total monodromy matrix.

## 4.2 The Precision Finite Difference Method

My new method for calculating the monodromy matrix, called the precision finite difference (PFD) method, is based on the “precision shooting” method of Grünwald, Dellago, and Geissler.<sup>54</sup> Precision shooting was designed in the context of transition path sampling, where it was used to keep a new trajectory near a trajectory known to be reactive for a longer time.

The mathematical concept behind both of these “precision difference” methods is the linearization of the dynamics of small perturbations. To describe this, we will use the notation from section 4.1.1, where  $X(t)$  and  $Y_j(t)$  are two trajectories which start very close to each other. We will define the quantity  $\delta_j x(t) \equiv Y_j(t) - X(t)$ , so that  $Y_j(t) = X(t) + \delta_j x(t)$ .

We define the solution operator  $\Phi_{\Delta t}$  as the operator which takes a system in state  $Z(t)$  and propagates it in time to make the system  $Z(t + \Delta t)$ . We can write the displacement  $\delta_j x(t)$  in terms of the solution operator:

$$\delta_j x(t) = Y_j(t) - X(t) = \Phi_t(X(0) + \delta_j x(0)) - \Phi_t(X(0)) \quad (4.6)$$

Now we make the linearization approximation. We expand the solution operator about  $X(0)$ , assuming that the displacement  $\delta_j x(0)$  is small:

$$\Phi_t(X(0) + \delta_j x(0)) - \Phi_t(X(0)) \approx \frac{\partial \Phi_t(X(0))}{\partial X(0)} \delta_j x(0) \quad (4.7)$$

For small displacements and short times, this approximation will hold.

The trick developed by Grünwald *et al.* is based on the fact that what holds for one displacement in the linear regime will hold for another such displacement. Suppose that the displacement  $\delta_j x(0)$  discussed above is well below the threshold of the linear regime. There will be a larger displacement,  $\delta_j \hat{x}(0) = c_0 \delta_j x(0)$  (with  $c_0 > 1$ ) corresponding to the start of another trajectory,  $\hat{Y}_j(t)$ , also still within the linear regime. The same analysis would lead us to see that

$$\delta_j \hat{x}(t) \approx \frac{\partial \Phi_t(X(0))}{\partial X(0)} \delta_j \hat{x}(0) \quad (4.8)$$

$$\approx \frac{\partial \Phi_t(X(0))}{\partial X(0)} c_0 \delta_j x(0) \quad (4.9)$$

$$\approx c_0 \delta_j x(t) \quad (4.10)$$

Within the linear regime, the constant of proportionality between the two trajectories remains unchanged.

What this means is that we can use a larger displacement (but still within the linear regime) as a proxy for a smaller displacement — possibly so small that the displacement falls below machine precision. The method developed as “precision shooting” and adopted here to calculate the monodromy matrix elements uses successive trajectories in the linear regime to rescale to a very small initial displacement. The proxy trajectory  $\hat{Y}_j^{(k)}(t)$  (where the superscript  $(k)$  is a label on the number of times the displacement has been rescaled) starts some initial distance  $\sigma$  in phase space from the known trajectory  $X(t)$ . After some number of steps  $\tau$  (but while  $\hat{Y}_j$  is still within the linear regime) the trajectory is rescaled again have a norm of  $\sigma$  within phase space. The rescaling factor is  $c_j^{(k)} \equiv |\delta_j \hat{x}^{(k)}(k\tau)| / |\delta_j \hat{x}^{(k)}((k-1)\tau)|$ . The initial displacement is similarly rescaled so that  $\delta_j x^{(k)}(0) = \frac{\delta_j \hat{x}^{(k)}(0)}{\prod_{n=0}^k c_j^{(n)}}$ . At any time, we can calculate the monodromy matrix by finite difference using equation (4.3), with the current proxy trajectory  $\hat{Y}_j^{(k)}(t)$  in the numerator and the rescaled initial displacement  $\delta_j x^{(k)}$  in the denominator. This idea is illustrated in figure 4.3. Like Garashchuk and Light’s method, the precision finite difference method involves a sort of “restarting” of the trajectory. But whereas Garashchuk and Light’s auxiliary trajectory is restarted without reference to the previous state, the precision finite different method actually rescales the previous state. In essence, this trick can be seen as keeping information that allows us to avoid the matrix multiplications that Garashchuk and Light have to do.

A flowchart for the precision finite difference algorithm is shown in figure 4.4.

### 4.3 Comparison of Methods for Simple Potentials

In this section, we will look at two simple systems in order to test the precision finite difference method. First we use a simple one-dimensional system in order to confirm that the

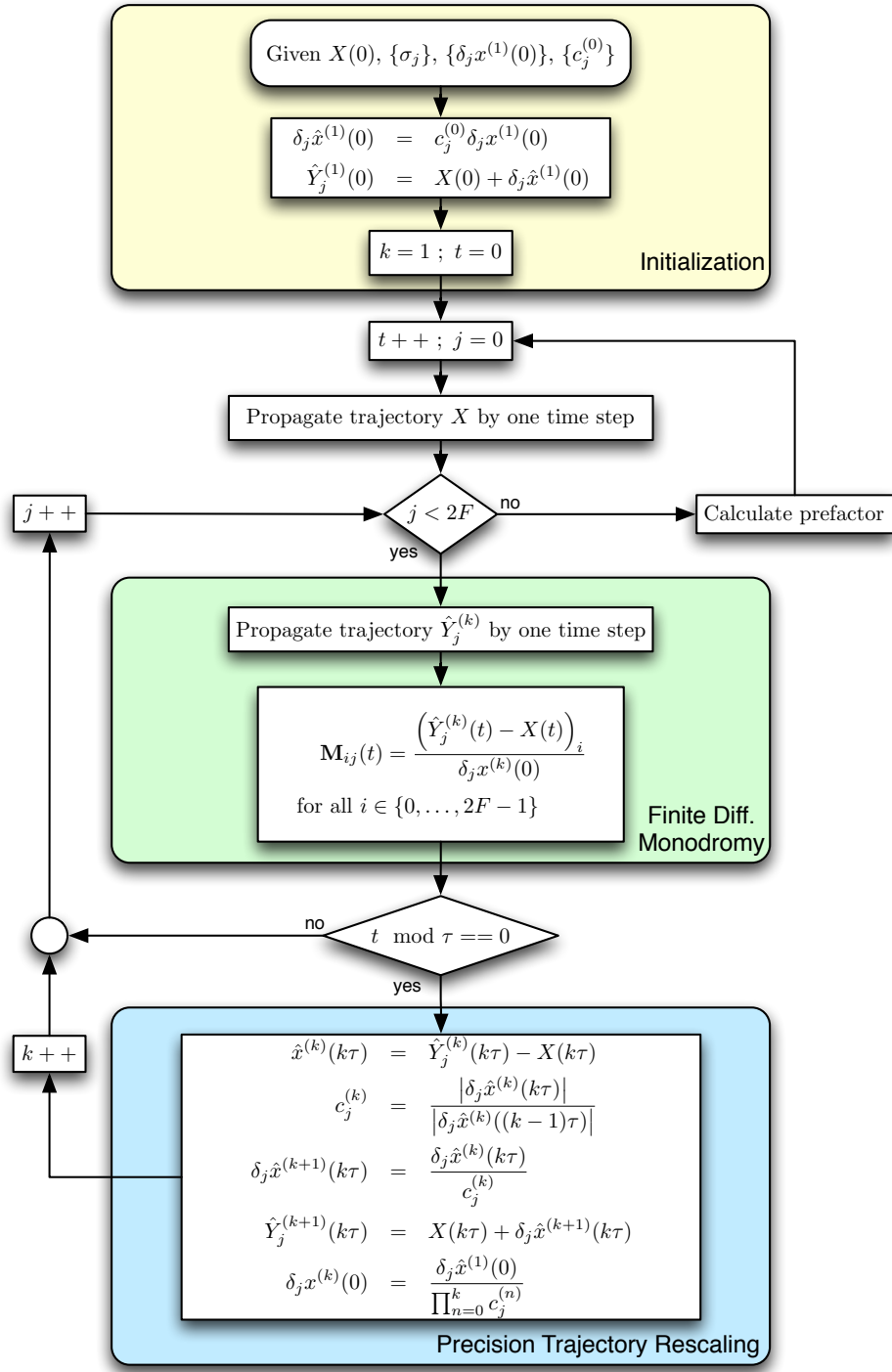


Figure 4.4: Flowchart for the precision finite difference algorithm.

Standard Method, Finite Difference Hessian	$F \mathcal{O}(\text{force}) + F^3$
Garaschuk and Light's Finite Difference Method	$F \mathcal{O}(\text{force}) + F^3$
Naïve Finite Difference Method	$F \mathcal{O}(\text{force}) + F^2$
Precision Finite Difference Method	$F \mathcal{O}(\text{force}) + F^2$

Table 4.1: Computational complexity of various methods for calculating the monodromy matrix, assuming the force calculation is a “black box.” The number of degrees of freedom in the system is denoted by  $F$ .

methodology works at all. Since the expected advantage of the precision finite difference method over the naïve finite difference method is that it should work better for chaotic systems, we then explore a two-dimensional system which is known to exhibit chaos.

### 4.3.1 One-Dimensional Potentials

An energy-conserving, one-dimensional potential cannot exhibit Lyapunov instability.\* Therefore, we can use such systems to compare the accuracy of the methods in the absence of chaos. As a first system to test, we'll look at an anharmonic Morse potential. This system is described in greater detail in section A.2. It has the potential energy

$$V(q) = 30.0 \left( 1 + (1 - e^{-0.08q})^2 \right) \quad (4.11)$$

with initial wavepacket (in the position representation):

$$\langle q | \psi \rangle = \left( \frac{12}{\pi} \right)^{1/4} e^{-6q^2 + ipq} \quad (4.12)$$

In figure 4.5(a), we see the survival amplitude calculated using the HK-IVR, with each of these methods to calculate the monodromy matrix. For all three finite difference methods, the finite difference displacement is set to  $10^{-5}$  for both position and momentum. For the precision finite difference method, we rescale every 50 steps. The results are indistinguishable.

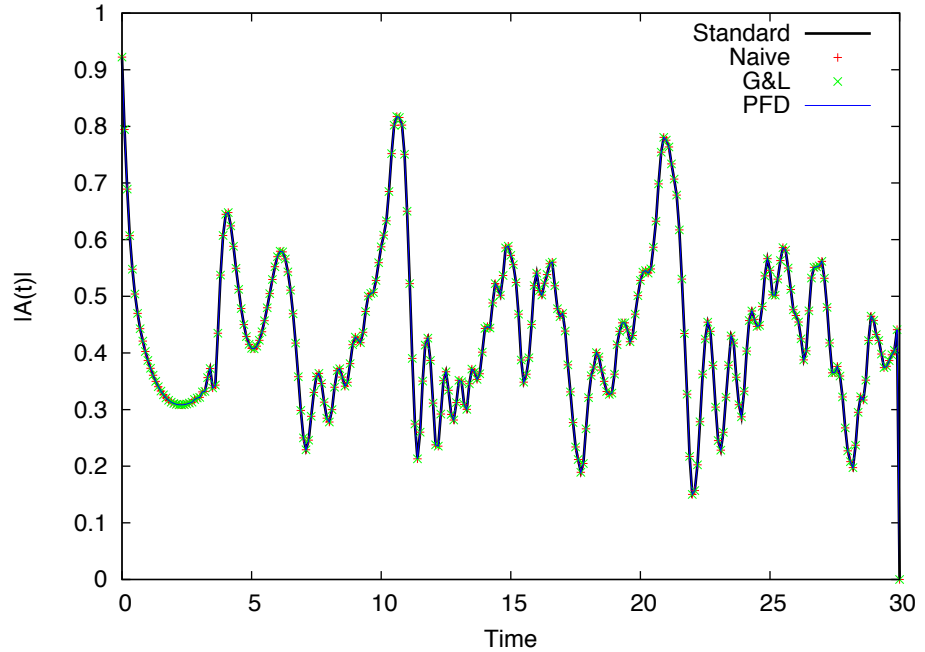
To take a closer look at how these methods perform, we'll use the magnitude of the Herman-Kluk prefactor

$$C_t^{\text{HK}} = \det \left( \frac{1}{2} \left( \frac{\partial q_t}{\partial q_0} + \frac{\partial p_t}{\partial p_0} + i\gamma \frac{\partial p_t}{\partial q_0} + \frac{1}{i\gamma} \frac{\partial q_t}{\partial p_0} \right) \right)^{1/2} \quad (4.13)$$

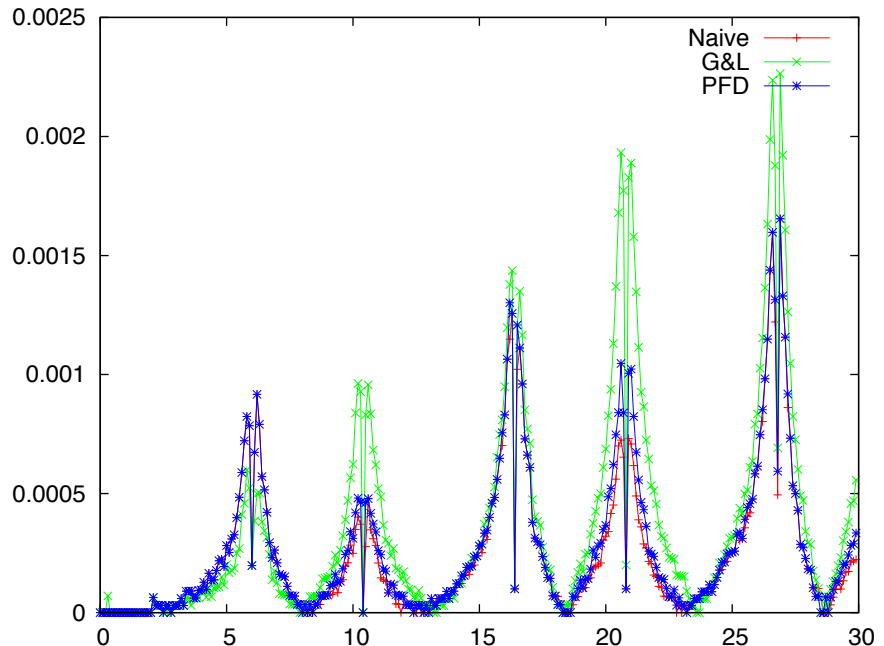
This gives us a single number to observe (instead of the  $4F^2$  monodromy matrix elements), and also happens to be the number that is most important to us for practical purposes. Figure 4.5(b) shows the percent error (compared to the standard method) for the modulus of the Herman-Kluk prefactor for a trajectory with initial conditions  $(q_0, p_0) = (0.0, 1.0)$ . The largest errors up to this time are on the order of 0.002%. The magnitude of the prefactor is around 1–3, so this error, after 100 timesteps, the error is up to about  $6 \times 10^{-5}$ . Since the original displacement is just  $10^{-5}$ , so essentially all the error can be attributed to the finite difference approximation. Further, all the methods show essentially similar amounts of error.

---

\* This is consequence of the Poincaré-Bendixson theorem.



(a) Full survival amplitude. The results are indistinguishable



(b) Percent error in the magnitude of the Herman-Kluk prefactor (compared to the standard method) for the naive, Garashchuk and Light (G&L) and precision finite difference (PFD) methods for a trajectory starting at  $q = 0.0$ ,  $p = 1.0$ .

Figure 4.5: Tests for the one-dimensional anharmonic Morse oscillator.

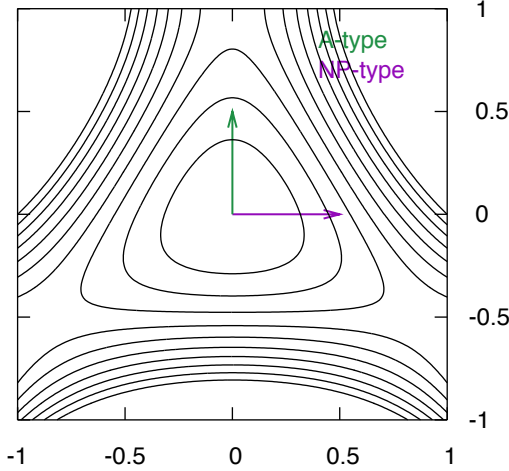


Figure 4.6: The Hénon-Heiles Potential. The arrows show the initial directions of the A-type and NP-type trajectories.

Label	$x_1(0)$	$x_2(0)$	$p_1(0)$	$p_2(0)$
A1	0.0	0.0	0.0	0.1
A2	0.0	0.0	0.0	0.4
NP1	0.0	0.0	0.1	0.0
NP2	0.0	0.0	0.4	0.0

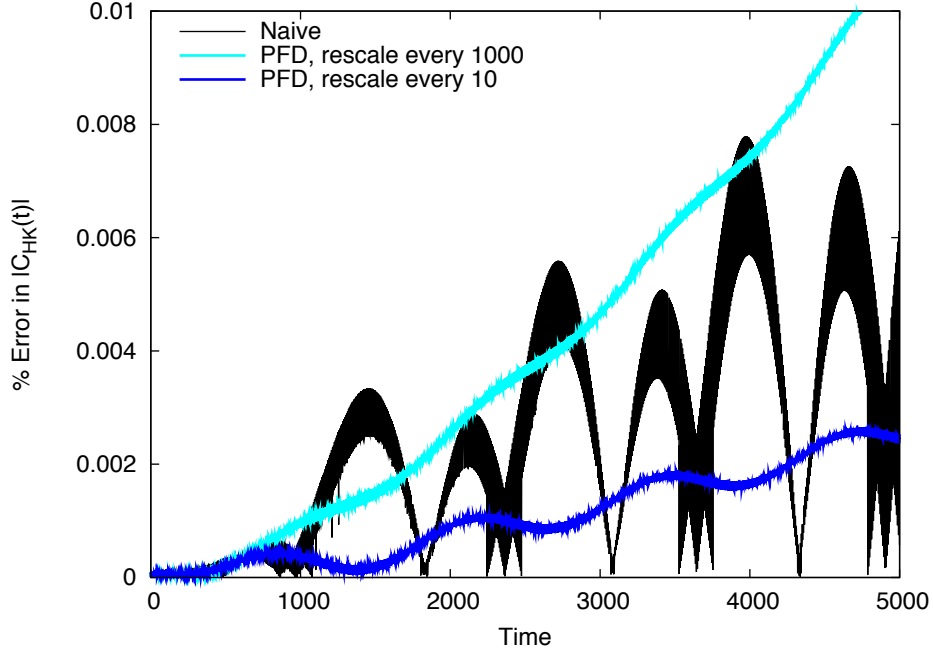
Table 4.2: Initial conditions for trajectories on the Hénon-Heiles potential.

### 4.3.2 A Chaotic Two-Dimensional Test: The Hénon-Heiles Potential

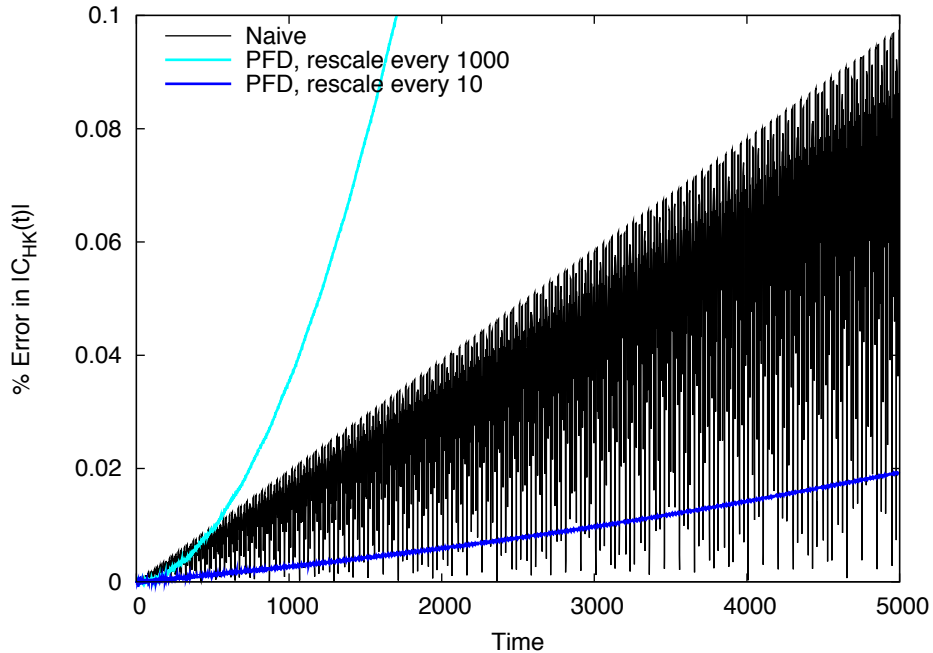
The main reason that we expect the naïve finite difference method to eventually fail is that we expect trajectories in realistic molecular dynamics simulations to exhibit Lyapunov instability. That can't occur in one dimension. In order to test the performance of these methods on unstable trajectories, we use the Hénon-Heiles potential,<sup>55</sup> which is one of the classic examples of a nonintegrable system. The Hamiltonian for the generalized Hénon-Heiles potential is:

$$H(x_1, x_2, p_1, p_2) = \frac{1}{2} (p_1^2 + p_2^2 + \omega_1^2 x_1^2 + \omega_2^2 x_2^2) + \alpha x_1^2 x_2 + \beta x_2^3 \quad (4.14)$$

We use the parameters of the original Hénon-Heiles system:  $\omega_1 = \omega_2 = 1.0$ ,  $\alpha = 1.0$ ,  $\beta = -1/3$ . The potential is illustrated in figure 4.6. It is a  $C_3$ -symmetric surface with a basin centered around the origin and a barrier with escape energy  $1/6$ . All of the trajectories considered here are classically bounded.



(a) Percent error in the HK prefactor for the low-energy trajectory NP1 ( $E = 0.01$ ).



(b) Percent error in the HK prefactor for the high-energy trajectory NP2 ( $E = 0.16$ ).

Figure 4.7: Percent error in the magnitude of the Herman-Kluk prefactor for the NP-type trajectories from the Hénon-Heiles potential, comparing the precision finite difference method to the naïve method.

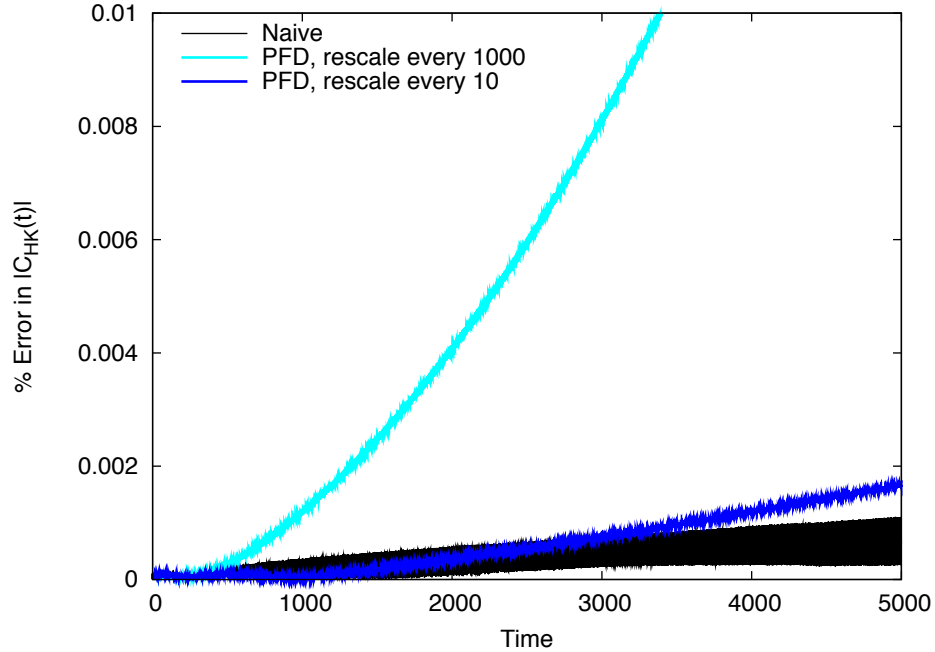
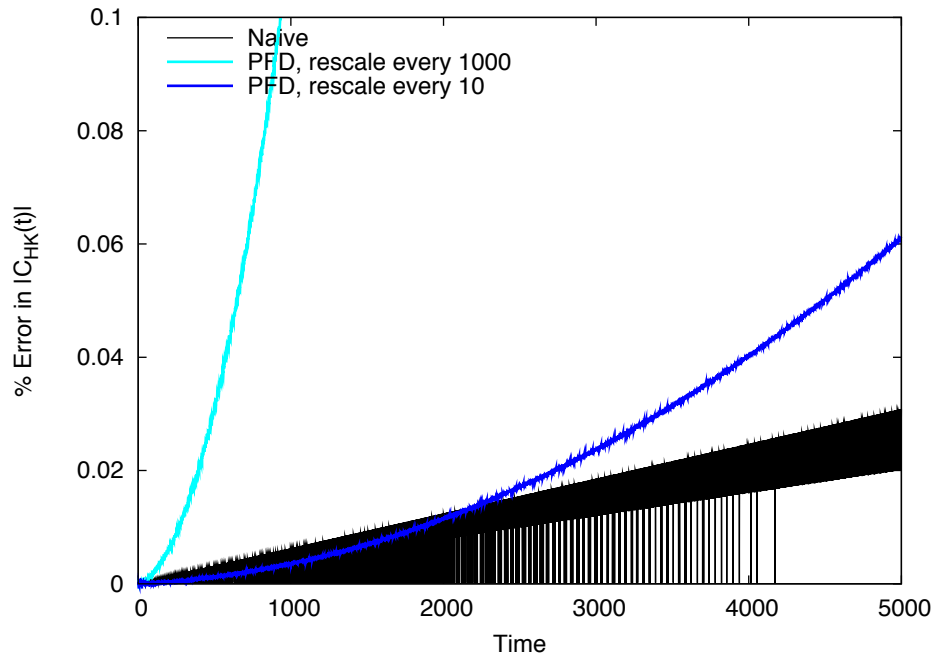
(a) Percent error in the HK prefactor for the low-energy trajectory A1 ( $E = 0.01$ ).(b) Percent error in the HK prefactor for the high-energy trajectory A2 ( $E = 0.16$ ).

Figure 4.8: Percent error in the magnitude of the Herman-Kluk prefactor for the A-type trajectories from the Hénon-Heiles potential, comparing the precision finite difference method to the naïve method.

We use stable (low energy) and unstable (high energy) members of the “A” family of periodic trajectories as described in reference 56, as well as low energy and high energy nonperiodic trajectories of various (classically bound) energies. Initial conditions are given in table 4.2. The high energy trajectories, with  $E = 0.16$ , are near the dissociation limit of  $E = 1/6$ . The low energy trajectories have  $E = 0.01$ .

In figures 4.7 and 4.8, we show percent error in the Herman-Kluk prefactor for each trajectory.<sup>†</sup> Each figure shows the error (as compared to the standard method) in the naïve finite difference method in black, and two rescaling frequencies of the precision finite difference method. In dark blue, we rescale every 10 steps (each step being 0.004 time units). In light blue, we rescale every 1000 steps. Both the naïve finite difference and precision finite difference have initial displacements of  $10^{-6}$  for the auxiliary trajectories in both position and momentum space.

For both figures, the first observation to make is that the error in the prefactor is surprisingly small, even for the naïve finite difference method. The calculation goes all the way to  $t = 5000$ , which is  $1.25 \times 10^6$  timesteps, and the worst errors (in the high-energy trajectories) are on the order of 0.1%. Furthermore, we still see linear growth in the error in the naïve prefactor (which may indicate that these trajectories are not sufficiently chaotic to show the exponential divergence in the error).

Figure 4.7 shows the results for the nonperiodic trajectories. We expect this behavior to be typical of the system, since the nonperiodic trajectories are (by definition) ergodic, and a trajectory selected at random is extremely unlikely to be periodic. In figure 4.7(a), we see the results from the low energy trajectory. Rescaling every 1000 steps begins to get much worse than the naïve method, indicating that after 1000 steps we are no longer in the linear regime, so the precision finite difference approximation is no longer valid. However, if we rescale every 10 steps, the precision finite difference method is, on average, better than the naïve finite difference. The same statements are true, but amplified, at high energy, as shown in figure 4.7(b). Rescaling every 1000 steps fails quickly and exponentially, while rescaling every 10 steps stays well under the typical error for the naïve finite difference method (although it looks like it may be curving upward at very long times, possibly moving into an exponential regime).

In figure 4.8, we explore the same issues as applied to the A-type periodic trajectories. Here we see different behavior. Rescaling every 1000 trajectories fails even more miserably, showing that this rescaling frequency takes us well outside the linear regime. However, in this case, even rescaling every 10 steps fails to improve the naïve result at long time (although it is as good or better up to a time on the order of  $t = 2000$ , which corresponds to  $5 \times 10^5$  timesteps). As with figure 4.7, both energies show the same qualitative behavior, although it is more pronounced at higher energies. This may be a specific result of the periodic trajectory, although the reason the periodic trajectory would suffer from this is unclear.

It is possible that the integrator is accumulating error at long times, since we go to over a million timesteps. However, we use a good fourth-order symplectic integrator.<sup>57</sup> Further, if this were the problem, we would expect to see it in the naïve finite difference calculation as well.

---

<sup>†</sup> Technically, what we show is the local maxima of the error. As can be seen from figure 4.5(b), the error oscillates. In order to make the plots readable, we only show the local maxima.

## 4.4 Discussion and Future Directions

One of the most surprising conclusions from this work is that the naïve finite difference method is much more robust than one might expect. The precision finite difference method, which can be seen as a layer on top of the naïve method, does improve the naïve results for the nonperiodic trajectories and for the periodic trajectories at relatively short times. The “short” times here, which reach to hundreds of thousands of timesteps, are actually quite long by the standards of SC-IVR calculations. Therefore, we believe that the precision finite difference method might be a practical way to calculate the monodromy matrix.

If the precision finite difference method is practical (*i.e.*, if it approximately obtains the correct answer), then it will be slightly faster than either the standard method or Garashchuk and Light’s method. It can’t reduce the leading term in the calculation cost (the calculation of the auxiliary trajectories, or, equivalently, the calculation of the Hessian), but the second term, which deals with how that information is used to generate the monodromy matrix, is faster than these methods.

However, it is not faster than the naïve finite difference, so the question then becomes whether the precision finite difference method is more accurate than the naïve finite difference. We have shown that it is more accurate up to reasonable times for the trajectories we explored, although the accuracy of the naïve finite difference method may be sufficient. Nevertheless, it is possible that the precision finite difference will hit a sweet spot in the trade-off between accuracy and speed, being faster than the standard method or Garashchuk and Light’s method, and more accurate than the naïve finite difference method.

There are still a few questions to explore. First, we would like to know why it is that the precision finite difference method fails at long time for the A-type trajectories, and whether that is a trait specific to the periodic trajectories, or if trajectories starting from other points in phase space would exhibit similar behavior. The ergodic nature of the nonperiodic trajectories guarantees that they sample all of (energetically available) configuration space, but that doesn’t mean that the specific examples chosen are representative of all nonperiodic trajectories in phase space.

Another question to answer is why the naïve method works so well. It is possible that these trajectories simply don’t exhibit enough instability to show the exponential divergence on these timescales. In order to further explore this idea, I’d like to turn to an even more highly non-linear system.

To provide a difficult test, I’d use a Hamiltonian which has been referred as the “quadric oscillator” or the “ $x^2y^2$ ” model. The Hamiltonian for this system is:

$$H(p, q) = \frac{1}{2} (p_x^2 + p_y^2) + \frac{1}{2} x^2 y^2 + \frac{\beta}{4} (x^4 + y^4) \quad (4.15)$$

This potential is illustrated in figure 4.9. This system was studied semiclassically by Kay<sup>58</sup> for the case where  $\beta = 0.01$  (in atomic units, with unit mass).

Part of Kay’s approach to the semiclassical treatment of chaotic systems was to use a cutoff function on the prefactor. If the magnitude of the prefactor is larger than the cutoff function, then that trajectory is thrown out for all later times. One concept which would be of interest would be to see how the various finite difference methods behaved as a function of

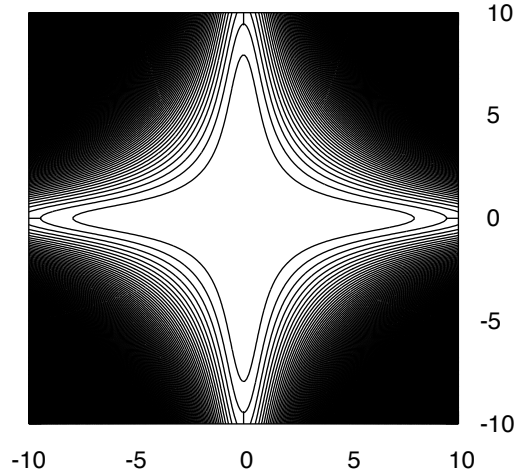


Figure 4.9: The Quadric (or  $x^2y^2$ ) Potential.

whether they were within that cutoff or not. Kay's cutoff is a reasonable, but arbitrary choice, so this idea could be easily expanded to multiple cutoffs bounding several domains. It is possible that we would see that the precision finite difference method (or even the naïve finite difference method) would be better for the trajectories before they are rejected by Kay's algorithm than for the trajectories after they have been rejected.

## Chapter 5

# Semiclassical Treatment of Fermionic Systems

Fermionic dynamics provide a special challenge in semiclassical theory. The more classical the behavior of a system, the better we expect semiclassical theory to do — after all, semiclassical theory should capture all classical effects, as well as whatever quantum effects it can manage. Fermions, however, have two particularly notable nonclassical behaviors.\* The first is the exchange antisymmetry of fermions, which leads to the fact that fermions obey fundamental *anticommutation* relations instead of commutation relations. The second is the Pauli exclusion principle, which prevents any two fermions in a system from having the same set of quantum numbers.

In this chapter we develop a way to treat fermions semiclassically. This work is based on a semiclassical treatment of second quantization, similar to original Meyer-Miller Hamiltonian described in section 1.3.

### 5.1 Classical Mapping of the Quantum Hamiltonian

Capturing semiclassical behavior of fermions remains a difficult problem. The problem is that in addition to mapping a quantum Hamiltonian to a classical Hamiltonian, we also have to account for the antisymmetry of fermions. The approach we suggest here is a bit *ad hoc*, but it seems to work.

One way to map a bosonic Hamiltonian written in second quantization to a classical Hamiltonian was discussed in section 1.3. Fermions present the additional challenge of accounting for the antisymmetry of the wavefunction; to date, no derivation analogous to that of Stock and Thoss (as presented in section 1.3) has been developed for this problem. So we return to the original ideas described by Meyer and Miller.<sup>38</sup> The basic procedure for applying this to fermionic systems was described by Miller and White in reference 59. Although we have made some changes (both to their method and to their derivation), we reprise the basics of the Miller-White idea here.

---

\* Really, these properties are better seen as two sides of the same coin: they are both manifestations of the antisymmetry of the fermionic wavefunction.

The natural way to approach these mappings is in terms of action-angle variables, where the action corresponds to the quantum occupation of a state. In fact, all the calculations in this chapter will remain in action-angle variables, although we will discuss a Cartesian version of this mapping in section 5.1.4.

### 5.1.1 Mapping Matrix Elements to Classical Expressions

The approach to generate our mapping is based on the observation that the second-quantized operator can be factored into a direct product of  $2 \times 2$  matrices, each of which we then map to classical action-angle variables according to Meyer and Miller's spin-matrix mapping method.<sup>60,61</sup>

The idea of Meyer and Miller's spin-matrix mapping method is to "invert"<sup>†</sup> the Heisenberg correspondence principle, which gives the matrix elements of a quantum operator in terms of the corresponding classical function of action-angle variables:

$$\langle n' | \hat{A} | n \rangle = (2\pi)^{-F} \int_0^{2\pi} dq e^{-i(n'-n)q} A_{\text{cl}}(\bar{n}, q) \quad (5.1)$$

where  $\bar{n} = \frac{1}{2}(n'+n)$  and  $F$  is the number of degrees of freedom. To solve for the classical operator  $A_{\text{cl}}(\bar{n}, q)$ , we take the formal inverse of the Fourier transform:

$$A_{\text{cl}}(\bar{n}, q) = \sum_{k \in \mathbb{Z}^F} e^{ikq} \left\langle \bar{n} + \frac{k}{2} \middle| \hat{A} \middle| \bar{n} - \frac{k}{2} \right\rangle \quad (5.2)$$

Now we reach the point where the inverse becomes nonunique (and nonexact). The ambiguity is from the fact that the classical action variable  $\bar{n}$  has to interpolate for all real numbers, while matrix elements are only defined for integer values of the quantum number  $n$ .

The spin-matrix mapping method is one approach to making this "inverse." It is based on the fact that any two-state system is equivalent to a spin  $\frac{1}{2}$  system. In particular, it uses the fact that the spin matrices  $\mathbf{S}_x$ ,  $\mathbf{S}_y$ , and  $\mathbf{S}_z$ , along with the  $2 \times 2$  identity matrix  $\mathbf{1}$ , form a basis for the space of  $2 \times 2$  matrices. Each of these basis matrices are mapped to a function of the classical action-angle variables  $(m, q)$ , where  $m$  is the action variable related to the  $z$ -projection spin quantum number. The identity matrix maps to 1, and the other operators map as

$$\mathbf{S}_x = \sqrt{\sigma^2 - m^2} \cos(q) \quad (5.3a)$$

$$\mathbf{S}_y = \sqrt{\sigma^2 - m^2} \sin(q) \quad (5.3b)$$

$$\mathbf{S}_z = m \quad (5.3c)$$

where  $\sigma$  is the length of the spin vector, the value of which will be discussed in section 5.1.3.

The quantum values of the action variable  $m$  are  $\pm\frac{1}{2}$ , but we would like to discuss this in the context of a system where the quantum values are 0 (for an unoccupied state) or 1 (for an occupied state). To do this, we make the elementary canonical transformation  $n = m + \frac{1}{2}$ . Thus,

---

<sup>†</sup> I put "invert" in quotes because this inverse is not unique.

an arbitrary  $2 \times 2$  matrix  $\mathbf{A}$  can be mapped to a function of the classical action-angle variables  $(n, q)$  as:

$$A(n, q) = (1 - n) A_{00} + n A_{11} + \sqrt{n - n^2 + \lambda} (A_{10} e^{iq} + A_{01} e^{-iq}) \quad (5.4)$$

where  $\lambda = \sigma^2 - \frac{1}{4}$ .

The key idea presented by Miller and White was to use the fact that a second-quantized operator can be factored into a direct product of  $2 \times 2$  matrices, each of which can then be described by the SMM method. This factorization is possible because (for example) the operator  $\hat{a}_i$  only acts on the  $i$ th mode. This allows us to suggest a practical method for mapping any second-quantized fermionic operator to a classical function of the action-angle variables.

First, we'll look at the operator  $\hat{a}_i^\dagger \hat{a}_i$ . The matrix elements for this are simply:

$$\langle n' | \hat{a}_i^\dagger \hat{a}_i | n \rangle = n_i \prod_j \delta_{n'_j, n_j} \quad (5.5)$$

The  $2 \times 2$  matrix associated with all degrees of freedom other than the  $i$ th degree is the identity matrix. For the  $i$ th degree of freedom, the off-diagonal elements are zero, and the diagonal elements are equal to  $n_i$ . So in the basis  $\{|n_i = 0\rangle, |n_i = 1\rangle\}$ , the matrix for the  $i$ th degree of freedom is

$$(\hat{a}_i^\dagger \hat{a}_i)^{(i)} = \begin{pmatrix} 0 & 0 \\ 0 & 1 \end{pmatrix} \quad (5.6)$$

where the parenthetical superscript outside the parentheses on the left-hand side of the equation indicates that this is the  $2 \times 2$  matrix for the contribution to the operator from the  $i$ th degree of freedom. Using equation (5.4), this immediately gives us the mapping

$$\hat{a}_i^\dagger \hat{a}_i \mapsto n_i \quad (5.7)$$

which, as expected, means that the quantum number operator for a given degree of freedom maps to the classical action for that degree of freedom.

The coupling operator  $\hat{a}_i^\dagger \hat{a}_j$  is a little more complicated. The matrix elements are:

$$\langle n' | \hat{a}_i^\dagger \hat{a}_j | n \rangle = \delta_{n'_i, n_{i+1}} \delta_{n'_j, n_{j-1}} \prod_{k \neq i, j} \delta_{n'_k, n_k} \prod_{p=i+1}^{j-1} (-1)^{n_p} \quad (5.8)$$

where we have assumed that  $i < j$ . In the case  $i > j$ , the product over  $p$  goes from  $j+1$  to  $i-1$ : it always includes the states between (but not including)  $i$  and  $j$ . That product is the result of the anticommutation of the fermionic creation/annihilation operators.

We can separate these contributions into four groups: the  $i$ th degree of freedom, the  $j$ th degree of freedom, the degrees of freedom  $p$  located between  $i$  and  $j$ , and all other degrees of freedom. These last group each give the identity matrix, and thus multiply the classical function by 1. For the  $i$ th degree of freedom, the Kronecker delta (indicating a raising of  $n_i$ ) gives the  $2 \times 2$  matrix:

$$(\hat{a}_i^\dagger \hat{a}_j)^{(i)} = \begin{pmatrix} 0 & 0 \\ 1 & 0 \end{pmatrix} \quad (5.9)$$

Using equation (5.4), this gives the contribution to the classical function for the  $i$ th degree of freedom as

$$\left(\hat{a}_i^\dagger \hat{a}_j\right)^{(i)} \mapsto \sqrt{n_i - n_i^2 + \lambda} e^{iq_i} \quad (5.10)$$

The  $j$ th degree of freedom is similar, but the Kronecker delta relates to the lowering of  $n_j$ . So the  $2 \times 2$  matrix is

$$\left(\hat{a}_i^\dagger \hat{a}_j\right)^{(j)} = \begin{pmatrix} 0 & 1 \\ 0 & 0 \end{pmatrix} \quad (5.11)$$

and the classical function corresponding to the  $j$ th degree of freedom is

$$\left(\hat{a}_i^\dagger \hat{a}_j\right)^{(j)} \mapsto \sqrt{n_j - n_j^2 + \lambda} e^{-iq_j} \quad (5.12)$$

That just leaves us the degrees of freedom  $p$  between  $i$  and  $j$ . Each of these degrees gives us a matrix of the form

$$\left(\hat{a}_i^\dagger \hat{a}_j\right)^{(p)} = \begin{pmatrix} 1 & 0 \\ 0 & -1 \end{pmatrix} \quad (5.13)$$

since  $(-1)^{n_p} = 1$  if  $n_p = 0$ , and  $-1$  if  $n_p = 1$ . When we plug this into equation (5.4), we find that the contribution for the degrees  $p$  is

$$\left(\hat{a}_i^\dagger \hat{a}_j\right)^{(p)} \mapsto 1 - 2n_p \quad (5.14)$$

The classical function is the product of the contributions from each of the degrees of freedom. Putting all of this together, so far we have mappings of the form

$$\hat{a}_i^\dagger \hat{a}_i \mapsto n_i \quad (5.15a)$$

$$\hat{a}_i^\dagger \hat{a}_j \mapsto \sqrt{(n_i - n_i^2 + \lambda)(n_j - n_j^2 + \lambda)} e^{i(q_i - q_j)} \prod_{p=i+1}^{j-1} f_b(n_p) \quad (5.15b)$$

where the spin-matrix mapping suggests  $f_b(n_p) = 1 - 2n_p$ . It turns out that this choice for  $f_b(n_p)$  does not work if applied directly. Instead, we find that we get accurate results if we use  $f_b(n_p) = 1$ . This decision is discussed in the next subsection. The value of  $\lambda$ , which we set to  $\frac{1}{2}$ , is discussed in section 5.1.3.

### 5.1.2 Book-Keeping Functions

The influence of the degrees of freedom  $p$  ordered between  $i$  and  $j$  on the term  $\hat{a}_i^\dagger \hat{a}_j$  is worth further discussion. These factors come from the product over  $(-1)^{n_p}$  in the matrix element, which in turn come from the normal ordering rules. Because the fermionic creation and annihilation operators which make up a second-quantized operator anticommute, the order in which the product is written determines its relative phase. In this way, the effect of the degrees of freedom  $p$  tracks the choice of order, and because of that, we'll refer to  $f_b(n_p)$  as the “book-keeping function.”

The book-keeping function of Miller and White is  $f_b = 1 - 2n_p$ . Since the purpose of the book-keeping function is simply to ensure that the system is antisymmetric, it turns out that any function that satisfies the mapping:

$$\begin{pmatrix} 0 \\ 1 \end{pmatrix} \mapsto \begin{pmatrix} 1 \\ -1 \end{pmatrix} \quad (5.16)$$

is a candidate. The book-keeping functions we attempted were:

$$f_b^{\text{lin}} = 1 - 2n_p \quad (5.17a)$$

$$f_b^{\text{exp}} = \exp(i\pi n_p) \quad (5.17b)$$

$$f_b^{\text{none}} = 1 \quad (5.17c)$$

The last option corresponds to no book-keeping at all, and does not satisfy mapping (5.16). When  $j < i$ , we simply switch the role of  $i$  and  $j$  in the bounds — *i.e.*, the states included by  $p$  are always those ordered *between* (but not including) states  $i$  and  $j$ .

All of this has dealt with mapping the term  $\hat{a}_i^\dagger \hat{a}_j$ . In practice, we'll need to map that quantity plus its Hermitian conjugate,  $\hat{a}_j^\dagger \hat{a}_i$ . If we use the book-keeping function  $f_b^{\text{lin}}$ , then both terms contribute the same book-keeping expression (since those functions are real-valued). However, the book-keeping function  $f_b^{\text{exp}}$  is not real-valued, so its complex conjugate appears in the Hermitian conjugate.

This means that the mapping of the sum of the term and its Hermitian conjugate are, for the linear (or any real-valued) book-keeping function:

$$\hat{a}_i^\dagger \hat{a}_j + \hat{a}_j^\dagger \hat{a}_i \mapsto 2\sqrt{(n_i - n_i^2)(n_j - n_j^2)} \cos(q_i - q_j) \prod_{p=i+1}^{j-1} f_b(n_p) \quad (5.18)$$

However, for the exponential book-keeping function, the mapping is:

$$\hat{a}_i^\dagger \hat{a}_j + \hat{a}_j^\dagger \hat{a}_i \mapsto 2\sqrt{(n_i - n_i^2)(n_j - n_j^2)} \cos(q_i - q_j + \theta_b) \quad (5.19)$$

where  $\theta_b = \pi \sum_{p=i+1}^{j-i} n_p$ . As before, if  $j < i$ , then the role of  $i$  and  $j$  in the sum over  $p$  are switched such that the sum is always over the states between  $i$  and  $j$ .

Figure 5.7 shows the results for the different kinds of book-keeping functions. While the results were, of course, dependent on the parameters of the system, the general trend was that the linear book-keeping decayed to zero, the exponential book-keeping found a plateau that was too small, and no book-keeping gave very good results. On that basis, we chose to use  $f_b(n_p) = 1$ , the no book-keeping method, for our calculations.

The source of the problem is clearly that the book-keeping factor shouldn't affect the magnitude of the mapping, but the continuous nature of the book-keeping in the above methods causes even the exponential form to change the magnitude when  $n_p \neq \pm 1$ . Another possibility, which we haven't explored, would be to force the book-keeping function to be  $\pm 1$ , perhaps by using  $f_b = \prod_{p=i+1}^{j-1} (-1)^{h(n_p - \frac{1}{2})}$ , where  $h(n)$  is the Heaviside function. Using this in the dynamics might be complicated due to the resulting Dirac delta in the time derivative of the angle variable,

so it might be approximated by some smoothed step function, such as a hyperbolic tangent. Yet another possibility would be to ignore it in the dynamics but to apply it as part of the operator.

However, an argument for the no-book-keeping method comes from one of the non-physical results of implementing these book-keeping functions as described above. Since the terms included in the book-keeping depend on the order in which the classical variables are listed, the result depends on that order. We hoped that there would be some evidence that after averaging over many trajectories this ordering effect would disappear, but for the book-keeping functions we tested this was manifestly not the case.<sup>†</sup>

Since order shouldn't matter, one approach would be to consider the average over all possible orders. Clearly, the quantum result will be the same for any ordering, so it gives the same answer trivially. But since different orderings matter for the classical model, we consider the average over all possible orderings. Consider the operator  $\hat{a}_\alpha^\dagger \hat{a}_\beta$ . In the following discussion, the labels  $\alpha$  and  $\beta$  will correspond to a given *state*, regardless of the order, and the labels  $i$  and  $j$  will correspond to a specific ordering.

Let  $S_F$  be the set of all orderings (permutations) of the  $F$  degrees of freedom in the system, and  $N_{S_F}$  be the number of permutations in that set. In that case, the average over all orderings is

$$\hat{a}_\alpha^\dagger \hat{a}_\beta = \frac{1}{N_{S_F}} \sum_{\sigma \in S_F} \hat{a}_{\sigma(\alpha)}^\dagger \hat{a}_{\sigma(\beta)} \quad (5.20)$$

Quantum mechanically, this equation must be true because any order should give the same results. Now we note that we can reorganize the permutations based on the number of states between state  $\alpha$  and state  $\beta$ . Let  $S_F^{(m)}$  be the set of permutations in which  $\alpha$  and  $\beta$  are separated by  $m$  states. Then we can write

$$\hat{a}_\alpha^\dagger \hat{a}_\beta = \frac{1}{N_{S_F}} \sum_{m=0}^{F-2} \sum_{\sigma \in S_F^{(m)}} \hat{a}_{\sigma(\alpha)}^\dagger \hat{a}_{\sigma(\beta)} \quad (5.21)$$

Now if we make the semiclassical mapping, we obtain

$$\hat{a}_\alpha^\dagger \hat{a}_\beta \mapsto \frac{1}{N_{S_F}} \sum_{m=0}^{F-2} \sum_{\sigma \in S_F^{(m)}} \sqrt{(n_\alpha - n_\alpha^2 + \lambda)(n_\beta - n_\beta^2 + \lambda)} e^{i(q_\alpha - q_\beta)} \prod_{p=i+1}^{i-1} f_b(n_p) \quad (5.22)$$

$$= \sqrt{(n_\alpha - n_\alpha^2 + \lambda)(n_\beta - n_\beta^2 + \lambda)} e^{i(q_\alpha - q_\beta)} \frac{1}{N_{S_F}} \sum_{m=0}^{F-2} \sum_{\sigma \in S_F^{(m)}} \prod_{p=i+1}^{i-1} f_b(n_p) \quad (5.23)$$

where  $i = \min(\sigma(\alpha), \sigma(\beta))$  and  $j = \max(\sigma(\alpha), \sigma(\beta))$ . This gives us a new book-keeping term, replacing the product over the underlying book-keeping function with the term

$$\pi_f = \frac{1}{N_{S_F}^{m_{\max}}} \sum_{m=0}^{m_{\max}} \sum_{\sigma \in S_F^{(m)}} \prod_{p=i+1}^{i-1} f_b(n_p) \quad (5.24)$$

---

<sup>†</sup> A simple test for this, based on the resonant-level (Landauer) system described later in this chapter, is to study the system at zero gate voltage and zero bias, with the degrees of freedom ordered at dot, left lead, right lead. Physically, the left and right currents should be equivalent for these parameters, so any deviation from that (beyond numerical error) indicates that the ordering is important.

where  $m_{\max}$  is  $F - 2$  if we average over all orderings, and  $N_{S_F}^{m_{\max}} = \sum_{m=0}^{m_{\max}} N_{S_F}^{(m)}$ . We can take this expansion to an arbitrary number  $m_{\max}$  of modes separating  $\alpha$  and  $\beta$ . The “no book-keeping” method, which we have found to give excellent results, is just the zeroth order expansion of this series.

This expansion is essentially a perturbation expansion, and as such, there are no guarantees that the results converge with the inclusion of more orders. However, this does provide a rough justification for our method, and it has the important feature that any value of  $m_{\max}$ , with any underlying  $f_b(n)$ , will give a result which is independent of the order of the labels of the degrees of freedom.

### 5.1.3 Choosing the Length $\sigma$

The last step in designing our classical mapping is to choose the value of  $\lambda$  from the expressions above. Since  $\lambda = \sigma^2 - \frac{1}{4}$ , this is the same as deciding the length  $\sigma$  which we associate with the spin vector.

We consider two main possibilities: the quantum value and the Langer-modified value. We also explore the idea of treating the Langer modification as a free parameter. The quantum value is based on the idea that  $\sigma^2$  should be the eigenvalue of the  $\hat{\mathbf{S}}^2$  operator, which for spin  $s$  is  $s(s+1)$ . Since we’re dealing with a spin  $\frac{1}{2}$  system,  $s = \frac{1}{2}$ , so  $\sigma^2 = \frac{3}{4}$  and  $\lambda = \frac{1}{2}$ .

The Langer modification is a common idea in semiclassical dynamics, and the Langer modified value was the version originally suggested by Miller and White. The original Langer modification was an attempt to remove the singularity of potentials of the form  $1/r^n$ .<sup>39</sup> In particular, Langer’s modification of the centrifugal potential  $-\frac{l(l+1)}{r^2}$  results in simply replacing  $l(l+1)$  with  $(l' + \frac{1}{2})^2$ . Making a similar change in the spin  $\frac{1}{2}$  system gives us  $\sigma^2 = (s + \frac{1}{2})^2 = 1$ , and  $\lambda = \frac{3}{4}$ .

In the case of the Meyer-Miller mapping described in reference 38, the Langer modification is required to reproduce the results of the Stock-Thoss derivation (described in reference 40 and followed in section 1.3). In that case, the Langer modification adds  $\frac{1}{2}$  to the action variables, and relates to the fact that the harmonic oscillator energy levels (which get brought in by using the harmonic oscillator isomorphism in the Stock-Thoss derivation) are  $n + \frac{1}{2}$ .

If we think about histogramming the continuous action onto the allowed quantum values of 0 and 1, we can see a couple other advantages of the Miller-White choice of using the Langer modification in the treatment of fermions. First, let’s assume the histogram acts as a Heaviside function at  $\frac{1}{2}$ : if  $n < \frac{1}{2}$ , it is histogrammed as the quantum value 0, and if  $n > \frac{1}{2}$ , it is histogrammed as 1. The Miller-White choice is the unique choice that gives boxes of allowed classical values with equal (unit) width, which are centered on the quantum allowed values.

Unfortunately, we find that the Miller-White choice doesn’t reproduce the dynamics accurately. However, we’d like to keep as many of those advantages as possible. Even when we treat the Langer modification as a free parameter (as was previously done by Stock)<sup>62</sup> we use the form  $n - n^2 + \lambda$ , which keeps the dividing surface at  $\frac{1}{2}$  and forces the boxes to be of equal width. The parameter  $\lambda$  determines the width of the boxes, and  $\lambda = \frac{3}{4}$  corresponds to the Langer modification, while  $\lambda = \frac{1}{2}$  corresponds to the choice of the exact quantum length.

It would be more elegant to fit our choice based on a physical model system than to

justify it based solely on experimentation with a free parameter. In this case, we choose the 2-state system with coupling  $k \in \mathbb{R}$  and diagonal elements  $\epsilon_0 = \epsilon_1 = 0$ . This gives us the Hamiltonian:

$$\hat{H} = k(a_0^\dagger a_1 + a_1^\dagger a_0) \quad (5.25)$$

The corresponds to the  $2 \times 2$  Hamiltonian matrix (in the basis  $\{|\psi_0\rangle, |\psi_1\rangle\}$ )

$$\hat{H} = \begin{pmatrix} 0 & k \\ k & 0 \end{pmatrix} \quad (5.26)$$

which has eigenvalues  $E_\pm = \pm k$  with eigenvectors  $|\psi_\pm\rangle = \frac{1}{\sqrt{2}}(|\psi_0\rangle \pm |\psi_1\rangle)$ . Therefore, the time-evolution operator is:

$$e^{-i\hat{H}t} = |\psi_+\rangle e^{ikt} \langle \psi_+| + |\psi_-\rangle e^{-ikt} \langle \psi_-| \quad (5.27)$$

The population of (or probability of being in) state 0 is given by the operator  $\hat{N}_0(t) = \left| \langle \psi_0 | e^{-i\hat{H}t} | \Psi \rangle \right|^2$ , where  $|\Psi\rangle$  is our initial state. If we choose our initial state to be  $|\Psi\rangle = |\psi_0\rangle$ , then we have:

$$\hat{N}_0(t) = \left| \langle \psi_0 | e^{-i\hat{H}t} | \psi_0 \rangle \right|^2 \quad (5.28)$$

$$= \left| \langle \psi_0 | \psi_+ \rangle e^{ikt} \langle \psi_+ | \psi_0 \rangle + \langle \psi_0 | \psi_- \rangle e^{-ikt} \langle \psi_- | \psi_0 \rangle \right|^2 \quad (5.29)$$

$$= \left| \frac{1}{2} (e^{ikt} + e^{-ikt}) \right|^2 = \cos^2(kt) \quad (5.30)$$

Taking the first derivative:

$$\dot{\hat{N}}_0(t) = -2k \cos(kt) \sin(kt) = -k \sin(2kt) \quad (5.31)$$

$$\dot{\hat{N}}_0(0) = 0 \quad (5.32)$$

And the second derivative:

$$\ddot{\hat{N}}_0(t) = -2k^2 \cos(2kt) \quad (5.33)$$

$$\ddot{\hat{N}}_0(0) = -2k^2 \quad (5.34)$$

Now we turn to our classical mapping. With an arbitrary Langer modification  $\lambda$ , the Hamiltonian (5.25) maps to:

$$H = 2k \sqrt{(n_0 - n_0^2 + \lambda)(n_1 - n_1^2 + \lambda)} \cos(q_0 - q_1) \quad (5.35)$$

The operator  $\hat{N}_0$  simply maps to the action variable  $n_0$ , so its time derivative maps to  $\dot{n}_0$ :

$$\dot{n}_0(t) = -2k \sqrt{(n_0 - n_0^2 + \lambda)(n_1 - n_1^2 + \lambda)} \sin(q_0 - q_1) \quad (5.36)$$

If we average over initial angle variables, this gives us zero, just as in the quantum result, equation (5.32).

Since we get zero for the first derivative, we move on to using the second derivative to set the value of  $\lambda$ . Our classical second derivative, in terms of the partial derivatives, is:

$$\ddot{n}_0(t) = \frac{\partial \dot{n}_0}{\partial n_0} \dot{n}_0 + \frac{\partial \dot{n}_0}{\partial n_1} \dot{n}_1 + \frac{\partial \dot{n}_0}{\partial q_0} \dot{q}_0 + \frac{\partial \dot{n}_0}{\partial q_1} \dot{q}_1 \quad (5.37)$$

Now we'll calculate the partial derivatives of  $\dot{n}_0$ . For simplicity, we'll write them all in terms of a factor of  $\dot{n}_0$ .

$$\frac{\partial \dot{n}_0}{\partial n_0} = \frac{1}{2} \frac{1 - 2n_0}{n_0 - n_0^2 + \lambda} \dot{n}_0 \quad (5.38)$$

$$\frac{\partial \dot{n}_0}{\partial n_1} = \frac{1}{2} \frac{1 - 2n_1}{n_1 - n_1^2 + \lambda} \dot{n}_0 \quad (5.39)$$

$$\frac{\partial \dot{n}_0}{\partial q_0} = \cot(q_0 - q_1) \dot{n}_0 \quad (5.40)$$

$$\frac{\partial \dot{n}_0}{\partial q_1} = -\cot(q_0 - q_1) \dot{n}_0 \quad (5.41)$$

The time derivatives of the variables are given by Hamilton's equations of motion. Again, we'll write these in terms of  $\dot{n}_0$ . Obviously  $\dot{n}_0(t)$  is itself; and due to the conservation of total action,  $\dot{n}_1(t) = -\dot{n}_0(t)$ . The time derivatives of the angle variables are:

$$\dot{q}_0(t) = \frac{1}{2} \frac{1 - n_0}{n_0 - n_0^2 + \lambda} \cot(q_0 - q_1) \dot{n}_0 \quad (5.42)$$

$$\dot{q}_1(t) = \frac{1}{2} \frac{1 - n_1}{n_1 - n_1^2 + \lambda} \cot(q_0 - q_1) \dot{n}_0 \quad (5.43)$$

With the partial parts in hand, we assemble them into the full derivative expression (5.37):

$$\ddot{n}_0(t) = \frac{1}{2} \dot{n}_0^2 \left( \frac{1 - 2n_0}{n_0 - n_0^2 + \lambda} - \frac{1 - 2n_1}{n_1 - n_1^2 + \lambda} \right) (1 + \cot^2(q_0 - q_1)) \quad (5.44)$$

$$\begin{aligned} &= \frac{1}{2} 4k^2 (n_0 - n_0^2 + \lambda)(n_1 - n_1^2 + \lambda) \left( \frac{1 - 2n_0}{n_0 - n_0^2 + \lambda} - \frac{1 - 2n_1}{n_1 - n_1^2 + \lambda} \right) \\ &\quad \times (\sin^2(q_0 - q_1) + \cos^2(q_0 - q_1)) \end{aligned} \quad (5.45)$$

$$= 2k^2 (n_0 - n_0^2 + \lambda)(n_1 - n_1^2 + \lambda) \left( \frac{1 - 2n_0}{n_0 - n_0^2 + \lambda} - \frac{1 - 2n_1}{n_1 - n_1^2 + \lambda} \right) \quad (5.46)$$

At this point, we recall that our initial conditions are  $n_0(0) = 1$  and  $n_1(0) = 0$ . That gives us the result

$$\ddot{n}_0(0) = (2k^2 \lambda^2) \left( -\frac{2}{\lambda} \right) = -4k^2 \lambda \quad (5.47)$$

To set a value for  $\lambda$ , we force this to equal the quantum result from equation (5.34):

$$-4k^2 \lambda = -2k^2 \implies \lambda = \frac{1}{2} \quad (5.48)$$

As discussed above, this corresponds to choosing the quantum value for the length of the spin vector. In addition to this justification, we will see in figure 5.8 that the experimental approach verifies this choice.

### 5.1.4 Aside: Cartesian Expressions for this Mapping

The work presented in this chapter was all done in action-angle variables, but a further analogy with the earlier work by Meyer and Miller on nonadiabatic dynamics presents us with a method for generating dynamics with Cartesian variables which correspond to the mapping we have described.

Equations in the form given by the spin-matrix mapping formalism, *i.e.*, equation (5.4), were already known in the context of the MMST Hamiltonian presented in section 1.3. First we express the MMST Hamiltonian (1.133) in action-angle variables (for the electronic degrees of freedom) in the case that we have two electronic states with  $V_{12} = V_{21}$  and no dependence on nuclear degrees of freedom:

$$H = n_1 V_{11} + n_2 V_{22} + 2\sqrt{(n_1 + \gamma)(n_2 + \gamma)} \cos(q_1 - q_2) V_{12} \quad (5.49)$$

(This was actually the original expression for the MMST Hamiltonian, as proposed by Meyer and Miller in reference 38.) As we observed in section 1.3, this is an exact mapping within the polyad of a single excitation. Within that polyad, we have  $n_1 + n_2 = 1$ . Now we write this Hamiltonian within that polyad, in terms of  $n = n_1$  (so  $n_2 = 1 - n_1$ ) and  $q = q_1 - q_2$ :

$$H = n V_{11} + (1 - n) V_{22} + 2\sqrt{n - n^2 + \gamma(1 + \gamma)} \cos(q) V_{12} \quad (5.50)$$

Of course, this is exactly equation (5.4) if  $A_{10} = A_{01}$  and  $\lambda = \gamma(1 + \gamma)$ .

What we have done above is to rewrite a two-dimensional system subject to a constraint as a one-dimensional system. In order to obtain a Cartesian representation of our system, we reverse the process: we double the size of the system.

The basic idea is just to reverse the process described above for each degree of freedom in our original Hamiltonian. One point of subtlety is that the term  $\epsilon_k \hat{a}_k^\dagger \hat{a}_k$  is now mapped to  $\epsilon_{k_0} n_{k_0} + \epsilon_{k_1} n_{k_1}$ . However, the energy of the unoccupied state  $\epsilon_{k_0}$  is zero for all values of  $k$ .

The result is that we now have the mappings:

$$\hat{a}_i^\dagger \hat{a}_i \mapsto n_{i_1} \quad (5.51a)$$

$$\hat{a}_i^\dagger \hat{a}_j + \hat{a}_j^\dagger \hat{a}_i \mapsto 2\sqrt{(n_{i_0} + \gamma)(n_{i_1} + \gamma)(n_{j_0} + \gamma)(n_{j_1} + \gamma)} \cos((q_{i_1} - q_{i_0}) - (q_{j_1} - q_{j_0})) \quad (5.51b)$$

where we have omitted the book-keeping functions  $f_b(n)$  for simplicity. If we require that  $n_{i_0} + n_{i_1} = 1 \forall i$ , we regain our original mappings through the procedure described above for converting the 2-state MMST Hamiltonian to a 1-state Hamiltonian.

Now we convert this to Cartesian coordinates. In terms of the action-angle coordinates, the Cartesian coordinates are:

$$x_{k_\alpha} = \sqrt{2(n_{k_\alpha} + \gamma)} \cos(q_{k_\alpha}) \quad (5.52)$$

$$p_{k_\alpha} = -\sqrt{2(n_{k_\alpha} + \gamma)} \sin(q_{k_\alpha}) \quad (5.53)$$

with  $k \in \{1, \dots, N\}$  and  $\alpha \in \{0, 1\}$ . This gives us

$$\sqrt{n_{k_\alpha} + \gamma} e^{\pm iq_{k_\alpha}} = \frac{1}{\sqrt{2}} (x_{k_\alpha} \mp ip_{k_\alpha}) \quad (5.54)$$

When we plug this into our doubled-state mapping (5.51), we obtain:

$$\hat{a}_i^\dagger \hat{a}_i \mapsto \frac{1}{2} (x_{i_1}^2 + p_{i_1}^2 - \gamma) \quad (5.55a)$$

$$\hat{a}_i^\dagger \hat{a}_j + \hat{a}_j^\dagger \hat{a}_i \mapsto (x_{i_0} x_{i_1} + p_{i_0} p_{i_1}) (x_{j_0} x_{j_1} + p_{j_0} p_{j_1}) + (x_{i_0} p_{i_1} - x_{i_1} p_{i_0}) (x_{j_0} p_{j_1} - x_{j_1} p_{j_0}) \quad (5.55b)$$

It turns out that we can obtain a similar mapping by using a result by Klauder.<sup>63</sup> We start by recalling that these operators can be written in terms of the spin matrices (and the  $2 \times 2$  identity matrix  $\mathbf{1}$ ) as:

$$\hat{a}_i^\dagger \hat{a}_i = \frac{1}{2} (\mathbf{1}^{(i)} + \mathbf{S}_z^{(i)}) \quad (5.56)$$

$$\hat{a}_i^\dagger \hat{a}_j + \hat{a}_j^\dagger \hat{a}_i = (\mathbf{S}_x^{(i)} + i\mathbf{S}_y^{(i)}) (\mathbf{S}_x^{(j)} - i\mathbf{S}_y^{(j)}) + (\mathbf{S}_x^{(j)} + i\mathbf{S}_y^{(j)}) (\mathbf{S}_x^{(i)} - i\mathbf{S}_y^{(i)}) \quad (5.57)$$

$$= 2 (\mathbf{S}_x^{(i)} \mathbf{S}_x^{(j)} + \mathbf{S}_y^{(i)} \mathbf{S}_y^{(j)}) \quad (5.58)$$

where the superscript  $(k)$  indicates that this is spin matrix associated with the  $k$ th electronic variables, and where we have left off the book-keeping term.

Klauder showed that the spin matrices can be written as:

$$\mathbf{S}_x = p_0 p_1 + x_0 x_1 \quad (5.59)$$

$$\mathbf{S}_y = x_0 p_1 - p_0 x_1 \quad (5.60)$$

$$\mathbf{S}_z = \frac{1}{2} (p_0^2 + x_0^2 - p_1^2 - x_1^2) \quad (5.61)$$

where the system is under the constraint

$$x_0^2 + p_0^2 + x_1^2 + p_1^2 = 4s \quad (5.62)$$

From this constraint, we can obtain a Cartesian mapping for the identity matrix for a spin  $s = \frac{1}{2}$  system:

$$\mathbf{1} = \frac{1}{2} (x_0^2 + p_0^2 + x_1^2 + p_1^2) \quad (5.63)$$

When we use Klauder's Cartesian form of the spin matrices on the expression for the off-diagonal elements  $\hat{a}_i^\dagger \hat{a}_j$  in equation (5.58), we get exactly the mapping from (5.55b).

Unfortunately, we don't quite get the same result for the diagonal elements  $\hat{a}_i^\dagger \hat{a}_i$  from Klauder's expressions, which would give us

$$\hat{a}_i^\dagger \hat{a}_i \mapsto \frac{1}{2} (x_{i_0}^2 + p_{i_0}^2) \quad (5.64)$$

By applying the constraint identity (5.62), we can make this into a form that bears a little more resemblance to the mapping (5.55a):

$$\hat{a}_i^\dagger \hat{a}_i \mapsto -\frac{1}{2} (x_{i_1}^2 + p_{i_1}^2 - 2) \quad (5.65)$$

but the sign of mapping is off, and the value of  $\gamma$  is wrong.

## 5.2 Measuring the Time-Dependent Current: Treatment of Operators

We're interested in studying the time-dependent current. By definition, the current is the change in the number of electrons as a function of time, *i.e.*, the flux of electron population through some surface (since the total electron population is conserved).

We can study this flux through any of several dividing surfaces. We define the left current  $\hat{I}_L$  as the flux of electrons from a “left” bath into the quantum dot system. Similarly, we define right current  $\hat{I}_R$  as the flux of electrons from the “right” bath into the quantum dot system. The total current  $\hat{I}$  is given as the flux through the quantum dot system. Since the total number of electrons is conserved, the total current is given by

$$\hat{I} = \frac{1}{2} (\hat{I}_L - \hat{I}_R) \quad (5.66)$$

We typically choose “left” and “right” such that the total current at steady state is positive (*i.e.*, the overall flow of electrons is from left to right).

The general problem we're exploring is that of quantum transport — in molecular electronics, the current is an obvious transport quantity to study. It is relatively straightforward to study both theoretically and experimentally. Some other methods only study the steady-state currents, but here we also explore the initial time-dependent transients.

### 5.2.1 Discretization of the Spectral Density

We describe the systems we're interested in as a central state (the quantum dot) sandwiched between two electrodes, which serve as (fermionic) baths. Formally, these baths are described by spectral density functions, which give the coupling strength to the bath modes at all (continuous) frequencies. But every bath frequency must correspond to a single (discrete) classical degree of freedom in our dynamics, so we have to discretize the spectral density.

Technically, the conduction problem we're studying should be described by an infinitely broad and flat bath, the magnitude of which is determined by the coupling,  $\Gamma$ . However, only a small range of modes will be thermally accessible, so we choose a spectral density of a form that is effectively a non-zero constant over a region of interest, but which drops to zero outside of that region of interest. Specifically, we choose:

$$J_{L/R}(\epsilon) = \frac{\Gamma_{L/R}}{\left(1 + e^{A(\epsilon - \frac{B}{2})}\right)\left(1 + e^{-A(\epsilon + \frac{B}{2})}\right)} \quad (5.67)$$

where  $B$  is the width of our region of interest, and  $\Gamma_{L/R}$  is the coupling to the left or right bath. The quantity  $A$  relates to how sharp the cutoff is (or, equivalently, how flat the region of interest is). For this work, we choose to work in scaled units where  $\Gamma_L = \Gamma_R = \frac{1}{2}$ .

The coupling constant for a given frequency  $\epsilon_k$  is given according to the formula:

$$t_k = \sqrt{\frac{J(\epsilon_k)}{2\pi\rho(\epsilon_k)}} \quad (5.68)$$

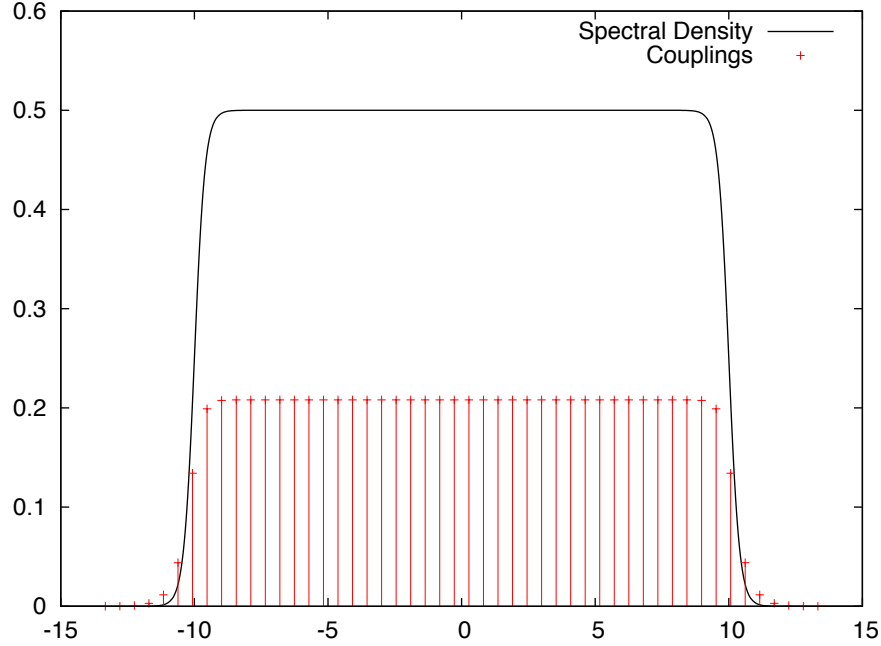


Figure 5.1: Discretization of the spectral density into 50 discrete modes with  $A = 5$  and  $B = 20$ .

We choose a uniformly spaced discretization of  $\epsilon_k$ , which gives  $\rho(\epsilon) = 1/\Delta\epsilon$ .

Figure 5.1 shows this discretization for a typical set of parameters ( $A = 5$ ,  $B = 20$ ), with 50 discrete modes. As we add more modes, the individual coupling constants decrease because their spacing grows smaller.

### 5.2.2 Describing the Initial Conditions

One can quickly show that the Hamiltonian described above fails to provide an accurate Boltzmann operator for a fermionic system, since the quantum partition function for a single fermionic degree of freedom is

$$Q \propto e^{-\beta\epsilon} + 1 \quad (5.69)$$

(the first term representing the occupied state and the second term the unoccupied). The mapped classical Hamiltonian above gives

$$Q \propto \int_a^b dn e^{-\beta\epsilon n} = \frac{1}{\beta\epsilon} \left( e^{-\beta\epsilon a} - e^{-\beta\epsilon b} \right) \quad (5.70)$$

Regardless of our choice of bounds  $a$  and  $b$ , this will obviously not match the quantum result. Therefore, we can't count on the mapped Hamiltonian we described in section 5.1 to give us accurate statistics.

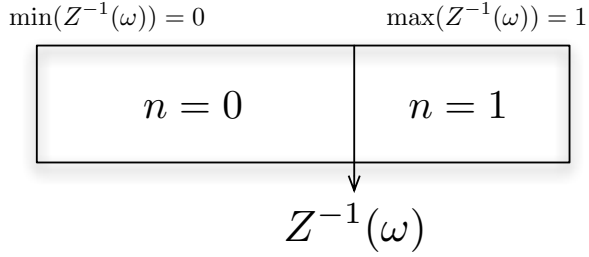


Figure 5.2: Illustration of the idea behind our sampling method. A random number is selected between 0 and 1. If it is less than  $Z^{-1}(\omega)$ , then the action  $n$  is zero. Otherwise, the action is one.

In order to get accurate statistics, we take a quasi-classical approach. That is to say, we populate the states according to the quantum Boltzmann operator, guaranteeing quantum statistics at time  $t = 0$ . Then we run the dynamics using the Hamiltonian described in section 5.1.

In this work, we assume that the coupling is off before  $t = 0$ . That is, we populate the states in each bath according to the (quantum) Hamiltonian  $\hat{H} = \sum_{k \in \text{bath}} \epsilon_k \hat{a}_k^\dagger \hat{a}_k$ . The result is that the Boltzmann operator can be written as a direct product over the modes, allowing each mode to be sampled independently.

We populate the initial action variables  $n_i$  by first selecting a random number  $\chi_i$  and choosing  $n_i$  according to the rule:

$$n_i = \begin{cases} 0 & \text{if } \chi_i < (1 + e^{-\beta(\epsilon_i - \mu_i)})^{-1}, \\ 1 & \text{otherwise.} \end{cases} \quad (5.71)$$

where  $\mu_i$  is the chemical potential (or voltage) associated with the electrode. The initial angles are selected as uniform random numbers in the range  $q_i \in [0, 2\pi)$ .

This method ends up giving us the Fermi distribution for our populations. The Fermi function is

$$f(\omega; \beta) = (1 + e^{\beta\omega})^{-1} \quad (5.72)$$

where  $\omega = \epsilon - \mu$  for our situation. The idea of our sampling methodology is that we are comparing our random number to what we'll call  $Z^{-1}(\omega)$ , given by

$$Z^{-1}(\omega) = \frac{1}{1 + e^{-\beta\omega}} \quad (5.73)$$

We note that  $\forall \omega, Z^{-1}(\omega) \in (0, 1)$ . The basic idea of the sampling method is illustrated in figure 5.2.

We can quickly show that this sampling method recovers the Fermi distribution. Let  $P(0)$  be the probability that  $n = 0$  and  $P(1)$  be the probability that  $n = 1$ . Clearly, the method described above gives  $P(0) = Z^{-1}(\omega)$ . So the expectation value  $\langle n \rangle$ , which should be given by

the Fermi function, is:

$$\begin{aligned}\langle n \rangle &= 0 \cdot P(0) + 1 \cdot P(1) \\ &= 1 \cdot (1 - P(0)) = 1 - Z^{-1}(\omega) \\ &= \frac{(1 + e^{-\beta\omega}) - 1}{1 + e^{-\beta\omega}} = \frac{1}{e^{\beta\omega} + 1} = f(\omega; \beta)\end{aligned}$$

which, indeed, is the Fermi function.

### 5.2.3 The Current Operator

The next step is to describe the current operator. There are two ways of approaching this problem, depending on when one decides to switch from the quantum picture to the semiclassical picture.

Quantum mechanically, we can explore the left current, the right current, or the total current. The total current is described in terms of the left and right currents as  $\hat{I}_{\text{tot}} = (\hat{I}_L - \hat{I}_R)/2$ . The left (or, respectively, right) current is given by the change in the total occupation of the left (right) current with respect to time:

$$\hat{I}_L = -\frac{d\hat{N}_L}{dt} \quad (5.74)$$

In second quantization, the number operator  $\hat{N}_L = \sum_{i \in L} \hat{a}_i^\dagger \hat{a}_i$ , where  $L$  is the set of mode labels in the “left” electrode.

As this point, we have two choices: we can either map the operator  $\hat{N}_L$  to a classical quantity and take the time derivative of that result, or we can take the quantum time derivative of  $\hat{N}_L$  and map that result to a classical operator. We have looked at both possibilities.

The first suggestion, mapping  $\hat{N}_L$  to a classical operator and taking its time derivative, is easy. As described above, the term  $\hat{a}_i^\dagger \hat{a}_i$  maps to the classical expression  $n_i$ . So the number operator maps as:

$$\sum_{i \in L} \hat{a}_i^\dagger \hat{a}_i \mapsto \sum_{i \in L} n_i \quad (5.75)$$

We can either output this directly and take the time derivative numerically or take the time derivative formally. The formal derivative, of course, depends on the Hamiltonian in question. However, our first test system, the Landauer Hamiltonian (described in section 5.3) is part of other Hamiltonians of interest, so we’ll look at its time derivative:

$$-\sum_{i \in L} \dot{n}_i = -\sum_{i \in L} \frac{dH}{dq_i} = -\sum_{i \in L} 2t_i \sqrt{(n_0 - n_0^2 + \lambda)(n_i - n_i^2 + \lambda)} \sin(q_0 - q_i) \quad (5.76)$$

The other approach is to first calculate the time derivative of the quantum operator, and then map that to a classical operator. In this case, we take the time derivative according to the Heisenberg equation of motion:

$$\frac{d}{dt} \sum_{i \in L} \hat{a}_i^\dagger \hat{a}_i = i \sum_{i \in L} [\hat{H}, \hat{a}_i^\dagger \hat{a}_i] \quad (5.77)$$

Again, to see a specific example, we turn to the Landauer Hamiltonian:

$$\frac{d\hat{N}}{dt} = i \sum_{i \in L} \left[ \epsilon_i \hat{a}_i^\dagger \hat{a}_i + \sum_{j \neq i} \epsilon_j \hat{a}_j^\dagger \hat{a}_j + t_i (\hat{a}_0^\dagger \hat{a}_i + \hat{a}_i^\dagger \hat{a}_0) + \sum_{j \neq i} + t_j (\hat{a}_0^\dagger \hat{a}_j + \hat{a}_j^\dagger \hat{a}_0), \hat{a}_i^\dagger \hat{a}_i \right] \quad (5.78)$$

$$\begin{aligned} &= i \sum_{i \in L} \left( [\epsilon_i \hat{a}_i^\dagger \hat{a}_i, \hat{a}_i^\dagger \hat{a}_i] + \sum_{j \neq i} \epsilon_j [\hat{a}_j^\dagger \hat{a}_j, \hat{a}_i^\dagger \hat{a}_i] + t_i [\hat{a}_0^\dagger \hat{a}_i, \hat{a}_i^\dagger \hat{a}_i] + t_i [\hat{a}_i^\dagger \hat{a}_0, \hat{a}_i^\dagger \hat{a}_i] \right. \\ &\quad \left. + \sum_{j \neq i} t_j [\hat{a}_0^\dagger \hat{a}_j, \hat{a}_i^\dagger \hat{a}_i] + \sum_{j \neq i} t_j [\hat{a}_j^\dagger \hat{a}_0, \hat{a}_i^\dagger \hat{a}_i] \right) \end{aligned} \quad (5.79)$$

Since we're dealing with the commutators of operators that are quadratic in the fermion ladder operators, all commutators where the ladder operators in the left operator anticommute with the ladder operators in the right operators (*i.e.*, those where the left and right operators do not share a subscript) vanish. Additionally, the trivial commutator vanishes. That leaves us with:

$$\frac{d\hat{N}}{dt} = i \sum_{i \in L} t_i ([\hat{a}_0^\dagger \hat{a}_i, \hat{a}_i^\dagger \hat{a}_i] + [\hat{a}_i^\dagger \hat{a}_0, \hat{a}_i^\dagger \hat{a}_i]) \quad (5.80)$$

$$= i \sum_{i \in L} t_i (\hat{a}_i^\dagger \hat{a}_0 \hat{a}_i^\dagger \hat{a}_i - \hat{a}_i^\dagger \hat{a}_i \hat{a}_i^\dagger \hat{a}_0 + \hat{a}_0^\dagger \hat{a}_i \hat{a}_i^\dagger \hat{a}_i - \hat{a}_i^\dagger \hat{a}_i \hat{a}_0^\dagger \hat{a}_i) \quad (5.81)$$

$$= i \sum_{i \in L} t_i (\hat{a}_i^\dagger \hat{a}_i^\dagger \hat{a}_i \hat{a}_0 - \hat{a}_i^\dagger \hat{a}_i \hat{a}_i^\dagger \hat{a}_0 - \hat{a}_i \hat{a}_i^\dagger \hat{a}_i \hat{a}_0^\dagger + \hat{a}_i^\dagger \hat{a}_i \hat{a}_i \hat{a}_0^\dagger) \quad (5.82)$$

$$= i \sum_{i \in L} t_i (\hat{a}_i^\dagger \hat{a}_i^\dagger \hat{a}_i \hat{a}_0 - \hat{a}_i^\dagger (1 - \hat{a}_i^\dagger \hat{a}_i) \hat{a}_0 - (1 - \hat{a}_i^\dagger \hat{a}_i) \hat{a}_i \hat{a}_0^\dagger + \hat{a}_i^\dagger \hat{a}_i \hat{a}_i \hat{a}_0^\dagger) \quad (5.83)$$

$$= i \sum_{i \in L} t_i (\hat{a}_0^\dagger \hat{a}_i - \hat{a}_i^\dagger \hat{a}_0 + 2\hat{a}_i^\dagger \hat{a}_i^\dagger \hat{a}_i \hat{a}_0 + 2\hat{a}_i^\dagger \hat{a}_i \hat{a}_i \hat{a}_0^\dagger) \quad (5.84)$$

$$= i \sum_{i \in L} t_i (\hat{a}_0^\dagger \hat{a}_i - \hat{a}_i^\dagger \hat{a}_0) \quad (5.85)$$

where we have (repeatedly) used the fermion anticommutation rules:  $\hat{a}_i^\dagger \hat{a}_j = -\hat{a}_j \hat{a}_i^\dagger$  and  $\hat{a}_i^\dagger \hat{a}_i = 1 - \hat{a}_i \hat{a}_i^\dagger$ , and the last step is because an operator that repeats the same fermionic raising or lowering operator twice in a row is the zero operator (the constraint that fermions only have values of 0 or 1 means that raising or lowering twice tries to take them out of this space.)

When we use our classical mapping for these operators, we obtain the result:

$$\frac{d\hat{N}}{dt} \mapsto - \sum_{i \in L} 2t_i \sqrt{(n_0 - n_0^2 + \lambda)(n_i - n_i^2 + \lambda)} \sin(q_0 - q_i) \quad (5.86)$$

As we see, this is exactly the same as equation (5.76).

#### 5.2.4 Aside: Time Derivative of the Current Operator at $t = 0$

Another calculation which we can do analytically is the time derivative of the current at  $t = 0$  for the Landauer model (the system which we study in detail below). This is very similar

to the derivation from section 5.1.3. Since the current is intimately related to the time derivative of the population variables, its first derivative with respect to time is intimately related to the second derivative of the population variables.

First we consider the time derivative of the (left) current. The classical function for the current is

$$I_L \propto \sum_{k \in L} 2t_k \sqrt{(n_0 - n_0^2 + \lambda)(n_k - n_k^2 + \lambda)} \sin(q_0 - q_k) \quad (5.87)$$

so its time derivative is

$$\dot{I}_L = \frac{\partial I_L}{\partial n_0} \dot{n}_0 + \sum_{k \in L} \frac{\partial I_L}{\partial n_k} \dot{n}_k + \frac{\partial I_L}{\partial q_0} \dot{q}_0 + \sum_{k \in L} \frac{\partial I_L}{\partial q_k} \dot{q}_k \quad (5.88)$$

The time derivatives of the action-angle variables are

$$\dot{n}_0 = \sum_{k \in L} H_{0k} \tan(q_0 - q_k) \quad (5.89)$$

$$\dot{n}_{k \neq 0} = -H_{0k} \tan(q_0 - q_k) \quad (5.90)$$

$$\dot{q}_0 = \epsilon_0 + \sum_{k \in L} \frac{1}{2} \frac{1 - 2n_0}{n_0 - n_0^2 + \lambda} H_{0k} \quad (5.91)$$

$$\dot{q}_{k \neq 0} = \epsilon_k + \frac{1}{2} \frac{1 - 2n_k}{n_k - n_k^2 + \lambda} H_{0k} \quad (5.92)$$

where  $H_{0k} = 2t_k \sqrt{(n_0 - n_0^2 + \lambda)(n_k - n_k^2 + \lambda)} \cos(q_0 - q_k)$ . At  $t = 0$ , where the action variables are all either 0 or 1,  $H_{0k} = 2t_k \lambda \cos(q_0 - q_k)$ , and the time derivatives become

$$\dot{n}_0(t = 0) = 2\lambda \sum_{k \in L} t_k \sin(q_0 - q_k) \quad (5.93)$$

$$\dot{n}_{k \neq 0}(t = 0) = -2\lambda t_k \sin(q_0 - q_k) \quad (5.94)$$

$$\dot{q}_0(t = 0) = \epsilon_0 + \sum_{k \in L} t_k \cos(q_0 - q_k) \quad (5.95)$$

$$\dot{q}_{k \neq 0}(t = 0) = \epsilon_k + t_k (-1)^{n_k} \cos(q_0 - q_k) \quad (5.96)$$

The derivatives of the current with respect to the action-angle variables are

$$\frac{\partial I_L}{\partial n_0} = \sum_{k \in L} \frac{1}{2} \frac{1 - n_0}{n_0 - n_0^2 + \lambda} H_{0k} \tan(q_0 - q_k) \quad (5.97)$$

$$\frac{\partial I_L}{\partial n_{k \neq 0}} = \frac{1}{2} \frac{1 - n_k}{n_k - n_k^2 + \lambda} H_{0k} \tan(q_0 - q_k) \quad (5.98)$$

$$\frac{\partial I_L}{\partial q_0} = \sum_{k \in L} H_{0k} \tan(q_0 - q_k) \quad (5.99)$$

$$\frac{\partial I_L}{\partial q_{k \neq 0}} = -H_{0k} \tan(q_0 - q_k) \quad (5.100)$$

At time  $t = 0$ , these become

$$\frac{\partial I_L}{\partial n_0} \Big|_{t=0} = \sum_{k \in L} t_k \sin(q_0 - q_k) \quad (5.101)$$

$$\frac{\partial I_L}{\partial n_{k \neq 0}} \Big|_{t=0} = (-1)^{n_k} t_k \sin(q_0 - q_k) \quad (5.102)$$

$$\frac{\partial I_L}{\partial q_0} \Big|_{t=0} = 2\lambda \sum_{k \in L} t_k \cos(q_0 - q_k) \quad (5.103)$$

$$\frac{\partial I_L}{\partial q_{k \neq 0}} \Big|_{t=0} = -2\lambda t_k \cos(q_0 - q_k) \quad (5.104)$$

Now we put all the  $t = 0$  partial derivatives together to make the full derivative, per equation (5.88). Since these equations are long, I'll start by treating each term of equation (5.88) separately.

$$\frac{\partial I_L}{\partial n_0} \dot{n}_0 \Big|_{t=0} = \sum_{k \in L} t_k \sin(q_0 - q_k) 2\lambda \sum_{l \in L} t_l \sin(q_0 - q_l) \quad (5.105)$$

$$= 2\lambda \sum_{k \in L} \sum_{l \in L} t_k t_l \sin(q_0 - q_k) \sin(q_0 - q_l) \quad (5.106)$$

$$= 2\lambda \left( \underbrace{\sum_{k \in L} t_k^2 \sin^2(q_0 - q_k)}_{(a)} + \underbrace{\sum_{k \in L} \sum_{l \in L; l \neq k} t_k t_l \sin(q_0 - q_k) \sin(q_0 - q_l)}_{(b)} \right) \quad (5.107)$$

where (a) and (b) are labels which we will use later. Next we look at the contributions from the other actions:

$$\sum_{k \in L} \frac{\partial I_L}{\partial n_k} \dot{n}_k \Big|_{t=0} = \sum_{k \in L} (-1)^{n_k} t_k \sin(q_0 - q_k) (-2\lambda t_k \sin(q_0 - q_k)) \quad (5.108)$$

$$= 2\lambda \left( \underbrace{- \sum_{k \in L} t_k^2 (-1)^{n_k} \sin^2(q_0 - q_k)}_{(c)} \right) \quad (5.109)$$

Now we move on to the contributions to the derivative of the  $t = 0$  Landauer current

from the angles. For the dot mode's angles,

$$\begin{aligned} \frac{\partial I_L}{\partial q_0} \dot{q}_0 \Big|_{t=0} &= 2\lambda \sum_{k \in L} t_k \cos(q_0 - q_k) \left( \epsilon_0 + \sum_{l \in L} t_l \cos(q_0 - q_l) \right) \\ &= 2\lambda \underbrace{\left( \sum_{k \in L} t_k \epsilon_0 \cos(q_0 - q_k) + \sum_{k \in L} t_k^2 \cos^2(q_0 - q_k) \right)}_{(d)} \end{aligned} \quad (5.110)$$

$$+ \underbrace{\sum_{k \in L} \sum_{l \in L; l \neq k} t_k t_l \cos(q_0 - q_k) \cos(q_0 - q_l)}_{(f)} \quad (5.111)$$

Finally, the contributions from the other angles, which are given by

$$\sum_{k \in L} \frac{\partial I_L}{\partial q_k} \dot{q}_k \Big|_{t=0} = \sum_{k \in L} -2\lambda t_k \cos(q_0 - q_k) (\epsilon_k + t_k (-1)^{n_k} \cos(q_0 - q_k)) \quad (5.112)$$

$$= 2\lambda \underbrace{\left( \sum_{k \in L} -t_k \epsilon_k \cos(q_0 - q_k) + \sum_{k \in L} -t_k^2 (-1)^{n_k} \cos^2(q_0 - q_k) \right)}_{(g)} \quad (5.113)$$

The total derivative will be  $2\lambda$  times the sum of the terms labelled (a)-(h) above, averaged over angle variables. Before averaging over angles, we'll recombine the terms above, grouped by in terms of the  $t_j$ 's and  $\epsilon_j$ 's.

First we look at the terms with one  $t_j$  and one  $\epsilon_j$ , *i.e.*, terms (d) and (g). When we add these two together, we get

$$\dot{I}_{dg} = \sum_{k \in L} t_k (\epsilon_0 + \epsilon_k) \cos(q_0 - q_k) \quad (5.114)$$

Since angles  $q_0$  and  $q_k$  are independent at  $t = 0$ , the average over angles will give zero.

Next we look at terms with two different values of  $t_j$  in the sum, *i.e.*, terms (b) and (f):

$$\dot{I}_{bf} = \sum_{k \in L} \sum_{l \in L; l \neq k} t_k t_l (\sin(q_0 - q_k) \sin(q_0 - q_l) + \cos(q_0 - q_k) \cos(q_0 - q_l)) \quad (5.115)$$

Since  $k$  and  $l$  can never be the same, we can do the average independently for  $q_k$  and  $q_l$  with a fixed  $q_0$ . For any value of  $q_0$ , the averages over  $q_k$  and  $q_l$  give us zero, and therefore the total average gives us zero. Terms (b) and (f) contribute zero to the overall derivative of the current.

Since these first two parts contribute nothing to the time derivative of the current, the current is entirely determined by the remaining four terms, which all have a factor of  $t_k^2$ . Combined,

they give

$$\dot{I}_{\text{aceh}} = \sum_{k \in L} t_k^2 (\sin^2(q_0 - q_k) - (-1)^{n_k} \sin^2(q_0 - q_k) + \cos^2(q_0 - q_k) - (-1)^{n_k} \cos^2(q_0 - q_k)) \quad (5.116)$$

$$= \sum_{k \in L} t_k^2 (1 - (-1)^{n_k}) (\sin^2(q_0 - q_k) + \cos^2(q_0 - q_k)) \quad (5.117)$$

$$= \sum_{k \in L} t_k^2 (1 - (-1)^{n_k}) \quad (5.118)$$

So the total current is

$$\dot{I}_L = 2\lambda \sum_{k \in L} t_k^2 (1 - (-1)^{n_k}) \quad (5.119)$$

Typically, the spectral density of the electrodes is selected to represent the wide-band limit. That is, it is nearly flat at some value  $\Gamma$  with two sharp cutoffs outside of which it is (near) zero. If we take this approximation, then we can say that  $t_k = t$  inside the band, and  $t_k = 0$  outside. Obviously, if  $t_k = 0$  we have no contribution to the time derivative of the current, so we assume that we only have states within the band. Within this approximation, our uniform sampling of electrode energy levels gives  $t$  according to

$$t^2 = \frac{\Gamma_L B}{2\pi N_L} \quad (5.120)$$

where  $B$  is the width of the band and  $N_L$  is the number of states in the left lead. Within this approximation, we can write the time derivative of the left current as

$$\dot{I}_L = 2\lambda \sum_{k \in L} t^2 (1 - (-1)^{n_k}) \quad (5.121)$$

$$= \frac{\lambda \Gamma_L B}{\pi} \sum_{k \in L} \frac{1 - (-1)^{n_k}}{N_L} \quad (5.122)$$

Since the function  $1 - (-1)^{n_k}$  gives 0 if state  $k$  is not occupied and 2 if state  $k$  is occupied, the sum over all states  $k$  will be twice the number of occupied states. When this is divided by  $N_L$ , the total number of states in the left lead, it gives us twice  $f_{\text{occ}}^L$ , the fraction of states in the left electrode which are occupied. Therefore, the final result for the  $t = 0$  current is

$$\dot{I}_L(t = 0) = \frac{2}{\pi} \lambda \Gamma_L B f_{\text{occ}}^L \quad (5.123)$$

At long time, the total current reaches a steady state (*i.e.*, the population of the dot no longer changes). At this point, the total current equals the left current, and is equal and opposite to the right current.

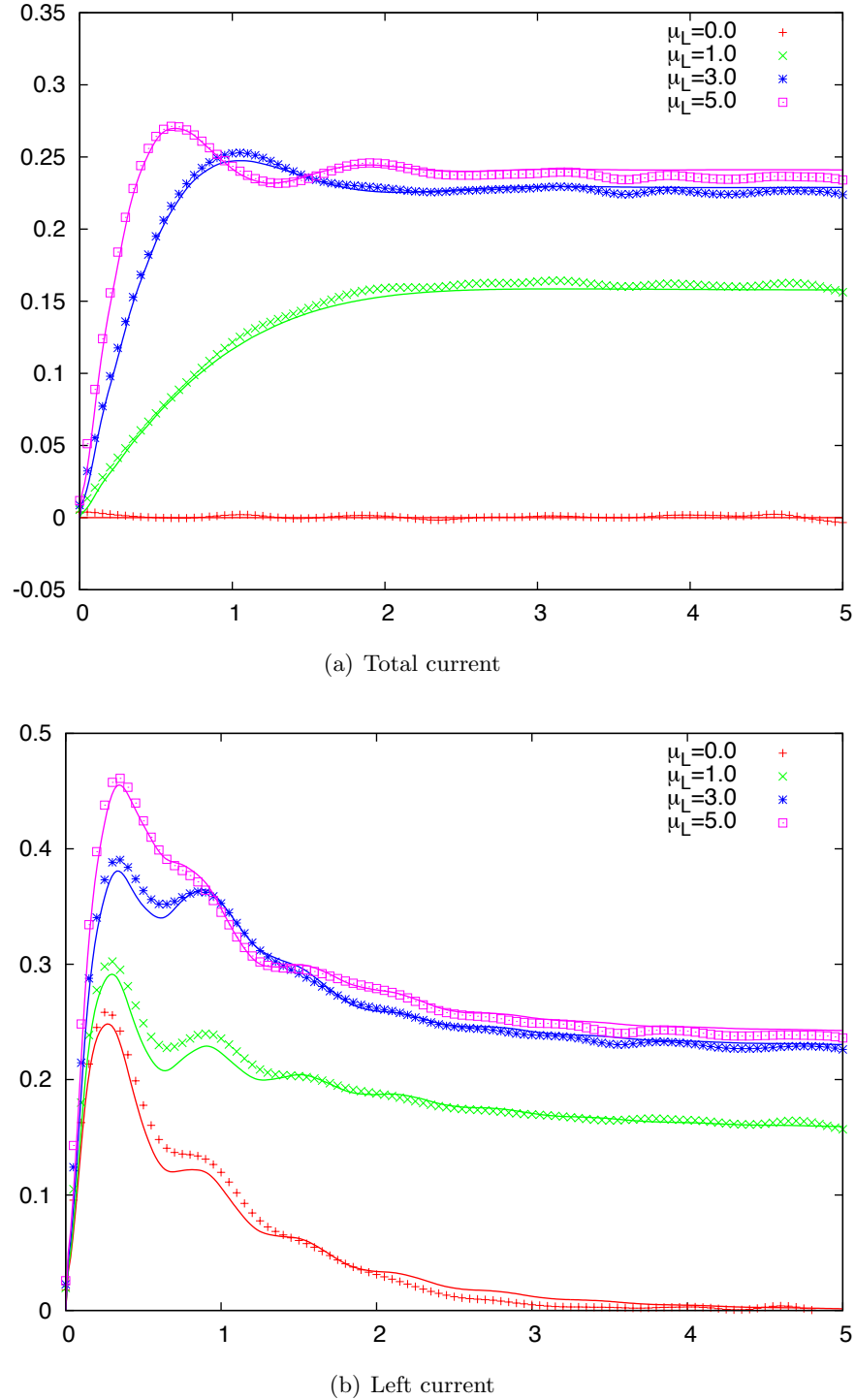


Figure 5.3: Results for different values of the source-drain voltage (where  $eV = 2\mu_L = \mu_L - \mu_R$ ). Inverse temperature is  $\beta = 3.0$ . All numbers are in units of  $\Gamma$ .

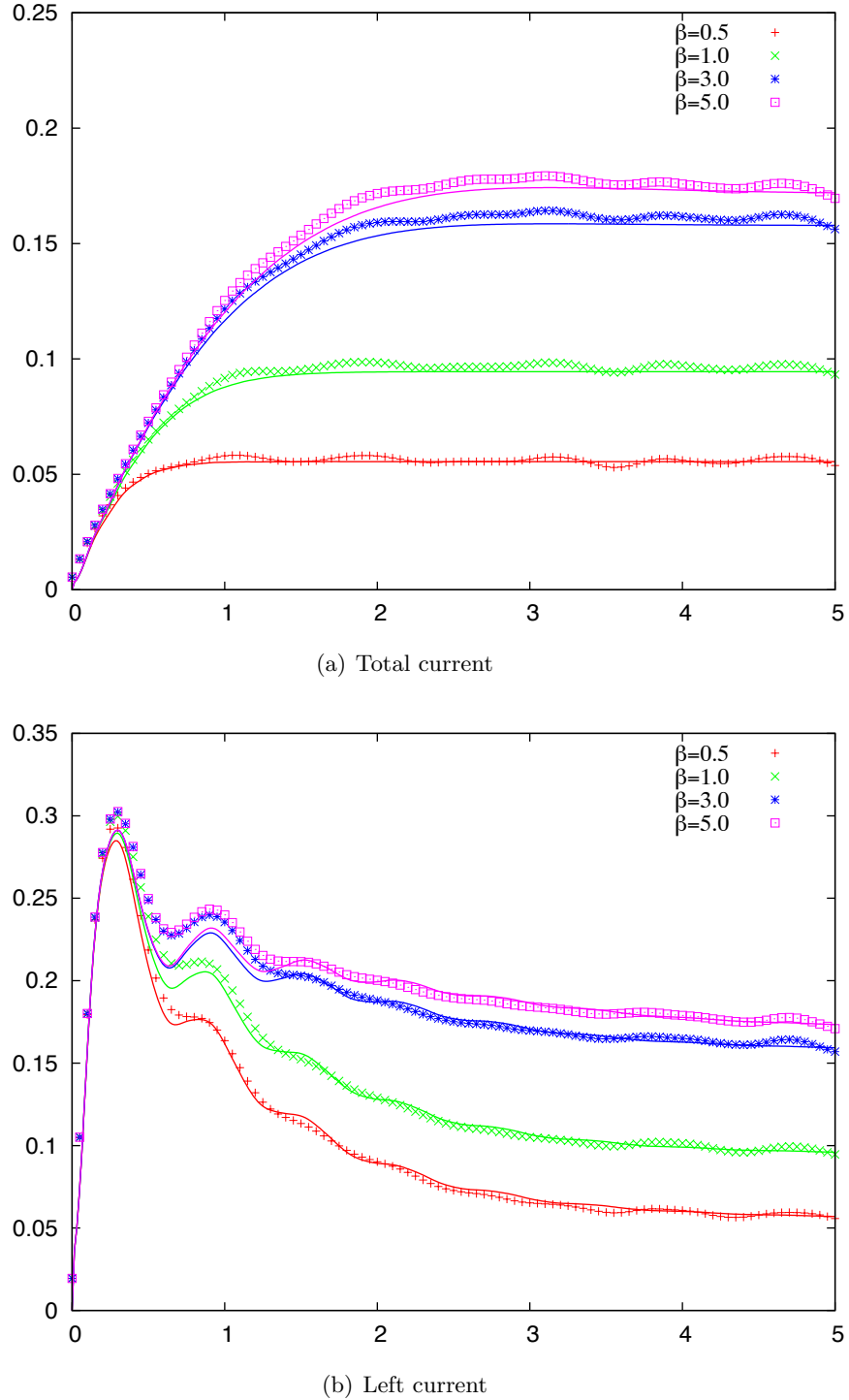


Figure 5.4: Results for different values of the temperature (presented as the inverse temperature  $\beta$  in units of  $\Gamma$ ). The bias is  $\mu_L = -\mu_R = 1.0$ .

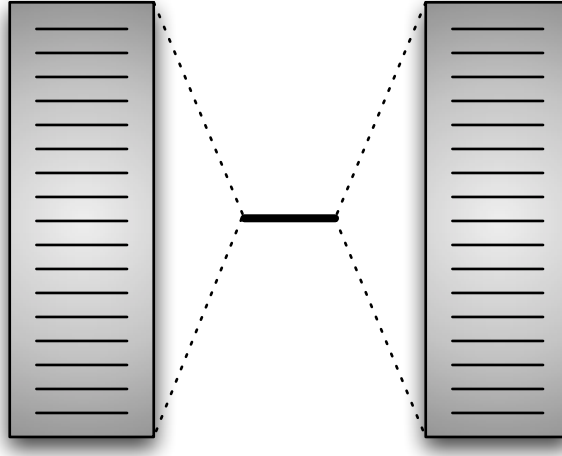


Figure 5.5: Cartoon of the Landauer (resonant-level) problem. A single quantum dot (center) is coupled to two baths, left and right. While the baths are formally continuous, we add the lines to represent the fact that in our semiclassical simulations we discretize the electrodes.

### 5.3 The Landauer Problem: A Test System

In order to develop, debug, and test this method, we start with the Landauer Hamiltonian:

$$\hat{H} = \sum_{i=0}^N \epsilon_i \hat{a}_i^\dagger \hat{a}_i + \sum_{k=1}^{N_L} t_k (\hat{a}_0^\dagger \hat{a}_i + \hat{a}_i^\dagger \hat{a}_0) + \sum_{k=N_L+1}^{N_L+N_R} t_k (\hat{a}_0^\dagger \hat{a}_i + \hat{a}_i^\dagger \hat{a}_0) \quad (5.124)$$

The idea here is illustrated in figure 5.5: we have one mode of the system, a “quantum dot,” sandwiched between two electrode baths. The dot is labelled as mode 0; the left bath is labeled with modes 1 through  $N_L$ , and the right bath is labeled with modes  $N_L + 1$  through  $N_L + N_R$ . Part of the interest in this system is that it can be solved analytically. Therefore, we are able to compare our semiclassical results to exact quantum results.

In our tests, we take the baths as displaced by a voltage  $\mu_L$  and  $\mu_R$ . The dot begins empty, and the baths are occupied thermally according to the method described in section 5.2.2.

Applying the mapping from equation (5.15), we obtain the semiclassical Hamiltonian

$$\begin{aligned} H = & \epsilon_0 n_0 + \sum_{k \in L} n_k + \sum_{k \in R} n_k + \sum_{k \in L} \sqrt{(n_0 - n_0^2 + \lambda)(n_k - n_k^2 + \lambda)} \cos(q_0 - q_0) \\ & + \sum_{k \in R} \sqrt{(n_0 - n_0^2 + \lambda)(n_k - n_k^2 + \lambda)} \cos(q_0 - q_0) \end{aligned} \quad (5.125)$$

which we use with Hamilton’s equations of motion to time-evolve the system. The numerical integration was performed with the sixth-order Gear predictor-corrector algorithm. Occasionally, the prediction step can move an action to a point where the radicand becomes negative. To avoid this, we modified the Gear predictor-corrector to include an adaptive timestep, while still hitting

the milestones which are necessary to average across trajectories. The details of these changes to the integrator are presented in appendix B. The maximum allowed timestep is  $0.01\hbar/\Gamma$ . When not otherwise stated, all of the results presented in this section are with bias  $\mu_L = -\mu_R = \Gamma$ , temperature  $T = \Gamma/3$ , gate voltage  $e_0 = 0$ , 400 modes per electrode, and 200000 trajectories. As discussed above, we use the book-keeping function  $f_b(n) = 1$  and the quantum length of the spin vector, giving  $\lambda = 0.5$ .

In figures 5.3, 5.4, and 5.6, we show the effect of various system parameters on the results of the time dependent current. Each of these figures shows both the total current and the left current. Although we can calculate the right current (indeed, we use it to obtain the total current) we do not show it here because the information it presents is redundant.

In many of the figures we observe oscillations, which are especially pronounced in the left current (and which are cancelled by similar oscillations in the right current). These result from the finite band width of the electrodes, and our semiclassical method also captures this effect.

In figure 5.3, we compare the semiclassical method to the exact quantum results for different values of the chemical potential (voltage bias). In these results, the energy of the quantum dot (the gate voltage) is kept at zero, and the chemical potential of the electrodes are equal and opposite. The bias is therefore twice the chemical potential in the left lead (which we have chosen to have a positive chemical potential). In figure 5.3(a) we see the total current for different choices of the bias. For all of them, we have quantitative agreement with the exact quantum results. The highest total bias we explored,  $eV = 10\Gamma$  (or  $\mu_L = 5\Gamma$ ) starts to get close to the limit of what we can do with our finite band width of  $B = 20$ . The steady state with  $\mu_L = 5\Gamma$  is  $I = 0.241\Gamma$ , which is already approaching the infinite bias limit of  $I = 0.25\Gamma$ .

In figure 5.3(b) we have just the left current for the different values of the bias. Whereas the total current for  $\mu_L = 0$  is completely flat (to within numerical noise), the left current shows a marked transient current. This corresponds to the (initially empty) quantum dot coming to equilibrium. The oscillations in the transient of the left current are captured qualitatively for all biases, but lower biases don't capture the results quite as quantitatively. However, a mirror effect occurs in the right current. This results in the total current providing extremely good agreement.

Figure 5.4 shows the effect of different (inverse) temperatures on the current. The temperatures studied range from  $T = \Gamma/5$  to  $T = 2\Gamma$ , which goes from the quantum regime to the classical regime. The semiclassical method performs very well at all temperatures, both for the total current and for the left current. When we look at figure 5.4(a) carefully, we can see that the semiclassical method performs a little bit better for higher temperatures than for lower temperatures. This is to be expected, since the classical limit for temperature is the high-temperature regime. In fact, it is remarkable that this method performs as well as it does as low temperatures.

However, as we go to lower temperature, the intermediate-time oscillations in the left current, seen in figure 5.4(b) (which are essentially cancelled in the total current by similar oscillations from the right current), become less accurate at lower temperatures. At all temperatures, the semiclassical method captures the qualitative behavior, but the quantitative agreement gets worse. However, at longer times (as the current approaches steady-state) the semiclassical method returns to near-quantitative accuracy. Furthermore, the similar error in the right current means that we don't see these intermediate-time errors in the total current.

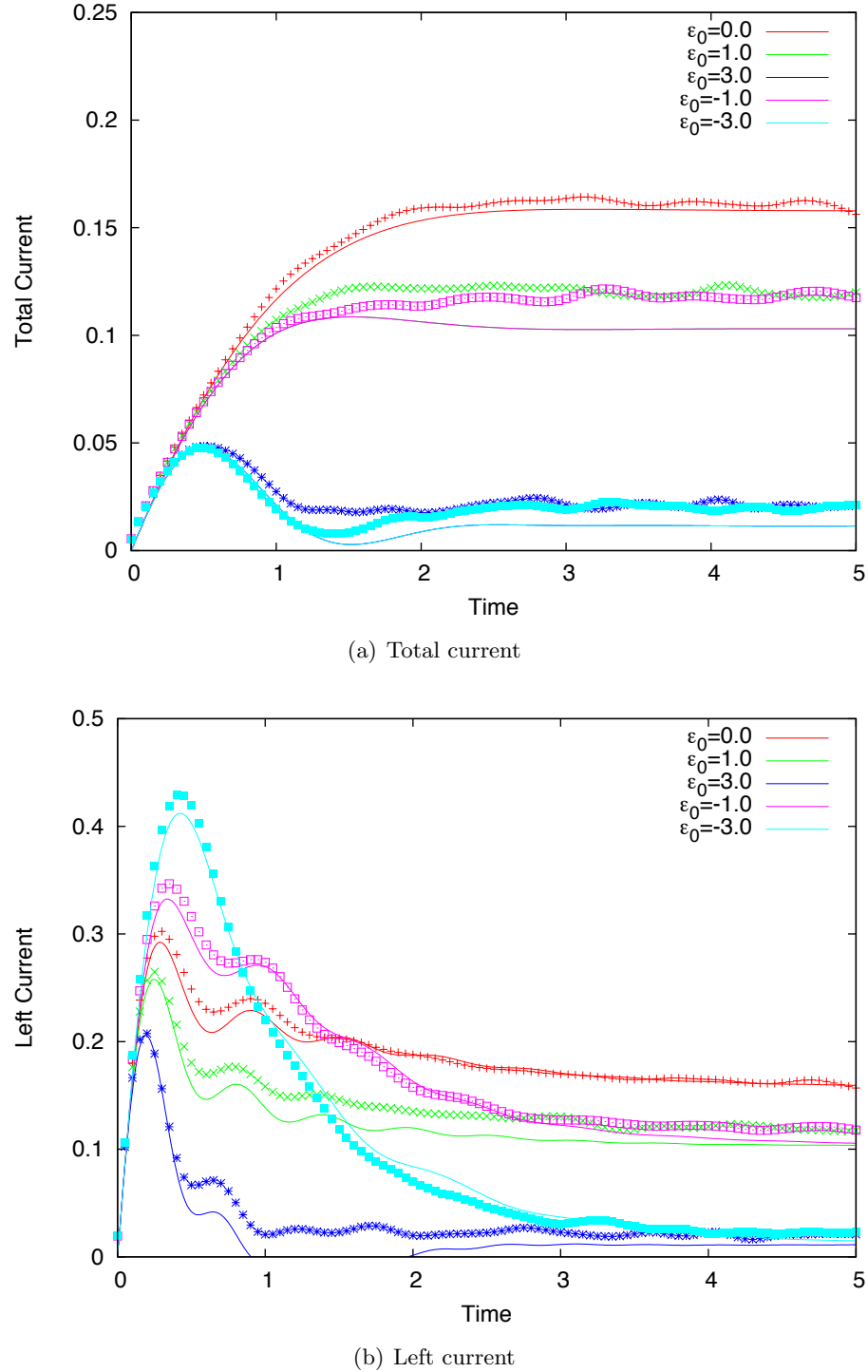


Figure 5.6: Effect of different gate voltages on the time-dependent current. The bias is  $\mu_L = -\mu_R = \Gamma$  and the temperature is  $T = \Gamma/3$ .

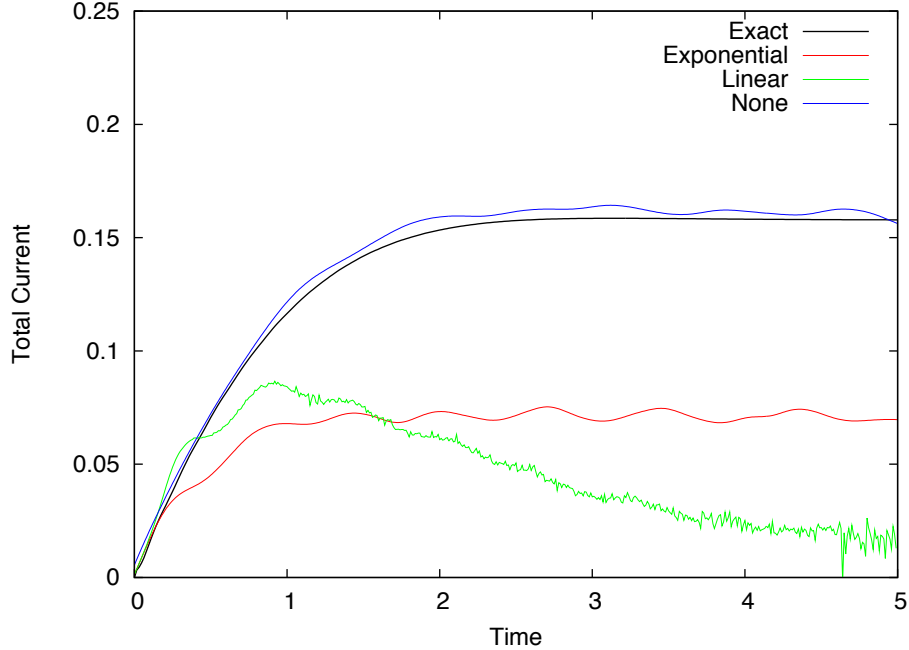


Figure 5.7: Effect of different choices of the book-keeping function  $f_b(n)$  on the time-dependent total current at temperature  $T = \Gamma/3$ , gate voltage  $\epsilon_0 = 0$ , and bias  $\mu_L = -\mu_R = \Gamma$ .

In figure 5.6 we see that we have slightly less success when we vary the gate voltage. In our model, the gate voltage  $eV_G$  is represented by the energy of the quantum dot,  $\epsilon_0$ . Although our results are less accurate when  $eV_G \neq 0$ , we still capture the trends in the currents, as well as the qualitative behavior at all times. In figure 5.6(b) we see that the semiclassical method even qualitatively captures the more pronounced oscillations in the left current. As we see in figure 5.6(a), the total current for equal and opposite gate voltages are equal at all times. In the semiclassical case, the steady-state currents for equal and opposite gate voltages are equal (within numerical noise), although the semiclassical steady-state current does not equal the exact quantum steady-state current. Both the left current and the right current have errors of the same magnitude in the steady-state current, but these errors combine to create a larger error in the total current.

Figures 5.7–5.10 justify various choices we made in simulation details, and highlight some of the details to which one must attend for these calculations. We start with our choice of the book-keeping function  $f_b(n) = 1$ . This choice, which we label as “None,” is shown in figure 5.7, along with the other options we explored:  $f_b(n) = e^{-i\pi n}$  (“Exponential”), and  $f_b(n) = 1 - 2n$  (“Linear”). For all of these we use  $\lambda = \frac{1}{2}$ , which gives us the correct short-time behavior, and 400 modes per electrode. The plot is for the resonant-level model at  $T = \Gamma/3$ ,  $\epsilon_0 = 0$ , and  $\mu_L = -\mu_R = \Gamma$ . The exponential method reaches a steady state, but it vastly underestimates the steady-state current. It also shows much more pronounced oscillations than the result with  $f_b(n) = 1$ . The linear method doesn’t even show a correct approach to steady state. The curve

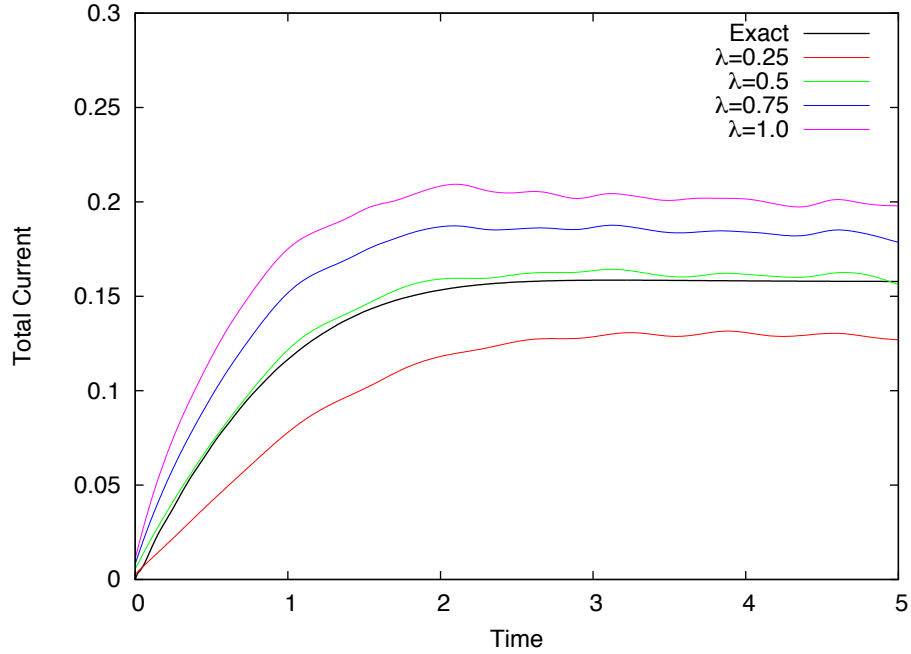


Figure 5.8: Effect of different values of  $\lambda$  (or equivalently, different choices for the length of the spin vector) on the time-dependent total current at temperature  $T = \Gamma/3$ , gate voltage  $\epsilon_0 = 0$ , and bias  $\mu_L = -\mu_R = \Gamma$ .

for the linear method is also very noisy, which probably results from the fact that the calculation is very difficult. Trajectories calculated with the linear book-keeping method occasionally fall into regions where the adaptive timestep algorithm must find extremely small steps, costing lots of computer time. As a practical matter, obtaining 200000 trajectories for this system requires running the calculation from many initial seeds, each of which contributes (on average) a few thousand trajectories before hitting one that requires too many tiny steps to complete.

In figure 5.8 we show the effect that different choices of the length of the vector in the SMM method has on the current in the Landauer model. The results are reported in terms of  $\lambda = \sigma^2 - \frac{1}{4}$ , where  $\sigma$  is the length of the spin vector. For the spin  $\frac{1}{2}$  system, we have  $s = \frac{1}{2}$ . Using the quantum choice for the vector length,  $\sigma^2 = s(s+1) = \frac{3}{4}$ , or  $\lambda = \frac{1}{2}$ . The Langer-modified version gives  $\sigma^2 = (s + \frac{1}{2})^2 = 1$ , of  $\lambda = \frac{3}{4}$ . In the spirit of Stock's treatment of the Langer modification as a free parameter,<sup>62</sup> we also show the results for  $\lambda = 1$  and  $\lambda = \frac{1}{4}$ , the latter being near Stock's result of 0.3125 (for a different system). As we saw from the short-time analysis of the time-dependent left current in section 5.2.4, the slope of the current at short time is proportional to  $\lambda$ . Regardless of the value of  $\lambda$ , the total current seems to reach a steady state after approximately the same amount of time. However, the value of that steady-state current grows with the value of  $\lambda$ . The larger initial slope gives a kind of “running start” to the current and it overshoots or undershoots the correct steady state for values of  $\lambda$  far from  $\lambda = \frac{1}{2}$ , which corresponds to the quantum choice of vector length, matches our short-time analysis for

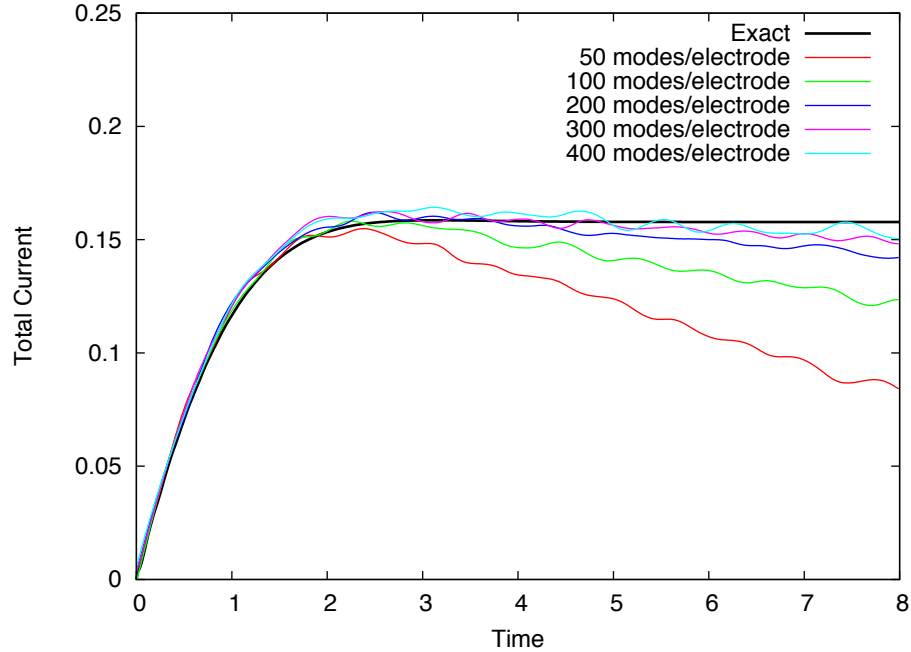


Figure 5.9: Result of different numbers of modes per electrode on the time-dependent total current at temperature  $T = \Gamma/3$ , gate voltage  $\epsilon_0 = 0$ , and bias  $\mu_L = -\mu_R = \Gamma$ .

the two-state system in section 5.1.3, and gives results which match the exact results.

Figure 5.9 highlights the necessity of including enough modes in the discretization of the electrodes. The steady state reached by this simulation is actually a pseudo-steady state. Due to the finite number of modes in the bath (and therefore the finite initial population of electrons), at long time the left electrode becomes depleted and the flow of electrons slows, *i.e.*, the current drops. Figure 5.9 shows that as we add more modes to the electrodes, we hold the steady state to longer time. If we have only 50 modes, we don't even hold the steady state long enough to recognize it. All the other calculations presented here use 400 modes per electrode, which figure 5.9 suggests holds the steady state until at least  $t = 5\hbar/\Gamma$ .

The convergence of this calculation with respect to trajectories is shown in figure 5.10. The qualitative behavior (and a rough estimate of the quantitative results) are evident with only 24000 trajectories. All the other results presented here involved at least 200000 trajectories.

In addition to being accurate, this semiclassical calculation is quite efficient. This particular system is relatively simple, since, as can be seen from the semiclassical Hamiltonian (5.125), it scales linearly with the number of degrees of freedom. A calculation to time  $t = 8\hbar/\Gamma$  with 400 modes per electrode and 200000 trajectories required less than one hour of walltime with 120 computational cores. The approximate results obtained with 24000 trajectories are therefore within the reach of even a single desktop computer.

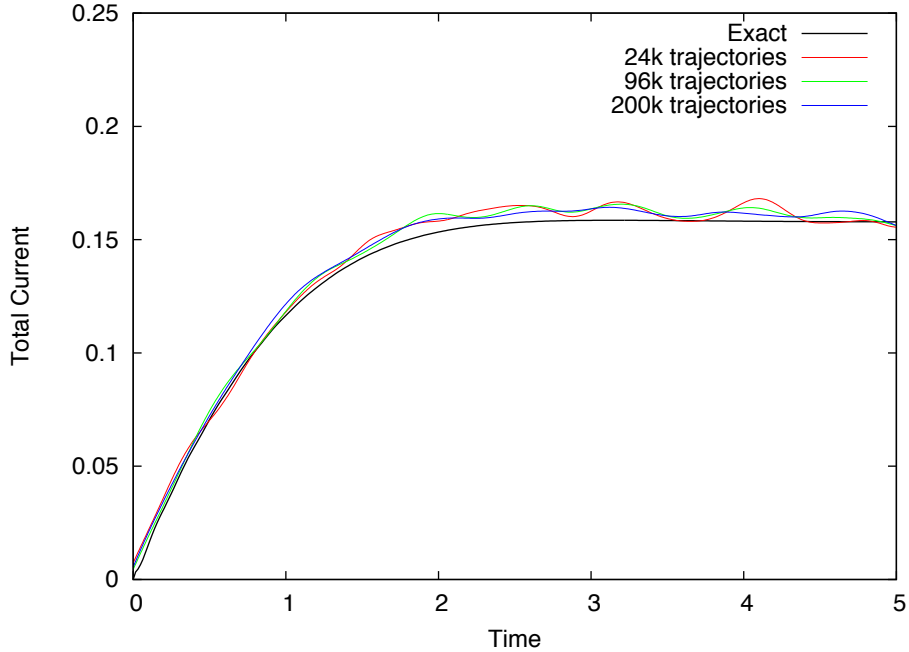


Figure 5.10: Convergence of the time-dependent total current with respect to the number of trajectories, for the system parameters of temperature  $T = \Gamma/3$ , gate voltage  $\epsilon_0 = 0$ , and bias  $\mu_L = -\mu_R = \Gamma$ .

## 5.4 Future Directions

Our results for the Landauer model were extremely successful, and this encourages us to see what else this methodology might be able to describe. The obvious next step is to start including electron correlation. This corresponds to terms which are higher than quadratic in the creation/annihilation operators. The first term to explore would be  $\hat{a}_i^\dagger \hat{a}_j^\dagger \hat{a}_j \hat{a}_i$ , which the SMM procedure maps to the function  $n_i n_j$  in action-angle variables.

In the context of molecular conduction, this term is known as the “Anderson impurity,” and leads to the Coulomb blockade and (at low temperatures) to the Kondo effect. Work is currently under way to study whether we can capture the physics associated with adding this term.

Another direction we can go is to add an interaction to bosons. Typically, this is done by adding a phonon bath, which represents the vibrational environment in which the molecular junction finds itself. We also plan to explore this.

More generally, coupling the electronic behavior to nuclear motion should be relatively easy in this system. This is the great advantage of taking the quantum behavior and converting it into a classical model: now the motion of the nuclei, which are well described by semiclassical (or even classical) dynamics, are automatically treated on the same footing as the very quantum mechanical electronic behavior.

Although the work presented here has been shown in the context of molecular electronics,

it actually provides a general treatment of a second-quantized Hamiltonian. As such, there are many other avenues of research available. One direction which is currently under exploration is an idea to use this as the basis for a semiclassical electronic structure method. Certainly, if we find that we are able to accurately capture the physics from higher order terms, it is likely that many other problems can be approached using this method.

# Concluding Thoughts

This document has covered a veritable plethora of ideas, calculations, and derivations related to semiclassical dynamics. To crystallize it into a single sentence, I would say this: Classical dynamics can be used as the underlying tool in the approximation of nearly all quantum mechanical effects.

Of course, the accuracy of that approximation depends on many factors. Yet, as we have seen, proper semiclassical methods can give quantitative treatment of quantum dynamical interferences, and even fermionic systems can be simulated by the appropriate classical dynamics.

Once we accept that these semiclassical tools can be useful as an approximate treatment of quantum dynamics, we would like to show that they can be efficient. In chapter 2, we showed that using a Monte Carlo method that involved time-dependent information could be much more efficient than one which only used time-independent information.

In chapter 3 we explored an idea not unlike the idea in chapter 2. In this case, we separated the phase from the magnitude by writing the semiclassical calculation as a phase histogram. While our efforts to fit a sum of Gaussians to the phase histogram did not make the calculation more efficient, the phase histograms themselves provided an interesting perspective on the source of quantum interference effects.

In chapter 4 we presented a new method for calculating the monodromy matrix (and thus the semiclassical prefactor), which has been one of the bottlenecks to semiclassical calculations. In terms of describing how chapter 4 fits into the whole of this work, it is worth noting that it is completely orthogonal from all other aspects. That is, it can be used in connection with the improved methods of chapter 2 or those of chapter 3: neither precludes a novel treatment of the semiclassical prefactor.

Finally, chapter 5 represents a break from the earlier chapters. The methodology developed is notably different from those presented earlier. Instead of focusing on nuclear dynamics, we focus on the dynamics of the electrons. Instead of using semiclassical methods to define the distributions at various times, we use a quasiclassical approach, forcing the  $t = 0$  statistics to match the quantum results and then allowing the dynamics to evolve according to the semiclassical Hamiltonian. While this method isn't as rigorous (or internally consistent) as the approach used in the other chapters, it represents a first attempt to apply this sort of semiclassical Hamiltonian to a practical problem.

As all good science should, many of these chapters ended with more questions unanswered than answered. Chapter 2 closes with another system to study, and an idea for a way use the basic methodology to generate an even more efficient algorithm for estimating SC-IVR calculations.

Chapter 3 notes that, although the Gaussian fitting idea failed, there seems to be a lot of structure to the phase histograms which a clever algorithm might use to its advantage. Chapter 4 leaves us with more systems to try, and questions about why the periodic trajectories caused problems for the precision finite difference method. Even at the end of chapter 5 we're left with many systems we would like to test, and methodologies which can use the techniques described herein for a wider variety of systems.

Semiclassical theory has proven itself as a practical method for simulations. It can capture quantum mechanical effects efficiently, and in this dissertation I have presented ideas which have both made it more efficient and which have broadened the range of problems which we have addressed semiclassically. Several chapters have even shown how semiclassical calculations can be used to provide insights on the nature of quantum mechanical effects.

The dream of using classical methods to describe quantum mechanics, which is nearly as old as quantum mechanics itself, becomes more and more of a reality as refinements such as these are developed.

## Appendix A

# Model Systems

As a practical matter, several model systems were frequently revisited in the process of developing the methodologies described in this text. This appendix looks at two in particular. For the harmonic oscillator, we present various analytical formulae for reference purposes. For the anharmonic Morse oscillator, we show how various parts of the calculation contribute to the total survival amplitude (and how the failure to capture certain results indicate the failure to describe certain parts of the physics).

### A.1 Harmonic Oscillator

The harmonic oscillator is one of the most useful model systems. Beyond its usefulness as a first approximation to any well on a potential energy landscape, it can be solved analytically both quantum mechanically and classically. The fact that it has an analytical classical solution means that it usually has an analytical semiclassical solution as well.

In addition, most semiclassical theories are exact for the harmonic oscillator. This is because, as discussed in chapter 1, SC-IVR approximations to the propagator are based on a second-order Taylor expansion of the potential as it appears in action exponential from the Feynman path integral. Of course, this second-order expansion is exact for the harmonic oscillator.

One of the uses of the harmonic oscillator as a model system is that, being exactly solvable, it can be used as an analytical tool for new methods. When either sanity-checking a new approximation or debugging new code, the analytical results from the harmonic oscillator can be useful.

The harmonic oscillator Hamiltonian  $H = \frac{p^2}{2m} + \frac{1}{2}m\omega^2q^2$  can be easily solved from Hamilton's equations:

$$\frac{\partial H}{\partial p} = \dot{q} = \frac{p}{m} \tag{A.1}$$

$$-\frac{\partial H}{\partial q} = \dot{p} = -m\omega^2q \tag{A.2}$$

Multiplying the first equation by  $m$  and taking a second time derivative, we're left with:

$$m\ddot{q} = -m\omega^2q \tag{A.3}$$

Quantity	Harmonic Oscillator Expression
Position	$q(t) = q_0 \cos(\omega t) + \frac{p_0}{m\omega} \sin(\omega t)$
Momentum	$p(t) = p_0 \cos(\omega t) - m\omega q_0 \sin(\omega t)$
Action	$S(t) = \frac{1}{4} \left( \frac{p_0^2}{m\omega} - m\omega q_0^2 \right) \sin(2\omega t)$
Monodromy Elements	$M_{qq} = M_{pp} = \cos(\omega t),$ $M_{qp} = \frac{1}{m\omega} \sin(\omega t), M_{pq} = -m\omega \sin(\omega t)$
Herman-Kluk Prefactor ( $\gamma = m\omega$ )	$\mathcal{C}_t^{\text{HK}} = e^{-i\omega t/2}$

Table A.1: Analytical results for the classical harmonic oscillator.

The general solution to this differential equation is  $q(t) = A \cos(\omega t) + B \sin(\omega t)$ . We can solve for the constants  $A$  and  $B$  by defining the initial conditions  $q(0) = q_0$  and  $p(0) = p_0$  (and using the fact that  $p = m\dot{q}$ ). The result is that the position is given by:

$$q(t) = q_0 \cos(\omega t) + \frac{p_0}{m\omega} \sin(\omega t) \quad (\text{A.4})$$

From this, we can obtain all the other results for classical quantities which enter into a semiclassical calculation, many of which are listed in table A.1.

## A.2 Anharmonic Morse Oscillator

One of my personal favorite systems, which is used throughout this thesis, is a specific anharmonic Morse oscillator which starts from a squeezed state. The reader will note a lack of units in this section: this is because the anharmonic Morse oscillator is not intended to represent a real physical system. It is treated with  $\hbar = 1$ , but beyond that the units have no meaning.

The potential energy for this system is given by

$$V(q) = 30.0 \left( 1 + (1 - e^{-0.08q})^2 \right) \quad (\text{A.5})$$

and the initial wavepacket has the position-space representation

$$\langle q | \psi \rangle = \left( \frac{12}{\pi} \right)^{1/4} e^{-6q^2 + ipq} \quad (\text{A.6})$$

This gives us a very narrow wavepacket at the bottom of the potential well. Using unit mass for the particle, the harmonic frequency of this system is 0.30984. This potential, its initial wavepacket, and an outline of its harmonic-width Gaussian are illustrated in figure A.1.

The potential is offset so that the bottom of the well is at zero. This highlights an issue that I have called the “semiclassical gauge” problem. When looking at quantities which are not Hermitian (such as the real part of the survival amplitude), the choice of the zero of energy is not

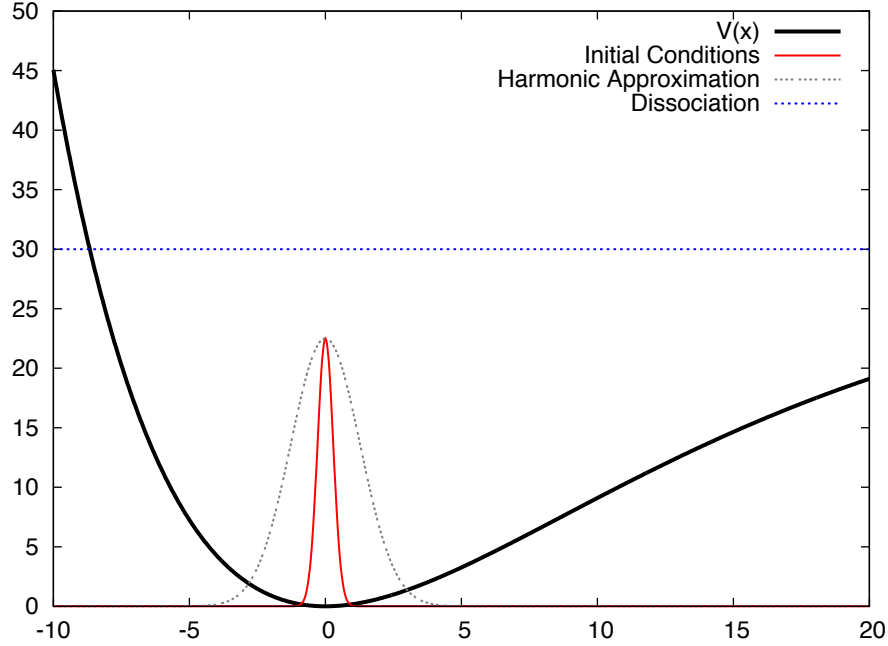


Figure A.1: Potential, initial wavepacket, and harmonic-width wavepacket for the anharmonic Morse oscillator.

arbitrary. The action integral is given by

$$S(t) = \int_0^t dt' \mathcal{L}(t') - \Delta E \quad (\text{A.7})$$

$$= -t\Delta E + \int_0^t dt' \mathcal{L}(t') \quad (\text{A.8})$$

This means that each trajectory has an additional phase of  $e^{-it\Delta E}$  associated with it, which changes the single-propagator results (see figure A.2 for an example of the effect of the semiclassical gauge problem). This is no longer a problem for multiple propagator methods, since the reverse propagator will contribute a phase of equal and opposite value for every time and for any trajectory.

Figure A.1 shows the position-space representation of the initial wavepacket. But since its width in position is very small, its width in momentum is relatively large. The standard deviation in momentum of the sampling function  $|\langle \Omega_0 | \psi \rangle|^2$  is  $\sqrt{12} \approx 3.46$ . Since the dissociation energy is 30.0 (and we have unit mass) any trajectory with momentum above 5.48 will dissociate. That's makes anything more than 1.5 standard deviations from the mean dissociative based on internal kinetic energy alone. And since the potential energy surface is positive definite, the potential energy contribution can only increase the energy.

Therefore a good number of trajectories will dissociate. This also means that the Grossman Morse can catch problems that occur in the imaginary frequency regime.

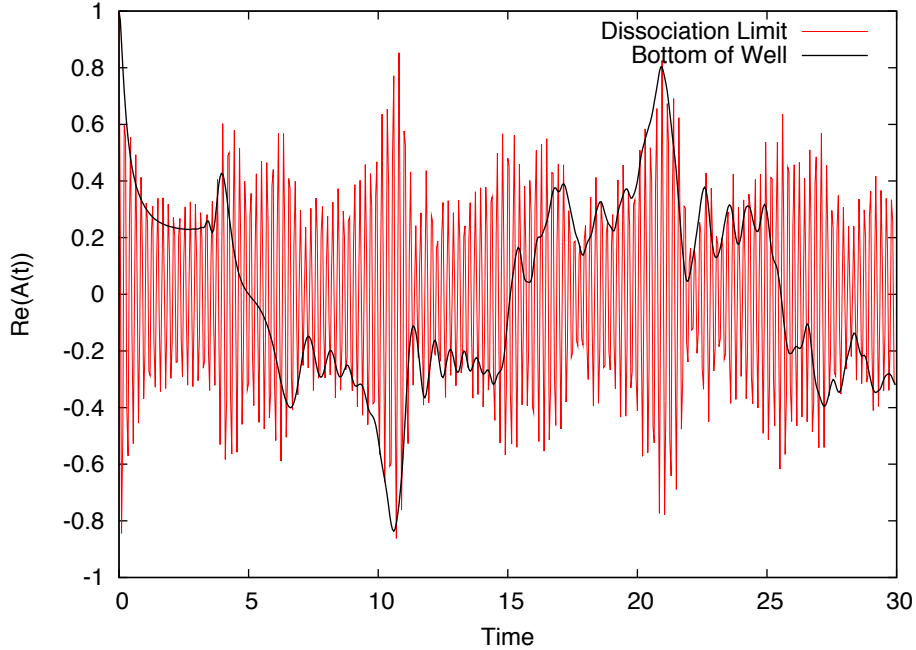


Figure A.2: The “semiclassical gauge” problem: the real part of the survival amplitude for the anharmonic Morse oscillator with the zero of energy at the bottom of the well versus at the dissociation limit.

The quantity which we typically calculate for this system is the survival amplitude,  $\mathcal{A}(t)$ . The survival amplitude is a useful quantity because it can be calculated with relative ease by any of the semiclassical methods available to us. Its most obvious definition is as a single-propagator calculation:

$$\mathcal{A}(t) = \left| \langle \psi | e^{-i\hat{H}t} | \psi \rangle \right| \quad (\text{A.9})$$

Of course, the modulus is just the square root of the modulus-squared, so we can write this in terms of a correlation function (suitable to be calculated by LSC-IVR or DHK-IVR) as follows:

$$\mathcal{A}(t) = \sqrt{\langle \psi | e^{-i\hat{H}t} | \psi \rangle^* \langle \psi | e^{-i\hat{H}t} | \psi \rangle} \quad (\text{A.10})$$

$$= \sqrt{\langle \psi | e^{i\hat{H}t} | \psi \rangle \langle \psi | e^{-i\hat{H}t} | \psi \rangle} \quad (\text{A.11})$$

$$= \sqrt{\text{Tr}(\langle \psi | e^{i\hat{H}t} | \psi \rangle \langle \psi | e^{-i\hat{H}t} | \psi \rangle)} \quad (\text{A.12})$$

$$= \sqrt{\text{Tr}(|\psi\rangle \langle \psi| e^{i\hat{H}t} |\psi\rangle \langle \psi| e^{-i\hat{H}t})} \quad (\text{A.13})$$

A useful aspect of the survival amplitude for this system is that different features from the plot correspond to different parts of the semiclassical expression. Therefore, a glance at the

survival amplitude can identify what physics are and are not being captured when testing a new method.

In figure A.3(a), we look at what happens with different treatments of the prefactor. In addition to looking at the full HK-IVR, the LSC-IVR, the result of “turning off” the prefactor (unit prefactor), we look at a phase-only approximation to the prefactor, given by<sup>64</sup>

$$c_t^{\text{HK}} \approx \exp \left( -\frac{i}{2} \int_0^t dt' \sum_j \omega_j(t') \right) \quad (\text{A.14})$$

where the set of  $\{\omega_j(t')\}$  are the square roots of the eigenvalues of the Hessian at time  $t'$ . We refer to this method as the “local harmonic prefactor,”\* because it essentially makes the harmonic approximation at each point along the trajectory. As one would expect, this approximation gives the exact result for the harmonic oscillator (as is easily verified by comparing with table A.1). If we look a little closer, we note that this version captures some part of the phase of the prefactor, but ignores everything related to its amplitude. This partial capture of the phase is what differentiates it from the unit prefactor, which is equivalent to ignoring the prefactor altogether.

Now we look at figure A.3(a). The first thing we note is that removing the magnitude of the prefactor, either by completely ignoring the prefactor (unit prefactor) or by only including the phase (local harmonic prefactor), the magnitude of the survival amplitude rapidly becomes too small. This is because the prefactor plays an important role in the normalization of semiclassical wavefunction. Although it isn’t immediately apparent from the expression for the LSC-IVR that it contains the prefactor (or at least enough of the prefactor to retain normalization as well as it does) we should remember that the (Van Vleck) prefactor is removed from the equation due to a change of variables (meaning that, in some sense, it is still included).

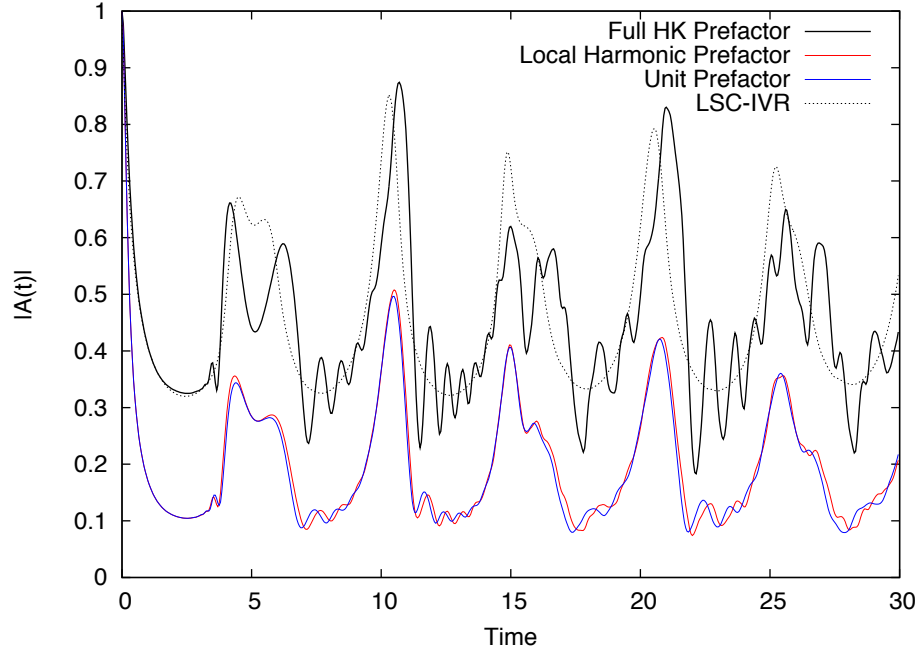
Even without normalization, we note that most of the features of the survival amplitude are captured by all of these methodologies. We have the notch before the first double peak, and the wiggles between about  $t = 7$  and  $t = 9$ . One notable difference, however, is that the dip around  $t = 5$  is not captured very well by these methods. This means that either it is the result of interference effects which are not captured by the local harmonic prefactor or it relates to capturing the correct magnitude of the prefactor. From time  $t = 10$  (approximately one period) on, the same basic motifs repeat.

It is also interesting to compare the local harmonic prefactor with the unit prefactor. Although their results are very similar, there is a slight offset between them. This is basically because the local harmonic prefactor captures the zero point energy, while the unit prefactor does not.

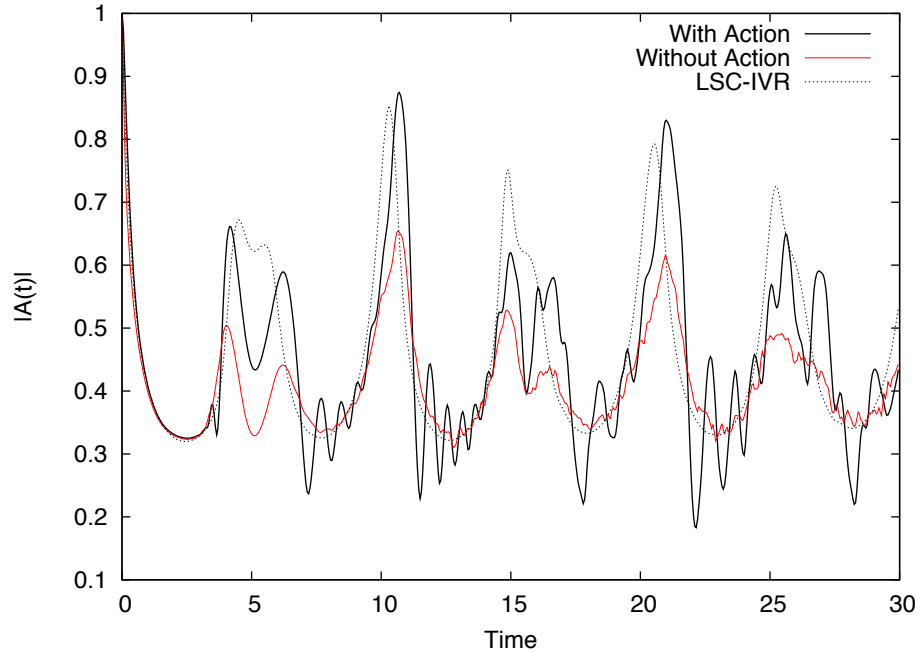
In figure A.3(b), we explore what happens to the survival amplitude of this system if we just turn off the action — *i.e.*, we set the phase factor  $e^{iS_t} = 1$  for all trajectories and all times. The black line is the full HK-IVR calculation (with action), the red line is if we turn off the action, and the dotted line shows the LSC-IVR result (which also doesn’t include the action). The first thing we note is that the magnitude of the recurrence peaks is much lower without the action.

---

\* It also sometimes called “Johnson’s multichannel WKB prefactor” or simply the “WKB prefactor.”



(a) Prefactor: The effect of different treatments of the prefactor.



(b) Action: The effect of turning off the action.

Figure A.3: Effect of various terms of the HK-IVR expression on the survival amplitude of the anharmonic Morse oscillator.

Up to the notch before the first double peak, the results are the same with or without the action. That notch is missing without the action, as are the wiggles which occur after between about  $t = 7$  and  $t = 9$ . Both of these aspects are also missing from the LSC-IVR. Although the no-action calculation misses the heights of the first double peak, which the LSC-IVR does capture, the no-action method does capture the deep dip around  $t = 5$ .

The point of all this analysis is to identify what features in the survival amplitude are related to which quantities in the semiclassical expression. To do that, I'll summarize the source of several features up to about time  $t = 10$ , after which the motifs repeat.

The double peak around  $t = 5$  corresponds to a half-period: trajectories which started in the well have gone to the classical turning point and returned to overlap with the original wavepacket, only with momentum in the opposite direction. Before the double peak, there is a small notch, which is the result of the action.

However, the most interesting feature around the double peak is the substantial dip in the modulus of the survival amplitude which occurs between the peaks. This effect is captured when we turn off the action, but not by the LSC-IVR or by either of the unit-magnitude approximations to the semiclassical prefactor. This means that it is either related to the magnitude of the prefactor in a way that the LSC-IVR fails to capture, or that it is related to the phase of the prefactor in a way that the local harmonic prefactor fails to capture. Considering the results of chapter 3, and figure 3.5(a) in particular, my suspicion is that it is a result of the phase of the prefactor. At time  $t = 5$ , when the dip happens, we see that the phase histogram is split into two regions separated in phase by a little more than one radian. In figure 3.7 we have the phase histogram from a time in the dip. It shows two peaks of roughly equal height, which suggests that the magnitude in one branch versus the other doesn't cause this feature.

The major peak around  $t = 10$  corresponds to the first full period of a typical trajectory from this initial distribution. Between the double peak and this single peak are a series of wiggles, which arise from the action. In both chapter 2 and chapter 3, we saw situations in which these wiggles were not captured. If we fail to sample sufficiently, as we saw in figure 2.9, then we don't sample the regions which contribute the different action which interfere to create the fringes we see in this region (which are analogous to the effect at  $t = 12.3$ ). In figure 3.9 we saw that the phase histogram in this region was extremely hard to fit, presumably because the two important features are very different: one is tall and narrow, and the other is short and broad.

A solid understanding of this simple (but subtle) system makes the anharmonic Morse oscillator into an excellent diagnostic tool. Although it is a simple one-dimensional system, it is unforgiving enough that it will expose many inadequacies in proposed methods. Furthermore, with the interpretation provided in this appendix, if flaws arise one can quickly understand what part of the semiclassical calculation isn't being captured by the new method.

## Appendix B

# Adaptive Gear 6th-Order Predictor-Corrector

Many of the calculations in this work are done with the fourth order integrator described by Candy and Rozmus,<sup>57</sup> with the treatment of the action and the monodromy matrices as described by the appendix of reference 65. However, when electronic degrees of freedom are included (as described in section 1.3), the underlying assumption of the symplectic integrator does not hold. That is, the Hamiltonian can no longer be written as  $H(p, q) = T(p) + V(q)$ , which allows the short-time factorization required by those symplectic integration schemes.

So we instead turn to an integration scheme that treats all variables, position and momentum, on equal footing. The 6th-order Gear predictor-corrector algorithm is one such method. Yet, even this can run into problems.

The work described in chapter 5 (on a semiclassical mapping for fermions) involves constraining the action variables to a range  $(r_1, r_2)$ . This is accomplished by including a terms in the Hamiltonian proportional to  $\sqrt{(n - r_1)(n - r_2)}$ . Unfortunately, the finite step size (and, in particular, the prediction step) can allow a trajectory near that boundary to step outside of it (causing numerical difficulties).

One solution would be to go to a much smaller step size (perhaps 2 orders of magnitude smaller) and rejecting the (relatively few) trajectories that fall out of these bounds. But since most of the time the dynamics were accurately described by the larger timestep, the idea of using 100 times as much computational effort to handle a problem that occurs on less than 1% of timesteps was unsatisfactory. So instead, we adopted an adaptive timestep algorithm.

Since the Hamiltonian was not amenable to the symplectic Candy-Rozmus integrator, I instead chose to use the 6th-order Gear predictor-corrector as my underlying integrator. I added an adaptive timestep algorithm (based on the Runge-Kutta adaptive timestep algorithm presented in Numerical Recipes) on top of the Gear integrator. Finally, a few modifications were made to the adaptive timestep procedure in order to make it useful for calculating time correlation functions, where many trajectories need to be averaged. The following sections will describe each of these steps.

## B.1 The 6th-Order Gear Predictor-Corrector

Like all predictor-corrector algorithms, the Gear algorithm has two steps to go from time  $t$  to time  $t + \Delta t$ . First, information at time  $t$  is used to estimate where the system should be at time  $t + \Delta t$ . Then information from this estimate is used to correct the state of the system (essentially, to minimize the error made in the estimate).

The Gear predictor-correctors are based on the idea of storing estimates of different orders of derivatives at a given time. Adams-Bashforth-Moulton predictor-corrector algorithms, on the other hand, only store the state and the first derivatives, but do so for several times.

The Gear predictor is very simple: since we assume that we have stored several orders of the derivative at time  $t$ , we use those derivatives to make an estimate for  $t + \Delta t$  based on the Taylor expansion.

The Gear correction requires that we calculate the first derivative in the estimated state, and compare that to the estimated first derivative. This difference is then used to correct the other derivatives (and the state of the system).

Further details can be found in Appendix E of reference 25.

## B.2 The Adaptive Timestep Algorithm

The basic idea of the adaptive timestep algorithm is to compare the predicted evolution for a half-sized step to that of a full-sized step. If it is within some tolerance then the step is accepted.

This does introduce significant overhead to the calculation, since each timestep actually requires the calculation of three timesteps. However, this allows us to usually take much larger timesteps, and only use small timesteps where absolutely necessary.

In order to define the tolerance, we calculate a linear approximation to the dynamics (in absolute magnitude) in order to provide a scale for the allowable error. That is, what we call the linear approximation  $\Omega^{\text{lin}}$  is given by

$$\Omega_{t+\Delta t}^{\text{lin}} = |\Omega_t| + |\dot{\Omega}_t| \Delta t \quad (\text{B.1})$$

To determine whether the trial step size is acceptable, we compare the system  $\Omega^{\text{full}}$  that results from taking a single full step from time  $t$  to time  $t + \Delta t$  with the system  $\Omega^{\text{half}}$ , which result from taking two half-sized steps to get from time  $t$  to time  $t + \Delta t$ . The step is accepted if, for all elements  $i$ , we have:

$$\frac{\Omega_i^{\text{full}} - \Omega_i^{\text{half}}}{\Omega_i^{\text{lin}}} \leq \epsilon \quad (\text{B.2})$$

for some tolerance  $\epsilon$ .

If the step is accepted, the next trial step is larger (unless, of course, the current trial step was already the maximum size). If the step is not accepted according to the criterion above, then the process is retried with a smaller step size.

Typically, when running the Gear integrator, the steps around  $t = 0$  will have to shrink very small. This is because the initial conditions for the derivatives are poorly chosen. The

initial conditions and the first derivatives are calculated correctly, but higher-order derivatives are initialized to zero, which is obviously incorrect. The small timesteps that result from the adaptive timestep algorithm have the effect of filling these in with more accurate derivatives, which are needed for accurate propagation of the trajectory.

### B.3 Fixing the Time Discretization

The work in the previous sections is well-described in the referenced literature. However, I had one more challenge to solve: the method described above allows the end time of each step to be at any point. However, I need to report the state of the system at specific times, so that I can average at the same time across many trajectories.

The most elegant way to do this is to save several points along the trajectory and use polynomial interpolation to estimate the value at the desired point. However, I decided to use a simpler method.

On the basis of the idea that adaptive timestep would be rarely used (the full-sized timestep is normally accurate), I thought of the step between each of my desired time-discretization points as a mini-trajectory with the adaptive timestep. The maximum allowed timestep was the difference between the current time and the next discretization timestep.

This works, although once the full timestep is the appropriate size, the calculation will switch between two timesteps: the last timestep in the previous discretization, and the remainder of that and the time discretization width. To solve this problem, I track how many adaptive steps are taken per discretized step. If that number is 2, then the estimate of the timestep for the next discretization step is the discretization width.

# Bibliography

- [1] E. Schrödinger, Ann. Phys. (Leipzig) **384**, 361 (1926).
- [2] G. Wentzel, Z. Physik **38**, 518 (1926).
- [3] L. Brillouin, C.R. Hebd. Scéances Acad. Sci. **183**, 24 (1926).
- [4] H. A. Kramers, Z. Physik **39**, 828 (1926).
- [5] J. H. Van Vleck, Proc. Natl. Acad. Sci. U.S.A. **14**, 178 (1928).
- [6] R. P. Feynman and P. A. M. Dirac, *Feynman's Thesis: A New Approach to Quantum Theory*, World Scientific, Singapore, 2005.
- [7] R. P. Feynman and A. R. Hibbs, *Quantum Mechanics and Path Integrals*, Dover Publications, Mineola, N.Y., emended edition, 2010.
- [8] W. H. Miller, Adv. Chem. Phys. **25**, 69 (1974).
- [9] M. C. Gutzwiller, J. Math. Phys. **8**, 1979 (1967).
- [10] W. H. Miller, Mol. Phys. **100**, 397 (2002).
- [11] V. S. Filinov, Nucl. Phys. B **271**, 717 (1986).
- [12] N. Makri and W. H. Miller, Chem. Phys. Lett. **139**, 10 (1987).
- [13] M. F. Herman and E. Kluk, Chem. Phys. **91**, 27 (1984).
- [14] H. Goldstein, C. P. Poole, and J. Safko, *Classical Mechanics*, Addison Wesley, San Francisco, 3rd edition.
- [15] D. W. H. Swenson, Tracking the Maslov Index, <http://www.hyperblazer.net/teaching/maslov-implementation.pdf>, 2008.
- [16] W. H. Miller, S. D. Schwartz, and J. W. Tromp, J. Chem. Phys. **79**, 4889 (1983).
- [17] X. Sun and W. H. Miller, J. Chem. Phys. **106**, 916 (1997).
- [18] H. Wang, X. Sun, and W. H. Miller, J. Chem. Phys. **108**, 9726 (1998).

- [19] X. Sun, H. Wang, and W. H. Miller, *J. Chem. Phys.* **109**, 4190 (1998).
- [20] X. Sun, H. Wang, and W. H. Miller, *J. Chem. Phys.* **109**, 7064 (1998).
- [21] J. Liu and W. H. Miller, *J. Chem. Phys.* **126**, 234110 (2007).
- [22] J. Liu and W. H. Miller, *J. Chem. Phys.* **125**, 224104 (2006).
- [23] Q. Shi and E. Geva, *J. Phys. Chem. A* **107**, 9059 (2003).
- [24] J. Liu and W. H. Miller, *J. Chem. Phys.* **131**, 074113 (2009).
- [25] M. P. Allen and D. J. Tildesley, *Computer Simulation of Liquids*, Clarendon Press, Oxford, 1987.
- [26] R. Gelabert, X. Giménez, M. Thoss, H. Wang, and W. H. Miller, *J. Chem. Phys.* **114**, 2572 (2001).
- [27] N. Ananth, C. Venkataraman, and W. H. Miller, *J. Chem. Phys.* **127**, 084114 (2007).
- [28] H. Wang et al., *J. Chem. Phys.* **114**, 2562 (2001).
- [29] M. Thoss, H. Wang, and W. H. Miller, *J. Chem. Phys.* **114**, 9220 (2001).
- [30] J. Liu and W. H. Miller, *J. Chem. Phys.* **127**, 114506 (2007).
- [31] J. Liu, W. H. Miller, F. Paesani, W. Zhang, and D. A. Case, *J. Chem. Phys.* **131**, 164509 (2009).
- [32] H. Wang, X. Song, D. Chandler, and W. H. Miller, *J. Chem. Phys.* **110**, 4828 (1999).
- [33] G. Tao and W. H. Miller, *J. Phys. Chem. Lett.* **1**, 891 (2010).
- [34] X. Sun and W. H. Miller, *J. Chem. Phys.* **110**, 6635 (1999).
- [35] W. H. Miller, *J. Phys. Chem. A* **105**, 2942 (2001).
- [36] H. Wang, M. Thoss, and W. H. Miller, *J. Chem. Phys.* **112**, 47 (2000).
- [37] W. H. Miller, *J. Chem. Phys.* **125**, 132305 (2006).
- [38] H.-D. Meyer and W. H. Miller, *J. Chem. Phys.* **70**, 3214 (1979).
- [39] R. Langer, *Phys. Rev.* **51**, 669 (1937).
- [40] G. Stock and M. Thoss, *Phys. Rev. Lett.* **78**, 578 (1997).
- [41] X. Sun and W. H. Miller, *J. Chem. Phys.* **106**, 6346 (1997).
- [42] S. Bonella and D. F. Coker, *J. Chem. Phys.* **122**, 194102 (2005).
- [43] S. Bonella, D. Montemayor, and D. F. Coker, *Proc. Natl. Acad. Sci. U.S.A.* **102**, 6715 (2005).

- [44] E. R. Dunkel, S. Bonella, and D. F. Coker, *J. Chem. Phys.* **129**, 114106 (2008).
- [45] S. X. Sun and W. H. Miller, *J. Chem. Phys.* **117**, 5522 (2002).
- [46] D. Frenkel and B. Smit, *Understanding Molecular Simulation: From Algorithms to Applications*, Academic Press, San Diego, 2nd edition, 2002.
- [47] C. Harabati, J. M. Rost, and F. Grossmann, *J. Chem. Phys.* **120**, 26 (2004).
- [48] J. C. Tully, *J. Chem. Phys.* **93**, 1061 (1990).
- [49] K. Levenberg, *Q. Appl. Math.* **2**, 164 (1944).
- [50] D. W. Marquardt, *SIAM J. Appl. Math.* **11**, 431 (1962).
- [51] W. H. Press, S. A. Teutolsky, W. T. Vetterling, and B. P. Flannery, *Numerical Recipes in C++*, Cambridge University Press, Cambridge, UK, 2nd edition, 2002.
- [52] E. Jones, T. Oliphant, P. Peterson, and others, SciPy: Open Source Scientific Tools for Python, <http://www.scipy.org/>, 2001–.
- [53] S. Garashchuk and J. C. Light, *J. Chem. Phys.* **113**, 9390 (2000).
- [54] M. Gruenwald and C. Dellago, *J. Chem. Phys.* **129**, 194101 (2008).
- [55] M. Henon and C. Heiles, *Astron. J.* **69**, 73 (1964).
- [56] K. T. R. Davies, T. E. Huston, and M. Baranger, *Chaos* **2**, 215 (1992).
- [57] J. Candy and W. Rozmus, *J. Comput. Phys.* **92**, 230 (1991).
- [58] K. G. Kay, *J. Chem. Phys.* **101**, 2250 (1994).
- [59] W. H. Miller and K. A. White, *J. Chem. Phys.* **84**, 5059 (1986).
- [60] H. D. Meyer and W. H. Miller, *J. Chem. Phys.* **71**, 2156 (1979).
- [61] H. D. Meyer and W. H. Miller, *J. Chem. Phys.* **72**, 2272 (1980).
- [62] G. Stock, *J. Chem. Phys.* **103**, 2888 (1995).
- [63] J. Klauder, *Ann. Phys. (N.Y.)* **254**, 419 (1997).
- [64] R. Gelabert, X. Gimenez, M. Thoss, H. Wang, and W. H. Miller, *J. Phys. Chem. A* **104**, 10321 (2000).
- [65] M. L. Brewer, J. S. Hulme, and D. E. Manolopoulos, *J. Chem. Phys.* **106**, 4832 (1997).